DECIPHERING INTRACELLULAR SIGNALING REGULATING DIRECTED CELL MIGRATION

by
Benjamin Chwanwen Lin

A dissertation submitted to Johns Hopkins University in conformity with the requirements for the degree of Doctor of Philosophy

Baltimore, Maryland
October, 2013

Abstract

Directed cell migration is a ubiquitous phenomenon with implications in development, wound healing, immunity, and metastasis. The ability of cells to orient their migration is dependent on the presence of external cues, the components to detect them and the intracellular networks to process them. This dissertation explores how the regulation of core intracellular components can shape directional migration responses and the mechanisms in which cells decode single and multiple external guidance cues. Given the complexity and redundancy in migratory signaling pathways, we develop a new technique to generate an intracellular gradient of protein activity without receptor activation. We demonstrate the utility of this technique by imposing gradients of different values of the active form of one of the core mediators of directed migration, a Rho GTPase, Rac. We find that shallow gradients of Rac alone are sufficient to direct the polarity and movement of cells, recapitulating phenotypes of chemoattractant induced migration and demonstrating synthetic chemotaxis in mammalian cells. These results reveal that cell polarity can be defined starting from a downstream node, Rac. Furthermore, we present a new refined mathematical model of cell chemotaxis and suggest a novel role for an upstream kinase, PI3K, in sensitizing cells to Rac activation. Next, we explore how cells process multiple guidance inputs, chemotaxis and contact inhibition of locomotion (CIL), and the resulting implications for directed cell migration. We find that chemotaxis and CIL do not act independently, as the resulting migration phenotypes when both cues are presented in conjunction are altered when they are presented individually. The balance between these cues is dynamic; modulating the strength of the cues through external inputs or molecular interventions can influence the

resulting directed migration outcomes. We further investigate the mechanistic basis of this dependency by enumerating the molecular mediators of these cues and finding where they might crosstalk. In this study, we develop several new techniques at the interface between engineering and the life sciences and present their applications. We anticipate that similar multidisciplinary approaches will help unravel mysteries in directed cell migration and in general biology.

Advisors: Andre Levchenko, PhD; Takanari Inoue, PhD

Readers: Andre Levchenko, PhD; Takanari Inoue, PhD

Thesis Committee: Peter Devreotes, PhD; Andrew J. Ewald, PhD; Andre Levchenko, PhD; Takanari Inoue, PhD.

Acknowledgements

I would first like to thank my advisors, Dr. Andre Levchenko and Dr. Takanari Inoue for their mentorship during my Ph.D studies. They helped me grow as a scientist through steady guidance during the most trying times of my studies and fostered the growth of interesting ideas through scientific discussion. Through their guidance, I began to see the bigger picture and was unafraid to tackle new and interesting scientific questions. I am also thankful for the scientific freedom I was given to grow and learn from my numerous mistakes. It was particularly gratifying to able to learn from the different scientific perspectives of both laboratories and to see their continued evolution.

I would also like to acknowledge the members of my thesis committee, Drs. Peter Devreotes and Andrew Ewald for their insightful comments on experiments and presentations, as well as career advice. I learned many lessons on how to communicate my research through both oral presentations and writing. I would like to further acknowledge my collaborators, Drs. Leah Edelstein-Keshet, William Holmes, Weibo Luo, Gregory Semenza, and Alfredo Quiñones-Hinojosa who were integral to my research and have enriched my experience at Hopkins.

I am very thankful for the special camaraderie I shared with the members of the Levchenko lab. We have shared many fun moments throughout my time at Hopkins which I will cherish. I would like to first acknowledge some of the lab alumni- Joanne, who introduced me to research, cultivated a passion for using microfluidics and was a mentor, Raymond, Saurabh, David Noren, Zhi-Zhong, Xiong, David Ellison, Hojung and Kshitiz who were always available for help. My research at Hopkins was particularly

aided by my neighbors, Adriel and Arnab. Our daily interactions, which mostly consisted of me asking them questions on analysis, coding, life, and/or experiments were invaluable to my research and to enjoying life in Baltimore. Alex, Patrick, Sung Hoon, Onur, Eric, Hao, Jin Seok, Chris, Ambhi, Kiran, Andrew, Tyler, and Matt, thanks for making the Levchenko lab such an enjoyable place to be.

I would also like to thank the members of the Inoue lab, who were not only my colleagues, but also my friends. I will always remember the fun lab events at Takanari's home and at the summer picnics. In particular, I would like to recognize Tasuku, Chris, Toru, Allison, Frank and Bob, who were of great assistance during my studies. It was amazing to see the growth of the laboratory from one postdoctoral fellow and one technician to where it is now. I look forward to seeing the continued development of the lab.

Finally, I would like to thank my friends who have made life in Baltimore enjoyable. The connections I have forged here will be carried far beyond Baltimore and throughout the rest of my life. I will end with acknowledging my family- my parents, Samuel and Shu, my brothers, Hubert and Wilson, and my sisters in law, Judy and Iris who have supported me throughout my time here. And of course, none of this would be possible without my wife, Ronnie, who was always there for me with love, extraordinary patience, sympathy, and humor and is truly my better half.

Table of Contents

List of Tables

List of Figures

Chapter 1. Introduction and Background

1.1 Directed migration in the developing and adult human

Directed cell migration is the ability of cells to sense, interpret and move towards or away from external stimuli. It is responsible for the proper function of a rich diversity of processes, including development[1], axon guidance[2], immunity[3], wound healing[4] and metastasis[5], among many others. Therapeutic interests in this field lie in juxtaposition; methods to augment or reduce directed motility are both being sought after. For example, the enhancement or correction of directed migration is ideal for wound healing applications[6] or an unresponsive immune system[7]. On the other hand, the abatement or blockage of directed migration is ideal for stopping the metastasis of cancer cells from primary tumor sites[8] or in treating inflammatory disorders[9]. Thus a fine balance exists between the sensitivity and selectivity of cell migration toward attracting or repulsing stimuli. A common approach to understanding directed cell migration has been to identify and characterize the roles of signaling proteins involved in migration. Over the past two decades, the individual functions and localizations of many components regulating cell migration have been identified[10, 11]. A core circuit of proteins has been outlined with each protein having a respective role. However, recent work has shown that the roles of some canonical proteins may not be clear cut and may be context dependent[12-14]. Additionally, alternative circuits have been discovered[15, 16] indicating redundancy in the process and adding new layers of complexity to understanding directed migration. A given migratory

cue binding to receptors on the cell surface can activate multiple pathways that converge onto similar downstream outputs. Thus the molecular basis of directed migration remains actively investigated. In the subsequent sections, we will provide a general background into the field of directed migration, with a particular emphasis on single cell studies and techniques, as these areas are the primary focus of this dissertation.

1.2 Environmental cues regulating directed cell migration

Given the abundance of processes which involve directed migration, it is not surprising that there are a plethora of cues which induce directional migration. Cues which induce directional migration are collectively referred to as "taxes", which is plural for the word "taxis", derived from the Greek word for arrangement[17]. The nomenclature of individual cues is acquired from the nature of the stimulus. For example, chemotaxis refers to directional migration in response to soluble chemicals while phototaxis refers to directional migration in response to light. Other directional migration cues include but are not limited to electric fields (electrotaxis)[18], adhesion (haptotaxis)[19], stiffness (durotaxis)[20], temperature (thermotaxis)[21], and topography (topotaxis)[22]. The most well studied taxis is chemotaxis, which is a focus of this thesis. However, as biological assays and observation techniques have advanced, other cues have begun to be recognized as prominent players in directed migration. It is important to note that these stimuli impart cellular guidance by being present in gradients, where concentrations or intensities vary across defined distances. Cellular guidance is achieved by detection of these gradations. Remarkably, single cells have the capacity to sense minute differences in cues across

their length and can subsequently migrate quite accurately[23]. This has lead to much fascination and speculation as to how this is achieved and has motivated the development of several model single cell systems.

1.3 Directed migration in single cells- model systems

In the subsections below, we will detail several popular single cell model systems used to study directed cell migration. These single cell model systems can be grouped into categories based on speed- fast moving (dictyostelium, neutrophils) vs. slow moving (fibroblasts, cancer cells) and morphology- amoeboid (dictyostelium, neutrophils, some cancer cells) vs. mesenchymal (fibroblasts, some cancer cells). Further subdivisions can be made by distinguishing the mode of motility, for example, generation of propulsion via f-actin rich protrusions or actin devoid blebbing driven by actin-myosin contractions. It is important to note that these distinctions may not always be clear cut, as some cancer cells and fibroblasts have been shown to change their morphology and mode of motility depending upon their local environment[24, 25]. The above dichotomy, particularly migration speed, has necessitated the development of different assays to study directed migration to match the time scales of motility and/or physiological environments. Details of these assays and their relative merits will be discussed in the later sections.

1.3.1 Dictyostelium discoideum

Dictyostelium discoideum (Dd) are soil residing social amoebas which migrate towards folic acid or other nutrients while vegetative. Upon starvation, complex morphogenesis takes place, where single amoeba aggregate through attraction to paracrine secretions of cyclic adenosine monophosphate (cAMP), forming converging cellular streams leading to the development of multi-cellular slugs and eventually, fruiting bodies[26]. These innate behaviors make Dd an ideal system for studying chemotaxis, as each phase of the dyctostelium life cycle relies on the ability to home towards soluble chemicals. Dd can be maintained in laboratory culture with controlled medium supplementation and defined developmental stages. Experimentally, Dd are genetically tractable with phenotypes which are relatively simple to evaluate and manipulate[27]. Many of the chemotaxis signaling pathways delineated in dictyostelium are preserved in higher order eukaryotes[27], thus making them suitable proxies for studying signal transduction. There are, however, notable differences between dictyostelium and mammalian cells, which must be kept in perspective when extrapolating results and conclusions.

1.3.2 Neutrophils

Neutrophils are members of the innate immune system which home to sites of bacterial infection and inflammation. Their primary function is to eliminate pathogens through phagocytosis and subsequent treatment with reactive oxygen species or antibacterial proteins[28]. Proper neutrophil behavior is essential for homeostasis[7], while improper behavior results in a host of autoimmune disorders[9], such as rheumatoid

arthritis. A large subset of their physiological behavior relies on their ability to migrate rapidly and accurately to specific tissues, thus necessitating robust cue detection and cytoskeletal arrangement systems. Neutrophils migrate directionally towards a variety of chemoattractants, ranging from bacterial peptides to inflammatory chemokines[28]. Primary neutrophils can be isolated through various methods for biological studies, including centrifugation from peripheral blood and peritoneal fluid[29]. Alternatively, given that neutrophils are short lived[30], an immortalized promyelocytic leukemia cell line, named HL-60, can be differentiated to become neutrophil like[31] with similar migratory properties and propensities[30].

1.3.3 Fibroblasts

Fibroblasts are mesenchymal cells critical to the wound healing process. After a post injury clot has formed from platelet aggregation, fibroblasts invade the wound clot, remodel the local matrix, and subsequently induce contractions which aid in reepithelialization[32]. Fibroblasts are normally quiescent, but are induced to proliferate and migrate directionally by mitogenic factors, with the most prominent factor being platelet derived growth factor (PDGF)[33]. Fibroblasts have also been shown to migrate towards extracellular matrix (ECM) components, such as collagen and fibronectin[33]. Many researchers have used primary mouse embryonic fibroblasts (MEFs) for experimentation[34], while others have used the immortalized NIH 3T3 cell line[35]. As mentioned above, fibroblast migration is quite slow when compared to neutrophils or Dd, differing by about an order of magnitude (10 μm/min for dictyostelium, 20 μm/min for

neutrophils, and .5~1 μm/min for fibroblasts[36]). Therefore, although many molecular players may be conserved among cell types, it is not surprising that fibroblasts have a distinct spatial detection mechanism and motility paradigm[36]. The above differences highlight the need to explore directed migration pathways in various cell types, as molecular interventions in one cell type may be ineffective in others.

1.3.4 Cancer cells

The textbook image of cancer is a mass of cells at a primary tumor site. This cell aggregation is induced by the acquisition of cellular mutations which enhance proliferation and survival beyond normal homeostatic levels. When cancer cells remain localized to the primary tumor site, prognosis remains relatively high, as extraction of the tumor via surgical or other therapeutic means is effective. However, when cancer cells metastasize, that is, disseminate from the primary tumor site to secondary sites in the body, mortality dramatically increases[37]. Directed migration is an essential step in metastasis[38], as it is involved in biasing cancer cell migration away from primary sites towards blood vessels, whereby subsequent intravasation into the blood stream promotes dissemination. Many cancer cells can migrate towards a variety of soluble factors, including chemokines and growth factors such as epidermal growth factor (EGF)[38]. The toolkit for studying directed migration in cancer cells revolves around the use of cancer cell lines for specific cancers. In this thesis, we will utilize a well characterized metastatic rat adenocarcinoma breast cancer cell line named MTLn3[39], which migrate towards gradients of soluble EGF[40]. As noted above for fibroblasts, MTLn3 cells and other

cancer cells contain distinct migration mechanisms, thus necessitating the elucidation of directed migration mechanisms in specific cell types of interest.

1.4 Collective migration

In single cell directed migration described above, cell to cell contacts and interactions are transient or non-existent. These ephemeral interactions allow cells to remain autonomous, as is seen in fibroblasts and neutrophils *in vivo* and permit characteristic single file cell streams as observed *in vivo* for some metastasizing cancers[38]. However, collective cell migration, where cell contacts are maintained, is also quite prominent in directed migration. For example, in metastasizing cancer, multicellular strands are frequently observed invading the local tumor stroma[41]. Collective migration also plays prominent roles in development, for example, in gastrulation, and in reepithelialization during wound healing[42]. There are several model systems used to study collective migration *in vivo*, these include border cell migration in Drosophila embryos[43], the zebrafish lateral line[44], and the neural crest in xenopus[45]. An important aspect of the above model systems is the ability to observe cells in the native *in vivo* environment. Other models of directed collective migration include culturing mouse mammary organoids[46] and primary carcinoma explants in 3D gels[47].

1.5 Intercellular cues regulating directed cell migration- Contact inhibition of locomotion (CIL)

The transition from single cell to collective cell directed migration highlights the importance of how cell to cell adhesion and coupling can transform single cell behavior to a concerted response. This suggests that in studying single cell directed migration, transient cell to cell interactions should not be disregarded, as they may modify and enhance locomotion. An important intercellular cue which influences directed cell migration is contact inhibition of locomotion (CIL). CIL was first observed roughly 50 years ago by Abercrombie and Heasyman[48], and can be defined as "the stopping of the continued locomotion of a cell in the direction that has produced a collision with another cell"[49]. Several cancer cells exhibit homotypic CIL, where collisions between two cancer cells will result in redirection of both cells[50]. Conversely, when many cancer cells contact nonmalignant cells during heterotypic collisions, migration remains unimpeded[51] and can be up-regulated[52]. This suggests that CIL may mediate the dispersal of malignant cells away from the primary tumor by preferentially orienting protrusions, while the lack of CIL with other cell types may enhance the dissemination of these cells into the stromal environment. In this thesis we will explore the relationship between CIL and chemotaxis during directed cell migration.

1.6 Processes in chemotaxis

In the section below, we will outline the canonical steps involved in chemotaxis, a form of directed cell migration, as it is a focus of this dissertation. Chemotaxis can be broken down into several separable steps which are essential for an accurate response. With the exception of adhesion, these steps are indispensable for directed migration. The first step involves sensing a cue which is accomplished via extracellular receptors. Next, cellular machinery is localized to occupied receptors which induces signaling and cytoskeletal polarity. Finally, cell propulsion is mediated by protrusions initiated by f-actin polymerization or blebbing driven by actomyosin contraction. In mesenchymal cells such as fibroblasts, adhesion is generated at the protrusion which generates a traction force necessary to pull the cell body forward. In the subsections below, we will describe several prominent molecules involved in directed cell migration.

1.6.1 Gradient sensing

Gradient sensing is achieved by receptors which uniformly decorate the cell membrane. In Dd and neutrophils, these receptors are G protein coupled receptors (GPCRs), while in fibroblasts and many cancer cells these receptors are receptor tyrosine kinases (RTKs). Regardless of receptor class, this uniform distribution of receptors allows cells to effectively sample their local environment and determine concentration differences across their diameter. Interestingly, various groups have demonstrated that in various cell types, receptor distributions remain uniform even in the presence of a

gradient of chemical ligands[53-55]. These experiments were carried out by introducing fluorescently tagged chemotactic receptors into the respective cell types and observing their distribution pre and post stimulation. An active cytoskeleton is not required for gradient sensing[56], indicating that these processes are separable. Overall, the above findings suggest that intracellular molecules mediate the subsequent polarized cell responses.

1.6.2 Polarization

Gradients of extracellular ligands induce differences in receptor occupancy across a given cell. These activated receptors, in turn, induce the local recruitment of several canonical polarity factors. One of the chief polarity factors is phosphoinositide 3-kinase (PI3K) which phosphorylates phosphatidylinositol (4,5)-bisphosphate (PIP2) to create phosphatidylinositol (3,4,5)-triphosphate (PIP3)[42]. Directionally migrating cells have PIP3 confined at the leading edge, where the directionality of migration is enforced. This localized recruitment of PIP3 has been observed in Dd[56], neutrophils[57], and fibroblasts[35] through the use of fluorescently tagged pleckstrin homology (PH) domains, which bind PIP3. The internal gradient of PIP3 is amplified with respect to the external ligand gradient in Dd[56] and neutrophils[57], but is not in fibroblasts[35]. Confinement of PIP3 at the leading edge is also mediated by the lipid phosphatase, phosphatase and tensin homolog (PTEN), which dephosphorylates PIP3 to PIP2. PTEN is localized to the lateral and rear membrane of migrating cells and is absent from the leading edge[58]. Although PI3K is a

crucial player in migration, cells can still undergo chemotaxis without it[12], suggesting that alternative pathways are also available for directing cells[15].

PIP3 localizes several pleckstrin homology (PH) domain containing proteins to the plasma membrane, notably, activators for small Rho GTPases known as guanine exchange factors (GEFs). The most well studied group of small Rho GTPases involved in cell migration are Rac, Cdc42, and RhoA[42], which predominantly reside at the plasma membrane. These small Rho GTPases cycle between an "on" GTP bound phase and an "off" GDP bound phase and contain intrinsic GTPase activity. GEFs catalyze the exchange of GDP to GTP, thus turning "on" small Rho GTPases. Conversely, GTPase-activating proteins (GAPS) accelerate intrinsic GTPase activity and turn "off" Rho GTPases. Another layer of regulation is instilled by the presence of GDP dissociation inhibitors (GDIs), which bind GDP bound Rho GTPases and sequester them from the plasma membrane.

Rac, Cdc42, and RhoA are central hubs in transducing upstream receptor level signaling to the cytoskeleton. The canonical studies from Alan Hall's lab using microinjected constitutively active forms of Rac, Cdc42, and RhoA in Swiss 3T3 cells demonstrated that disregulation of their protein activity could produce dramatic effects on the cytoskeleton[59-62]. In particular, constitutively active Rac produced broad protrusions called lamellipodia, with a characteristic dendritic network of F-actin filaments[61], while a constitutively active Cdc42 produced several spike like projections from the plasma membrane termed filopodia[62]. Contrary to Rac and Cdc42, constitutively active RhoA induced cellular contraction, characterized by the appearance of stress fibers[60].

Given these complex cytoskeletal phenotypes, the next logical question is where are the activities of these Rho GTPases localized in directionally migrating cells. This question was answered with the development of fluorescence resonance energy transfer (FRET)-based probes for Rac[63], RhoA[64], and a sensor for Cdc42[65]. These studies revealed that the activity of Rac and Cdc42 is localized to the leading edge[63, 65], while RhoA activity can be observed adjacent to the leading edge and at the rear of cells[64, 66]. In this thesis, we will explore how the spatial distribution of active Rac controls directed cell migration. We will also look at the activities of Rac and RhoA in migrating MTLn3 cells.

1.6.3 Protrusion

Cell propulsion is mediated by protrusions generated off of the cell body. In some cases these protrusions may be produced autonomously in the absence of stimuli[67], while in other cell types, they are produced in a stimulus dependent manner[68]. There are two main classes of protrusions, the first being f-actin mediated protrusions and other being actomyosin driven blebbing. F-actin mediated protrusions are driven by the force of polymerizing actin networks pushing against the plasma membrane. Blebbing is produced in an f-actin independent manner by hydrostatic pressure driven by local actomyosin contraction, leading to the rupture of cortical actin at the plasma membrane and outward movement of the membrane[69]. Recently a third class of protrusion termed lobodopodia was also shown to exist[25]. It is likely that these protrusive phenotypes are interchangeable and are variations of a general migration mode. Regardless, the diversity

of protrusions highlight the need to derive mechanistic insight into protrusive processes, as therapeutic molecule interventions may only be functional on a subset of cells. Activation of protrusive machinery is mediated through downstream effectors of the small Rho GTPases. Downstream of Rac and Cdc42 are the Wiskott-Aldrich syndrome protein (WASP) family proteins which can be categorized based on structure into WASPs and WAVEs[70] and other effectors such as the insulin receptor substrate protein (IRSp53) and p21 activated kinases (PAKs). Active Cdc42 can directly interact with IRSp53 to mediate the formation of filopodia[71], while active Rac can interact with WAVE complexes, which in turn, activate actin related proteins (Arp2/3), leading to increased actin branching and protrusion formation[70]. As opposed to Cdc42 and Rac, the function RhoA has traditionally been associated with contraction and retraction through its downstream effector, Rho-associated kinase (ROCK), which functions directly upstream of contractile machinery such as myosin II[72]. Blebbing is thought to be driven by the activity of RhoA. An alternative effector of RhoA is a formin, diaphanous-related formin-1, (mDia1), which can produce straight actin filaments leading to membrane protrusion[73]. These contrasting functions suggest that spatial activity of RhoA must be exquisitely regulated in migrating cells.

1.6.4 Adhesion

The formation of a protrusion is typically followed by the establishment of local adhesive sites. The maturation of these adhesive sites provides a traction force for translocation of the cell body. A cyclic process ensures proper cell migration: adhesions

are formed at cell protrusions while they are disassembled at the rear of cells[74]. Adhesion is mediated primarily by cell surface receptors called integrins, which can bind ECM components such as laminin, fibronectin, and collagen[75]. Bound integrins can recruit several signaling species, such as focal adhesion kinase (FAK) and src family kinases (SFKs) as well as cytoskeletal elements[75]. Although adhesion is critical to mesenchymal motility, it is dispensable for amoeboid migration or migration in 3D matrices, suggesting that adhesion is context dependent[76].

1.7 Assays to study chemotaxis

Progress in the field of chemotaxis has been spurned by the development of assays which have allowed a mechanistic understanding of how it occurs and to which factors. Each assay has its own set of advantages and drawbacks. For example, assays which allow live cell imaging can be coupled to fluorescent biosensors, which have been invaluable in the phenotypic evaluation of which sets of proteins appear at the "front" and "back" of migrating cells. On the other hand, end point assays allow a high throughput analysis of what factors may induce chemotaxis. In the sections below, we describe a few prominent assays used to study chemotaxis. Excellent protocols on how these assays may be executed and evaluated can be found here[77]. We will conclude with a brief description of how microfluidics has been used to study chemotaxis. A more detailed look will be given in the subsequent chapter.

1.7.1 Micropipette assay

The micropipette assay is a straightforward method to assess chemotaxis in a variety of cell types such as neutrophils[57], Dd[78], fibroblasts[35], and cancer cells[79]. In this assay, a fine tip micropipette is filled with a chemoattractant of interest and is lowered by micromanipulators to a set distance away from a group of cells. The chemoattractant is then ejected from the micropipette by pneumatic pressure, which allows the control of the ejection volume and frequency of ejection[80]. Exponential gradients are produced from the tip of the micropipette and decay sharply with distance. The advantages of the micropipette assay are that it is relatively easy to execute, fluorescent reporters can be used in cells of interest, and kinetics of responses can be measured. The disadvantages of this assay lie in the reproducibility of the size of the tip, which may alter the shape of the gradient, and in throughput, as only a few cells may be imaged in a given area around the micropipette. Disadvantages in throughput can be magnified when studying slower moving cells, such as fibroblasts and cancer cells, where responses may take on the order of tens of minutes and gradients may need to be maintained on the timescale of hours.

1.7.2 Boyden Chambers

The boyden chamber was developed by Stephen Boyden over 50 years ago as a simple population level assay used to assess chemotaxis[81]. The boyden chamber assay involves the use of a well with an upper and lower compartment separated by a porous membrane insert. Chemoattractants of interest are placed in the lower compartment and

will form a sharp gradient through the pores via diffusion. Cells seeded on the top of the insert will perceive the gradient and will migrate through the pores to the other side. At the end of the assay, cells are fixed and counted on the bottom of the insert using a microscope. The obvious advantage of using boyden chambers is in the high throughput data which can be collected, as this is an end point assay. The disadvantages of this assay lie in the inability to gain mechanistic insight into the chemotaxis process. For example, some factors may increase overall cell speed or increase cell proliferation but will not induce guidance. Such factors would be inaccurately assessed as chemotactic in this assay.

1.7.3 Zigmond, Dunn, and Insall Chambers

To increase the throughput and reproducibility of chemotaxis assays, a variety of chambers have been developed based on diffusive gradient development between a source chemoattractant and a sink. These chambers are named after their creators, Sally Zigmond[23], Graham Dunn[82], and Robert Insall[83]. In this set of assays, thin ridges are connected to a source and sink, thus generating a gradient across the ridges. The assay is initiated when a coverslip with adherent cells is inverted onto the viewing chamber, thus initiating a fluid connection between the source and sink. These viewing chambers allow the direct observation of chemotactic processes and allow the reproducible formation of gradients. The disadvantages of these assays lie in the stability of their gradient profiles, which evolve as the sink is saturated with chemoattractant over time, in the inability to

observe early events of chemotaxis, and in the planar geometry of the assay which fails to represent the typical 3D environment in which cells reside.

1.7.4 Hydrogel assays

Among the assays described above, hydrogel assays best represent the *in vivo* cellular environment. Hydrogels can be created based on native ECM molecules, such as collagen[47], or with agarose[84]. In these assays, groups of cells can either be placed in a preformed cavity in the hydrogel or the hydrogel itself can be polymerized around them. A chemoattractant is placed in a nearby preformed cavity and forms a gradient by diffusion from the cavity into the surrounding hydrogel, thus attracting cells to migrate towards it. As mentioned above, the advantage of such assays is the ability to recreate *in vivo* like environments. The disadvantages of this method lie in imaging cells through the hydrogel, which may cause optical distortion, and in the reproducibility of the gradient, as cavities are manually produced.

1.7.5 Microfluidic assays

Microfluidic assays allow the manipulation of fluids at the micro and nano-scale using custom tailored devices fabricated out of biocompatible polymers. The length scale of these manipulations matches the length scales of cells, thus making them well suited for controlling cellular microenvironments, and in particular, assaying chemotaxis. Mehmet Toner's group was the first to use microfluidics to create gradients of a

chemoattractant to study chemotaxis in 2002[85]. They studied neutrophil responses to linear and complex gradients of interleukin-8 generated by an upstream "Christmas" tree like network. Microfluidic assays have several distinct advantages which we will outline in the subsequent chapter. The chief drawbacks to using microfluidics are the specialized setups needed to run the assays and lack of commercial availability of most devices.

1.8. Aims and significance of this research

Progress in the field of directed migration is driven largely by the advancement of techniques which allow the observation of new phenomena or can ask an entirely new set of questions. A prime example of this was the development of fluorescent biosensors, which revolutionized our understanding of how cells could sense an external gradient and proved a means to systematically look at the spatial and temporal behavior of intracellular components involved in directed migration. The general aim of this thesis is to explore the molecular underpinnings of directed migration through the development of new technologies. We seek to answer the following questions- 1) Is the graded activity of a core component sufficient in itself to induce directed migration? 2) How are multiple cues integrated during directed migration? A specific set of aims are enumerated below.

<u>Specific Aim 1-</u> Develop microfluidic platforms for studying directed migration mechanisms and phenomena in cancer cells (Chapter 2).

We will begin with a review of microfluidics and will enumerate several of the principles of why it is an effective tool for studying cell biology. We will also provide several examples of how microfluidics has been used to control cell positioning and for the manipulation the spatial and temporal environment around cells. Finally, we will describe how we developed a new set of devices to study the mechanisms of directed cell migration in cancer cells, which will be utilized in chapters 3 and 4. Protocols for device fabrication are also found in this section.

Specific Aim 2- Directly recapitulate a native, active protein distribution of a known regulator of cell migration in living cells and assess its affects on directed migration. (Chapter 3)

We use our first set of tools developed in aim 1 to create a platform for directly inducing graded activation of Rac, an important regulator of cell migration. We further delve into how these perturbations provide new intuition into the function of pathways converging on Rac activation.

Specific Aim 3- Dissect how multiple cues are integrated during directed cell migration (Chapter 4)

In this aim, we use our second set of tools developed in aim 1 to understand the interplay between chemotaxis and CIL in controlling directed cell migration. We provide further insight into how this is mediated at the molecular level and the implications for the overall cell population.

The research presented here makes significant contributions to the scientific community from both technical and mechanistic standpoints. We develop new technological platforms which enable sensitive control over cellular microenvironments and enable us to address fundamental questions in directed cell migration. We utilize these tools to derive new insight into the signaling mechanisms regulating directional migration by specifically perturbing the spatial-temporal activity of intracellular components. Furthermore, we present tools to study how multiple cues interact during directing migration in cancer cells, addressing one of the current challenges in the directed cell migration community. We suggest that the maturation of these tools will help reveal how directed cell migration is achieved.

Chapter 2. Development of microfluidic platforms for studying directed migration

2.1 Microfluidic technologies for studying cell biology

2.1.1 Introduction

The term "microfluidics" denotes an extensive set of techniques and tools developed largely over the last decade for manipulation of fluids at the micro- and nano-liter scale using fabricated networks of precisely manufactured channels, chambers, and valves. There are several advantages to working at this small scale, including predictable fluid flows (only laminar flow is expected under most circumstances), small reagent consumption, and reduced spatial device footprints. At its inception, microfluidics was geared toward reducing the cost and increasing the throughput of traditional biochemical assays, such as capillary electrophoresis[86], PCR[87], chromatograpy[88], and FACS[89]. More recent advances have expanded the breadth of microfluidics to biological applications, including live cell assays with real time monitoring of biochemical processes using diverse imaging techniques, particularly fluorescent microscopy. Microfluidic devices are capable of assaying multiple inputs of various magnitudes by manipulating the soluble

and surface immobilized cell milieu with concomitant detection of dynamic output signals with high spatio-temporal resolution (**Fig. 2.1**).

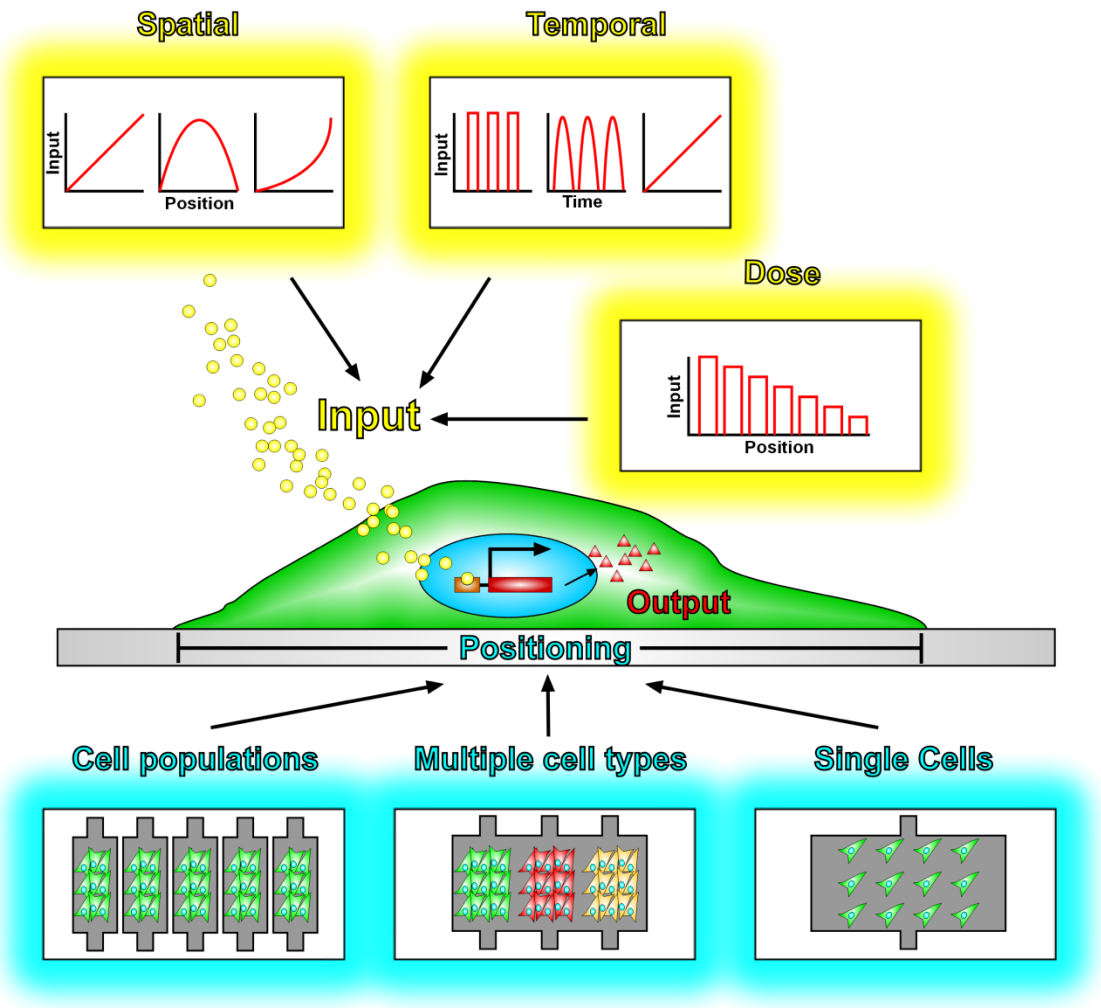

Fig 2.1: Microfluidic devices are platforms allowing precise spatial and temporal control over inputs as well as patterning of cells and their adhesion substrates.

These assays take advantage of a highly developed technological capacity to translate manipulation of liquid flows into control of the extracellular environment in a well defined spatial-temporal manner and the emergence of ever expanding molecular reporters used with highly developed microscopy systems. In what follows, we will

briefly introduce microfluidic devices and their beneficial properties for studying biological problems. We will also highlight techniques used in microfluidics devices falling into two general categories; positioning of cells and their adhesion substrata and controlling dynamically and spatially variable environments.

2.1.2 Biocompatibility of microfluidics

Presently, a vast majority of microfluidic devices are fabricated from polydimethylsiloxane (PDMS) using a process known as soft lithography. These devices are created via replica molding off silicon masters, where user-defined patterns deposited on the masters are embossed into the final device. The resulting networks of various pre-designed features, including channels and chambers, are sealed to a surface compatible with imaging and, if desired, cell adhesion, such as glass, and are coupled to a flow input/output control system. Excellent reviews on fabrications processes can be found in a number of recent references[90, 91]. Overall, the design and fabrication of PDMS devices can occur on the time scale of a few days, allowing rapid prototyping and general ease of use.

PDMS has several advantages for use in biological assays; it is optically transparent, permeable to atmospheric gases, chemically inert, mechanically flexible and electrically insulating[92]. The optical transparency allows the use of transmitted light and fluorescent signals for imaging cell activity. Permeability to non-polar gases, particularly oxygen and carbon dioxide, is beneficial for culturing cells within devices over extended

periods of time. Microfluidic cell culture arrays have been developed which allow continuous cell culture for weeks[93]. Furthermore, electrical insulation provided by PDMS permits additional use of electric fields to precisely control flow and cell properties.

In addition to the many physical and chemical benefits provided by PDMS as a fabrication material, there are several advantages gained from the physics of working at the microscopic length scale of microfluidic devices. Arguably the most important benefit is non-chaotic, laminar liquid flow due to a low Reynolds number, the number that characterizes fluid behavior in a given system. In this regime fluids mix purely by diffusion. For example, two parallel streams containing different molecular solutes will mix in a gradual manner defined by diffusion at their interface. Researchers have utilized this property to create concentration gradients through serial dilution of input solutions navigating through series of merging and splitting channels. This technique will be discussed in more detail below. Other benefits of working at this spatial scale include reduced sample volumes, opportunities for parallelization, and functional chambers at the length scale of cells. More details of the physics underlying microfluidics can be found here[94].

2.1.3 Control of positioning of cells and their adhesion substrata

Well established techniques exist for controlling cell positioning within microfluidic devices, including segregating cell populations into several discrete chambers, patterning multiple cell types, and isolating single cells (**Fig. 2.1**). Microfluidic devices achieve this through electrical, magnetic, mechanical and chemical cell

manipulation. We will describe mechanical and chemical techniques using soft lithography which have become standard for multiple labs.

2.1.4 Patterning of cell populations

Two of the earliest modalities for patterning populations are a) PDMS stencils to physically block select regions and b) using microfluidic channels to restrict the deposition of extracellular matrix (ECM) as the substratum for cell adhesion and to control cell deposition onto the substratum from cell suspensions. Folch et al. used PDMS stencils to restrict the attachment of primary rat hepatocytes to square zones across various substrates[95], while Stine et al. used a similar system to create a co-culture of melanoma and human umbilical vein endothelial cells (HUVEC)[96]. Utilizing an alternative technique, Folch and Toner used microchannels as templates to deposit ECM on different biocompatible substrates[97]. After washing and removal of the elastomeric device, co-culture of different cell types could be achieved by adding distinct cell types after the initial patterning. Another method to control ECM patterning is by interfacing multiple laminar flow streams in microfluidic devices (**Fig. 2.2a**). As mentioned above, merging streams in microfluidic devices normally mix purely by diffusion at their

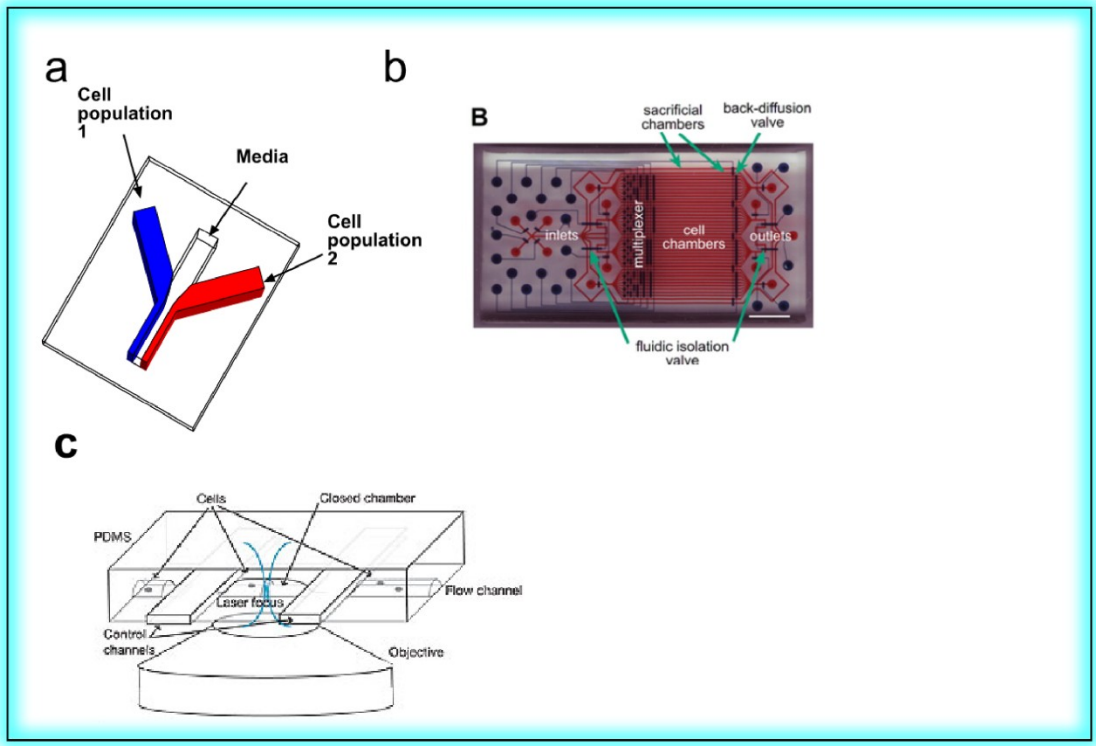

Fig 2.2: Microfluidic technologies for precise positioning of cell populations.

(a) Three laminar flow streams can be used in a microfluidic device to selectively deposit cells in a given position. (**b**) A microfluidic device can be used for high throughput screening of cytokine responses in cell populations seeded into separate chambers. Each chamber can encompass an individual treatment condition and enable screening of cell responses. (**c**) Sample chambers within a microfluidic device can be used to isolate single *E. coli* cells by pressurizing surrounding valves.

interface. If the flow rates are fast enough, this mixing becomes negligible over the time course the flows are interfaced in the device and precise boundaries between deposits used for patterning can be achieved. Takayama et al. used up to 5 merging microchannels to selectively deposit erythrocytes and E.coli in parallel lines[98]. Controlled perturbation of subpopulations is also possible in this configuration, as evidenced by selective trypsinization and labeling of bovine capillary endothelial cells[98]. On the other extreme of

device design complexity is the ability to use channels of simple geometric cross-sections (particularly triangular) for depositing smooth gradients of ECM[99].

Cell populations can also be distributed into separate chambers within microfluidic devices. When coupled to on chip valves these chambers are addressable individually or in groups, thus allowing screening of different inputs across large samples. Valves will be described in more detail below. Based on this principle, Cheong et al. developed a high-throughput microfluidic device to study cytokine or growth factor responses in cell populations across multiple concentrations and stimulation durations[100-103] (**Fig. 2.2b**). Other groups have developed similar designs[93, 104] which have been used to study inflammatory processes[105]. Taylor et al. significantly expanded the throughput of this technology by creating a highly parallel device with 2048 assayable chambers with the ability to use different cell types and stimulus patterns[106].

Another subset of devices are designed to serve as chemostats, where cell populations are monitored over extended time periods with continuously renewed culture conditions. Balaban et al. used PDMS channels separated from a fluid network by a membrane to analyze the growth of single and multiple bacteria cells over time[107]. Medium in the fluidic channels continuously renewed nutrients via diffusion through the membrane to the bacteria cells underneath. Groisman et al. used a multi height single layer PDMS device to isolate bacteria cells in chambers adjacent to medium supplying channels[108]. Connections between the chambers and supply channels were approximately 0.6 μm, thinner than an *E.coli* cell diameter, but increasing the overall in-device pressure could reversibly enlarge the connections (similar to the effect of an inflating balloon), thus allowing cell seeding to the chambers. Continuous perfusion of media supplied

nutrients via diffusion from the perfusion channels through the thin connections, also allowing concomitant removal of waste from the chambers. Cho et al. used a similar device with arrays of chambers with different sizes and shapes to explore the relationship between confinement geometry and cellular self-organization in a model of biofilm initiation[109].

2.1.5 Positioning of single cells

Separation of autocrine from paracrine signaling is often desirable to study autonomous signaling at the single cell level. To remove paracrine signaling, cells need to be isolated individually. Single cell isolation is difficult to achieve using traditional laboratory techniques but a variety of microfluidic tools have been developed to address this issue. One of the earliest methods to isolate single cells, known as micropatterning utilizes PDMS as a stamp by absorbing ligands from solution and depositing them in user defined patterns onto substrata based the shape and area of contact with the stamp. Chen and colleagues used micropatterning to create different sized 'islands' of fibronectin to decouple the effects of cell spreading vs. adhesive signaling in controlling programmed cell death[110]. Increases in the size of islands reduced cell death but the results were confounded by a concomitant increase in adhesive signaling. To separate the effects, smaller fibronectin microspots in the 3-5 μm range were created with unadhesive compounds between them. Cells extended across spots and a decrease in apoptosis was seen with increased cell spreading while having comparable integrin signaling levels, thus supporting a role for spreading in controlling apoptosis.

Geometric traps have also been successfully used to isolate single cells from suspension. These designs generally rely on hydrodynamic trapping, where flow is allowed to pass through arrays of crevices smaller than a cell diameter and are subsequently blocked once a cell arrives. The Lee group designed an array of U-shaped structures utilizing hydrodynamic trapping to isolate single cells[111]. An array of 100 cells was successfully captured with 85% retention after 24 hours of continuous perfusion. Using a similar design, the Voldman group fabricated arrays of capture cups to investigate cell paring and fusion[112]. Up to 70% pairing efficiencies were obtained between multiple cell types using a multi-step loading protocol. The device also allowed coupling to traditional chemical and electric fusion stimuli. Other trapping designs include ' jails'[113], hook-shaped traps[114], and 'docks' at T junctions[115].

Another technique to isolate single cells relies on the use of elastomeric valves fabricated by stacking multiple layers of PDMS. This technology was pioneered by the Quake group and demonstrated a simple and robust method to control fluid flow[116]. A typical setup includes two layers of PDMS, where one layer contains the fluidic network and a separate valve layer is bonded on top. Channels in the top, valve layer, can be pressurized and subsequently deflect the PDMS membrane separating the valve from the fluidic network which suppresses flow. Cai et al. used on chip valves to isolate single *E. coli* in microfluidic channels to study protein expression using enzymatic amplification of secreted protein products[117] (**Fig. 2.2c**). The valving technique allowed the seclusion of very small volumes of solution, about 100 pl, thus giving the authors the ability to detect single molecules.

Lastly, Yin et al. used dielectrophoretic (DEP) forces to induce heterotypic and homotypic single cell paired interactions in a microfluidic device[118]. Generation of polarized electric fields across cells in a device can lead to electrical polarization of the cells themselves. This polarization is sufficient to pull cells towards sources of maximum or minimum DEP depending upon intrinsic cell properties and the surrounding medium. The researchers were able to precisely pair together different cell types, a549 human lung cancer cells with human umbilical vein cells (HUVEC), or cells of the same cell types.

2.1.6 Input control

Beyond patterning of cell positions, microfluidic devices have the capability of controlling cell stimuli in space, magnitude and time (**Fig. 2.1**). Possible perturbations of the cell microenvironment include a) generation of spatial gradients of input signals through progressive serial dilution of two or more input streams into a series of streams spanning several orders of magnitude in concentration; b) diffusion based gradient formation, and c) creation of complex, temporally variable stimuli defined over a variety of time scales, including oscillatory inputs. These complex input distributions are made possible through the predictable mixing behavior of fluids in microfluidic channels. They have been utilized to study fundamental cellular behaviors, such as chemotaxis, axon guidance, inflammatory responses, differentiation, as well as activation of mutiple signaling pathways. Below we provide several illustrative examples of how microfluidic generation of diverse spatial and temporal stimuli can be used to address important questions in cell and tissue biology.

2.1.7 Temporal control of inputs

Valves in microfluidic devices, whether external or internal, have enabled the creation of dynamically changing input signals, as complex as e.g., pulsatile or ramp stimuli, which can be adjusted in frequency, amplitude, and shape[119]. As opposed to the step inputs, typically applied by addition of a stimulus to a dish, oscillatory stimuli can reduce noise, reveal the bandwidth of a pathway, and help understand adaptation mechanisms[120, 121]. Microfluidic devices designed to produce waveforms typically have multiple input streams gated by valves. Actuation of valves controls which stream enters the cell microenvironment, thus allowing the formation of square waves by rapidly switching between streams of different concentrations (**Fig. 2.3a**). More complex waveforms can be achieved by allowing the input streams to mix in different proportions by controlling their relative flow rates.

In one of the first studies to utilize microfluidic generated waveforms, Mettetal et al. used a valve driven flow system to generate square waves of different osmolyte concentrations to study the osmo-adaptation pathway in yeast[122]. A biosensor for high-osmolarity glycerol (HOG) was used to quantify signaling responses to the induced stresses. The effects of two previously known negative feedbacks in the HOG pathway, through fast and slow mechanisms, were decoupled by comparing the frequency responses of wild type yeast with a mutant harboring decreased HOG1 activity. Similarly, Hersen et al. used microfluidic driven pulsatile stimuli, created by varying the flow rates

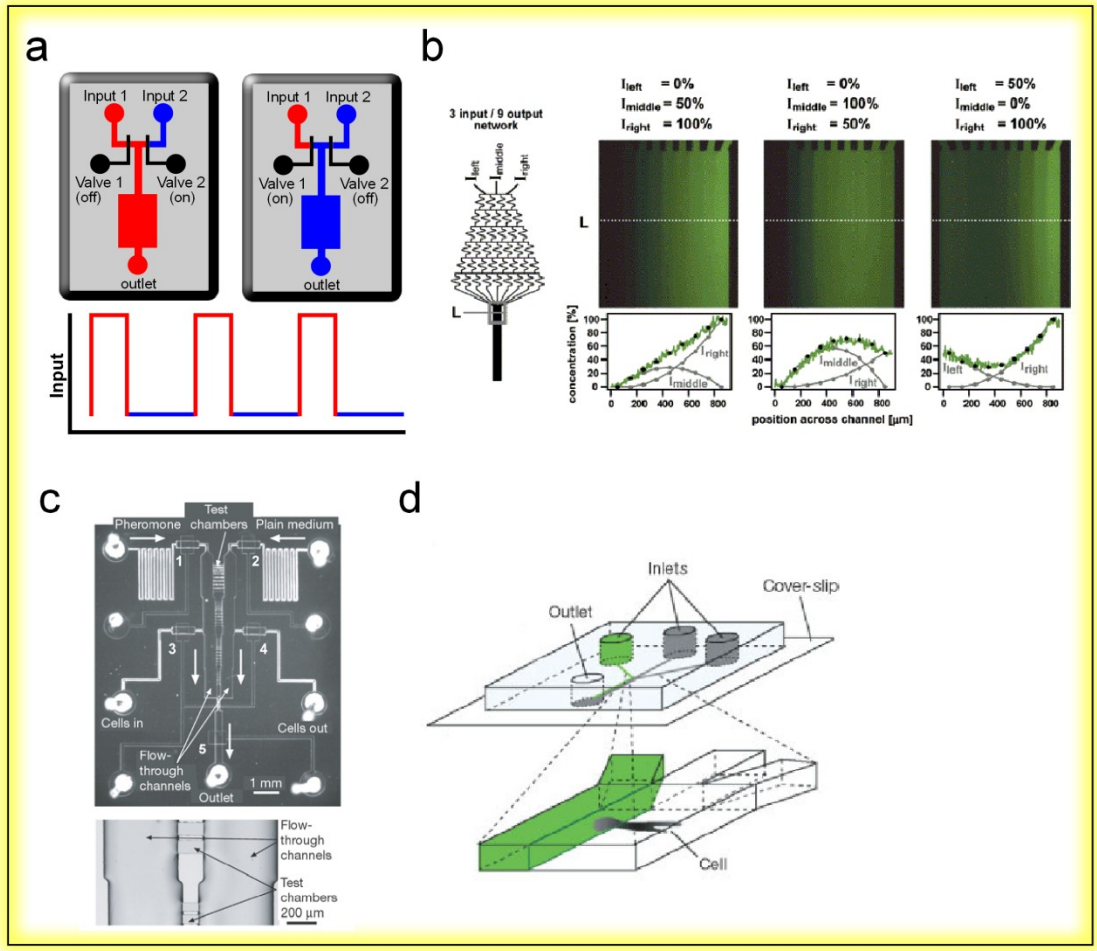

Fig 2.3: Microfluidic technologies for controlling cellular environments.

(**a**) Schematic of a simple microfluidic device used to generate square waves of input by switching between two input solutions containing different concentrations of inputs. (**b**) A microfluidic gradient generating network with three inputs. When solutions containing different concentrations of fluorescein are connected to the different inlets, various gradient profiles can be obtained. (**c**) A microfluidic device used to generate gradients across test chambers of various sizes by diffusion. Two flow-through channels are connected by the test chambers. Stimulants are introduced into one flow-through channel and form a linear gradient across the test channels by diffusing towards the other flow-through channel. (**d**) A three inlet microfluidic device, similar to that shown in **Fig. 2.2a** is used to selectively stimulate a portion of a cell seeded into the chamber.

of the inputs and thus their interface across a channel, to investigate the bandwidth of the HOG pathway[123]. Microfluidic waveform devices have also been used to study metabolic regulation[124] as well as chemotactic signaling[119].

2.1.8 Spatial control of inputs

The methodology of generating soluble and surface bound gradients of biologically active molecules was first demonstrated by the Whitesides group[125, 126] (**Fig. 2.3b**). Analogies between electric and fluidic circuits were used to predict the serial dilution of input streams via multiple junctions, splitters, and fluidic resistors. The resulting output streams, spanning the concentration range defined by the input concentrations, can be merged in an outlet channel to generate the final concentration gradient. One of the first studies utilizing microfluidic gradient generation was carried out by Jeon et al. to study the chemotaxis of neutrophils in gradients of a chemokine, interleukin-8[127]. Gradients in this analysis could be generated within seconds and maintained stably pending available reagents. This device allowed concurrent time-lapse imaging of initial neutrophil responses as well as quantitative characterization of motility vs. several applied gradients. Complex gradient shapes could be created in addition to linear gradients, including parabolic and "sawtooth" shaped gradients profiles. Others have applied similar designs to create exponential gradients[128], fast switching gradients[129], multiple opposing gradients[130], and other complex shapes[131].

Gradient generating networks can be slightly adjusted to create several discrete dosages rather than a smooth gradient. Instead of merging separate streams of different concentrations, the streams can be fed into separate channels, thus exposing each channel to a well predicted, discrete concentration spanning the range of the inputs. Thompson et al. utilized such a device with an upstream dilution module and downstream cell chambers to look at the dynamics of NF-κB activity in cells across multiple densities and concentrations of TNF-α[132]. The advantage of such parallel exposure designs is the rich variety of data obtained in a single experiment with the simple preparation of two input solutions. We will utilize a similar design to study the EGF dose dependence of CIL in MTLn3 cells in chapter 4.

The techniques discussed above can be lumped together as flow-based techniques, in which continuous flow is needed to maintain the gradient. For non-adhesive or less robust cell types, milder gradient generating techniques have been developed which rely on passive solute diffusion between a source and sink. A source and sink can be linked together by one or more channels and a linear gradient can be generated between these channels via diffusion. If the source and sink are continuously renewed due to liquid perfusion, the established gradient can persist indefinitely. Modulation of the steepness of gradients can be achieved by varying channel lengths, while variation of widths can modulate cell numbers. Paliwal et al. developed and used a microfluidic device based on this principle to study the mating response of yeast in gradients of pheromone[133] (**Fig. 2.3c**). A variety of mating phenotypes could be observed at different concentrations of pheromone, with cells also displaying different chemo-sensing accuracies. Similar devices have been used to explore cell differentiation[134] and chemotaxis[135, 136]. The

devices utilized in chapter 3 and 4 are based on the principles of passive gradient generation.

Sub-cellular patterning of stimuli is also achievable through microfluidics. The well-defined interface between multiple streams in a microfluidic device can be positioned over single cells to induce spatially heterogeneous stimulation. Takayama et al. used a microfluidic device to label select populations of mitochondria within a single cell and also induced local disruption of actin filaments[137] (**Fig. 2.3d**). Similarly, Sawano et al. locally exposed Cos-7 cells to epidermal growth factor (EGF) to determine the extent of lateral propagation of downstream signaling[138]. Interestingly, the lateral propagation increased with overexpression of EGF receptors, thus elucidating a new mechanism enabled by microfluidic technology.

2.2 Development of a microfluidic platform for inducing subcellular gradients

In this subsection, we will outline the development and rationale behind the microfluidic device used in chapter 3. We will enumerate a set of device requirements we satisfied in order to achieve a functioning device. We will follow this with a discussion on how our design met those requirements. Finally, we will provide a protocol of how we produced our devices.

2.2.1 Device requirements

The primary requirements of our device were as follows- 1) generate gradients of a soluble chemical in a reproducible fashion, 2) generate these gradients across single cancer cells, and 3) do this in a high throughput manner. We also had two other secondary criteria. The first was to minimize shear stress across cells. Shear stress has been shown to induce directed migration responses, alter cell signaling, and reduce cell viability[139], and thus could obfuscate responses to soluble chemicals. The second was to have all cells receive the stimulus at a time scale which would be negligible compared to the time scale of cell responses. For example, if cell responses occurred on the order of tens of minutes, then a time window of a few minutes would be reasonable for all cells to receive the stimulus. This would, in turn, allow us to accurately assess the cell response kinetics across the population.

2.2.2 Device design

Our design (**Fig 3.1, Fig. 3.2**) was inspired by studies carried out by our lab to study gradient sensing in yeast[133] and by the Toner group for studying neutrophil chemotaxis[140]. Gradient generation is achieved by diffusion between a source and sink, similar to the principles of the various chambers described in the introduction[23, 82, 83]. However, in our device, the source and sink are continually replenished by flow originating from an upstream network, thus maintaining a very reproducible gradient at steady state indefinitely, as long as the volumes of the respective sources are maintained. This fulfilled one of our primary requirements of having a well controlled gradient. We connected our source and sink by 250 individual microchannels with widths (18 μm)

matching the diameters of single HeLa cells. This gave us 250 potential opportunities to assay single cells, thus allowing us to have high throughput yield of single cell data and fulfilling our two other primary requirements. To reduce the potential shear stresses in our system, we introduced two modifications. First, we optimized the ratio of the height of the microchannels to those of adjacent source and sink to minimize cross flow between them. The resistance in a given rectangular channel with a high aspect ratio can be approximated with the following equation-

$$R = \frac{12\mu L}{wh^3}$$

where R = resistance, μ = the viscosity of the fluid, L = the channel length, w = the channel width, and h = the channel height[94]. As the height term dominates the resistance equation, we found an optimal ratio to be ~1:16 with the height of the microchannels being 6 μm and the source and sink having a height of 100 μm, thus providing a ~25 fold increase in resistance and drop in flow rate in the microchannels. Second, we used the flow balancing scheme from the Toner group[140], where the source and sink input streams meet and split off before entering the main interrogation chamber. This provides an opportunity for any flow imbalances in the input streams to balance out. Thus with these two modifications we fulfilled the first of our two secondary criteria in minimizing shear stress across cells. Finally, we found that the response kinetics in our experiments (Chapter 3) were on the order of tens of minutes. We optimized the flow rate in our devices to have all cells experience the gradient in less than 5 minutes, therefore fulfilling the last of our secondary criteria.

2.2.3 Device fabrication protocol

We provide a general protocol here for fabricating microfluidic devices used in chapter 3. This protocol necessitates the use of a clean room, as dust or other air pollutants can cause significant defects. We create our device designs in Freehand (Macromedia); however, any computer assisted design (CAD) software can be used to create devices. These designs can then be printed on a high resolution mylar transparency from a printing company. For low resolution designs (smallest feature > 20 μm), we recommend In Tandem design (Towson, MD), while for high resolution designs, we recommend CAD art services (Bandon, Oregon). Care must be taken to ensure the resolution is high enough to match the smallest feature size.

Microchannel layer

1) Clean a 3 inch Silicon wafer using spray bottles positioned over an appropriate waste container in the following order- 1) Acetone, 2) Isopropanol, and 3) DI water.

2) Dry wafers using nitrogen air stream and place on hotplate >100 $^{\circ}$C for at least 5 minutes to ensure all water has evaporated.

3) Spincoat SU-8 3005 (Microchem) at 3000 rpm for 30 seconds.

4) Soft bake the wafer on a hotplate at 95°C for at least 10 minutes.

5) Expose the wafer using a mask aligner using a constant energy of 1000 mJ/cm^2.

(We utilize a long pass UV quartz filter (Omega Filters) which provides straighter channels but require more exposure energy.)

6) Post exposure bake for 1 hour at 95°C.

7) Develop in SU-8 developer (Microchem).

8) Hard bake for at least 1 hour at 200°C.

Fluidic layer

1) Use the microchannel layer wafer created above and repeat steps 1 and 2 above.

2) Spincoat SPR-220-7 (Megposit) at 730 rpm for 30 second on the silicon wafer.

(note- silane coating may improve the adhesion of SPR-220-7)

3) Soft bake for 8 minutes at 115°C.

4) Allow the SPR-220-7 coated wafer to rehydrate at room temperature for at least 1 hour. Care must be taken to align the fluidic layer to alignment marks put into the microchannel layer.

5) Expose the wafer using a mask aligner using a constant energy of 600 mJ/cm^2.

6) Develop using a 1:4 dilution of AZ400K developer (Clariant).

7) Round channels by baking at 125°C for 15 minutes.

Control valve layer

1) Use a new silicon wafer and follow steps 1 and 2 as outlined for the microchannel layer.

2) Spincoat SU-8 2025 at 1500 rpm for 1 minute.

3) Soft bake the wafer at 95°C for 2 hours.

4) Expose the wafer using a mask aligner using a constant energy of 2000 mJ/cm^2.

5) Post exposure bake for 1 hour at 95°C.

7) Develop in SU-8 developer (Microchem).

8) Hard bake for at least 1 hour at 200°C.

PDMS device fabrication

1) Prepare a 8:1 and 20:1 mixture of component A to component B of RTV615 (Momentive) and mix in weight boats for at least 5 minutes.

2) Remove air bubbles with a vacuum chamber.

3) Treat the microchannel + fluidic layer wafer and the control layer wafer with chlorotrimethylsilane (TMCS) by placing wafers into a vacuum dessicator and placing a few drops of TMCS into a bottle cap. Evacuate the chamber and let sit for at least 20 minutes.

4) Spincoat the 20:1 mixture onto the microchannel + fluidic layer wafer at 1600 rpm for 60 seconds.

5) Place the control layer wafer into a heat resistant container and pour the 8:1 mixture on top.

6) Place the spincoated microchannel + fluidic layer wafer and the coated control wafer into an oven for 30 minutes at 85°C.

7) Carefully remove peel the solidified PDMS off of the control wafer.

8) Cut out individual devices using a razor blade and punch inlets.

9) Align devices onto spincoated microchannel + fluidic layer wafers and place in the oven for at least 1.5 hours at 85°C.

10) Cut out completed devices using a razor blade by tracing the boundaries.

11) Punch inlets of the fluidic layer.

12) Carefully remove the PDMS layer between the fluidic layer and the control layer by using a pair of sharp tweezers.

Device bonding

1) Clean devices with an alconox solution and rinse thoroughly with DI water.

2) Rinse with 70% Ethanol and dry using a filtered air stream.

3) Clean a 22 x 40 mm glass coverslip (Fisher) using 70% Ethanol and dry using a filtered air stream.

4) Place cleaned device on glass coverslip and make sure no air bubbles are present.

5) Place the device in an oven set at 85°C overnight to induce a strong, reversible bond.

2.3 Development of a microfluidic device for studying directed migration phenomena in cancer cells

In this subsection, we will outline the development and rationale behind the microfluidic device used in chapter 4 (**Fig 4.1, Fig. 4.2**). We will again enumerate a set of device requirements we satisfied in order to achieve a functioning device. We will end with a discussion of the design principles we incorporated to meet these requirements.

2.3.1 Device requirements

Many of the primary requirements of this device were similar to those described for the device used in section **2.2**. These requirements were generating reproducible gradients of soluble chemicals across cancer cells in a high throughput manner. The secondary requirement of low shear stress across cells also applied. However, matching the time scales of cell responses in this assay presented new challenges. The goal of this device was to study the mechanisms of chemotaxis in MTLn3 cells to gradients of EGF. The response kinetics of MTLn3 cells to EGF is on the order seconds to minutes[54], an order of magnitude faster than the response kinetics of HeLa cells to rapamycin seen in the previous device[141]. Therefore, a similar gradient introduction scheme would not work in this system, as early cell responses could be missed across the cell population. We will outline the changes we made to the device design to accommodate these kinetics in the next section.

2.3.2 Device design

To ensure that all cells received the stimulus at the same time scale, we introduced top down elastomeric valves between the microchannels and the source and sink (**Fig 4.2**). These valves allowed us to functionally isolate the microchannels while pre-establishing the source and sink. Once the source and sink were at steady state,

opening the valves enabled the simultaneous formation of the gradient by diffusive flux across all channels. Thus, all cells receive the stimulant at the same time which enables an accurate comparison of the response kinetics.

We also modified the upstream flow balancing scheme to reduce the potential contamination of the sink by the source stream due to upstream diffusion. We placed a shunt at the junction of the source and sink which connects directly to the outlet (**Fig 4.2**). By carefully optimizing fluidic resistances in our design, any pressure imbalances between the source and sink input streams are transmitted to the shunt and do not influence downstream gradient. Moreover, any contamination between the source and sink streams is transported through the shunt and is not propagated downstream.

2.3.3 Device fabrication protocol

The device fabrication protocol of this device is quite similar to that in section **2.2.3**, however, we made several modifications to incorporate valves between the microchannels and the source and sink.

Microchannel layer

1) Clean a 3 inch Silicon wafer using spray bottles positioned over an appropriate waste container in the following order- 1) Acetone, 2) Isopropanol, and 3) DI water.

2) Dry wafers using nitrogen air stream and place on hotplate >100 °C for at least 5 minutes to ensure all water has evaporated.

3) Spincoat SU-8 3005 (Microchem) at 3000 rpm for 30 seconds.

4) Soft bake the wafer on a hotplate at 95°C for at least 10 minutes.

5) Expose the wafer using a mask aligner using a constant energy of 1000 mJ/cm^2.

(We utilize a long pass UV quartz filter (Omega Filters) which provides straighter channels but require more exposure energy.)

6) Post exposure bake for 1 hour at 95°C.

7) Develop in SU-8 developer (Microchem).

8) Hard bake for at least 1 hour at 200°C.

Fluidic layer

1) Use the microchannel layer wafer created above and repeat steps 1 and 2 above.

2) Spincoat SPR-220-7 (Megposit) at 730 rpm for 30 second on the silicon wafer.

(note- silane coating may improve the adhesion of SPR-220-7)

3) Soft bake for 8 minutes at 115°C.

4) Allow the SPR-220-7 coated wafer to rehydrate at room temperature for at least 1 hour.

5) Expose the wafer using a mask aligner using a constant energy of 600 mJ/cm^2. Care must be taken to align the fluidic layer to alignment marks put into the microchannel layer.

6) Develop using a 1:4 dilution of AZ400K developer (Clariant).

7) Round and hard bake channels by baking at 200°C for 5 hours using a slow ramp (180°C/hr)

Source and Sink layer

1) Use the microchannel + fluidic layer wafer created above and repeat steps 1 and 2 from the microchannel layer protocol for cleaning.

3) Spincoat SU-8 3050 (Microchem) at 1000 rpm for 30 seconds.

4) Soft bake the wafer on a hotplate at 95°C for 2 hours.

5) Expose the wafer using a mask aligner using a constant energy of 3000 mJ/cm^2. Be sure to align the source and sink layer with the previous two layers using a third set of alignment marks.

(We utilize a long pass UV quartz filter (Omega Filters) which provides straighter channels but require more exposure energy.)

6) Post exposure bake for 1 hour at 95°C.

7) Develop in SU-8 developer (Microchem).

8) Hard bake for at least 1 hour at 200°C.

PDMS device fabrication

1) Prepare a 8:1 and 20:1 mixture of component A to component B of RTV615 (Momentive) and mix in weight boats for at least 5 minutes.

2) Remove air bubbles with a vacuum chamber.

3) Treat the microchannel + fluidic layer wafer and the control layer wafer with chlorotrimethylsilane (TMCS) by placing wafers into a vacuum dessicator and placing a

few drops of TMCS into a bottle cap. Evacuate the chamber and let sit for at least 20 minutes.

4) Spincoat the 20:1 mixture onto the microchannel + fluidic layer wafer at 390 rpm for 60 seconds.

5) Place the control layer wafer into a heat resistant container and pour the 8:1 mixture on top.

6) Place the spincoated microchannel + fluidic layer wafer and the coated control wafer into an oven for 30 minutes at 85°C.

7) Carefully remove peel the solidified PDMS off of the control wafer.

8) Cut out individual devices using a razor blade and punch inlets.

9) Align devices onto spincoated microchannel + fluidic + source and sink layer wafer and place in the oven for at least 1.5 hours at 85°C.

10) Cut out completed devices using a razor blade by tracing the boundaries.

11) Punch inlets of the fluidic layer.

Device bonding

1) Clean devices with an alconox solution and rinse thoroughly with DI water.

2) Rinse with 70% Ethanol and dry using a filtered air stream.

3) Clean a 22 x 40 mm glass coverslip (Fisher) using 70% Ethanol and dry using a filtered air stream.

4) Place cleaned device on glass coverslip and make sure no air bubbles are present.

5) Place the device in an oven set at 85°C overnight to induce a strong, reversible bond.

2.4 Discussion

The microfluidic devices described in section **2.2** and **2.3** (Illustrated in **Fig 3.2** and **Fig 4.2**, respectively) will be utilized in **Chapters 3** and **4**, respectively. These microfluidic device designs enable the investigation of a new set of questions in the mechanisms of directed migration by allowing sensitive control of cellular microenvironments. We suggest that they will be applicable to a variety of cell types and will allow the general exploration of graded processes in cell signaling.

Chapter 3. Synthetic spatially graded Rac activation drives cell polarization and movement

3.1 Introduction

Directional motility is an intrinsic ability of many eukaryotic cells to migrate to predetermined locations in an efficient manner. Migration bias is tuned by the detection of various guidance cues that often form spatial gradients. The extracellular gradients of diffusing or surface bound ligands can lead to spatially graded occupancy of extracellular receptor[10]. The spatial asymmetry in receptor occupancy is subsequently translated into an intracellular gradient of polarity effectors which can modify cytoskeleton and lead to the development of an asymmetric cell morphology with functionally distinct front and rear 'compartments'. Remarkably, many cell types can accurately detect less than a 5% difference between ligand concentration at the cell front and back[10, 23, 142]. This exquisite sensitivity suggests that intracellular amplification of extracellular cues may be necessary. Indeed, various groups have demonstrated the existence of local positive feedback loops[143-146] as well as mutual inhibition between different regulators[147, 148] as likely candidates for response amplification. However, recent studies have also shown that directional motility can still be achieved, albeit less efficiently, when once thought indispensable molecules involved in putative amplification mechanisms are removed[12, 13]. Thus the various functions of signaling components associated with directed migration still need to be elucidated.

An attractive method for resolving the roles of signaling network components in both spatial cue sensing and directed cell motility is direct activation of these components in a spatially constrained and rapid manner, independent from initiation of upstream, receptor-level signaling. Utilizing this principle, a variety of studies have used optical activation to identify the small Rho GTPase Rac[148-153] , cofilin[154], thymosin □4[155], and calcium[156] as key components which are sufficient to direct cellular motility. However, an important caveat to these studies has been the reliance upon highly localized activation that can create artificial regional amplification of target protein activity. In contrast, in more physiological settings, a cell processes a shallow gradient of an external cue into a graded intracellular response, as reflected in polarized effectors[11], including those of the small Rho GTPase family[63-65]. Thus it remains unclear if an induced shallow gradient of an active motility signaling component is capable of reconstituting cell polarization and motility. In particular, it is unknown if such perturbations are sufficient to override or enhance endogenous intracellular signaling of the same component. Finally, localized activation of signaling processes presents considerable challenges to quantitative analysis and coupling to detailed computational models developed to describe more natural, spatially distributed signaling events.

To address these questions, we created microfluidic devices permitting generation of precise gradients of extracellular cues[133] and interfaced them with a rapamycin induced dimerization system[157]. In this system, the addition of rapamycin leads to dimerization of two intracellularly transduced molecular components, FK506 binding protein (FKBP)

and the rapamycin binding domain of FKBP-rapamycin-binding protein (FRB)[158]. Localization and signaling motifs can be linked to either domain, allowing spatial-temporal control of protein function. We used our combined system to study the effects of a rapidly induced intracellular gradient of activated Rac, an important regulator of cell polarity[59] and previously shown to induce migration when locally activated[148-153].

3.2 Results

3.2.1 System design

To directly activate endogenous Rac, we introduced two constructs into HeLa cells, a cytoplasm localized effector unit consisting of YFP tagged TIAM1, a Rac GEF, conjugated to FKBP (YF-TIAM1) and an anchor unit at the cell membrane, Lyn_{11}-FRB (LDR). The introduction of rapamycin dimerizes these modified molecular components, thereby bringing TIAM1 in close proximity to the cell membrane where it activates endogenous Rac[157] (**Fig. 3.1a**). Due to the chemical nature of the activation, this system is amenable to generation of a gradient of Rac activity through microfluidic production of rapamycin gradients. Microfluidic tools have recently been used for the control of complex gradients of extracellular cues[85, 128, 133], cellular localizations[159, 160] and shaping cell morphologies[140, 161].

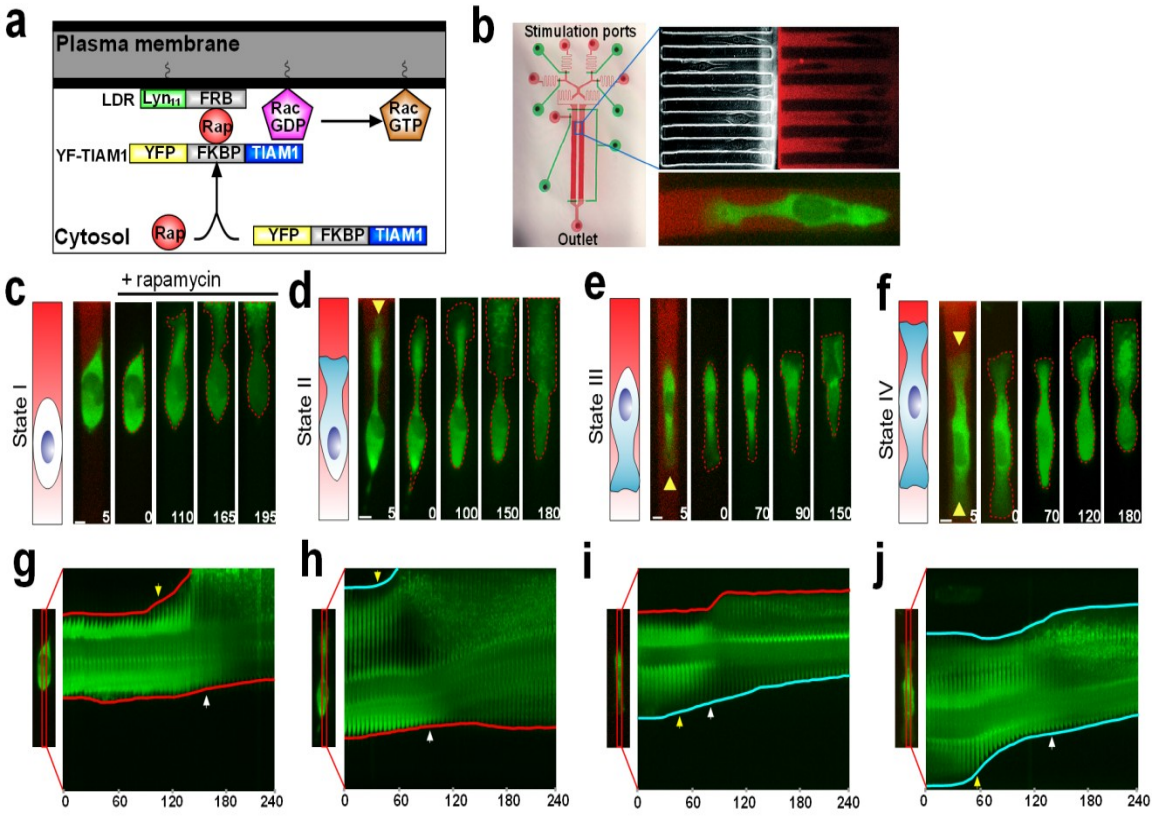

Fig 3.1: Graded activation of Rac directs cellular polarity.

(**a**) A schematic of the mechanism of Rac activation by rapamycin induced heterodimerization. (**b**) The microfluidic device used to generate linear gradients of rapamycin with a sample image of the microchannels seeded with individual HeLa cells and the corresponding gradient visualized with Alexa 594 dye. Ports are labeled according to function. The red layer of the device is the fluid flow layer, while the green layer is the control valve layer. Alexa 594 dye is used to visualize the gradient (red) in all subsequent images. A sample image of a cell transfected with the Rac activator, YF-TIAM1 experiencing a gradient of rapamycin is shown below. (**c-f**) Four polarity states observed after the attachment period with respect to the direction of the imposed rapamycin gradient and associated polarization responses to the gradient of rapamycin. Images are rotated by 90° to aid in visualization. Cartoons illustrate the polarity of the associated state and the direction of the gradient. The green color indicates expression of YF-TIAM1. Yellow arrows denote the initial direction of polarity. The rapamycin gradient is shown in the 5 minute image and removed in subsequent images for clarity. Red dotted lines highlight evolving changes in cell morphology. Times are in minutes. Scale bars, 10 μm. (**g-j**) Kymographs taken across cell centers (specified in accompanying image) illustrating the morphological changes of the corresponding cells in **c-f** over the experimental period. Blue lines trace initially polarized faces while red lines trace initially unpolarized faces. Yellow arrows denote the initial response time and their location indicate which cell face was the first to change in the gradient. White arrows indicate the late polarization time. Times are in minutes.

We applied a previously developed strategy for imposing diffusion based linear gradients onto cells housed within narrow channels[133, 140]. Specifically, the devices contained a series of 6 μm tall microchannels for cell experimentation, flanked by 130 μm tall main flow-through channels (**Fig. 3.2a**). Actuation of flow led to the development of a linear gradient across the shallow channels due to uneven stimulus concentration in the flow-through channels (**Fig. 3.1b**). The microchannels were designed to be on the order of a cell diameter to relegate cells to a uniaxial phenotype (**Fig. 3.1b**). HeLa cells introduced into the microchannels settled into random locations and after a 3-4 hour attachment period were categorized into different polarity states according to the existence of a lamellipodium (State I- no lamellipodium) and its direction (State II- lamellopodium towards the high side of the gradient, State III- lamellipodium towards the low side of the gradient, State IV- lamellopodia towards both sides) (**Fig. 3.1c-f**). The overall distribution of phenotypes was skewed towards cells with single leading edge lamellipodium, indicating an intrinsic preference for directed motility (**Fig. 3.2b**).

3.2.2 Direct generation of active Rac gradients

To evaluate HeLa cell responses to synthetic generation of an intracellular gradient of active Rac, we exposed cells to a linear gradient of rapamycin (0 - 2 nM across the channel or 0.01 nM/μm; yielding front/back concentration differences ranging from ~15-92% across varied cell lengths) visualized by Alexa 594, a fluorescent dye with a similar molecular weight (**Fig. 3.1b** and **Fig. 3.2c**). We chose this concentration range to avoid saturating the FKBP-FRB system with rapamycin (K_D = 12 nM[162]). One

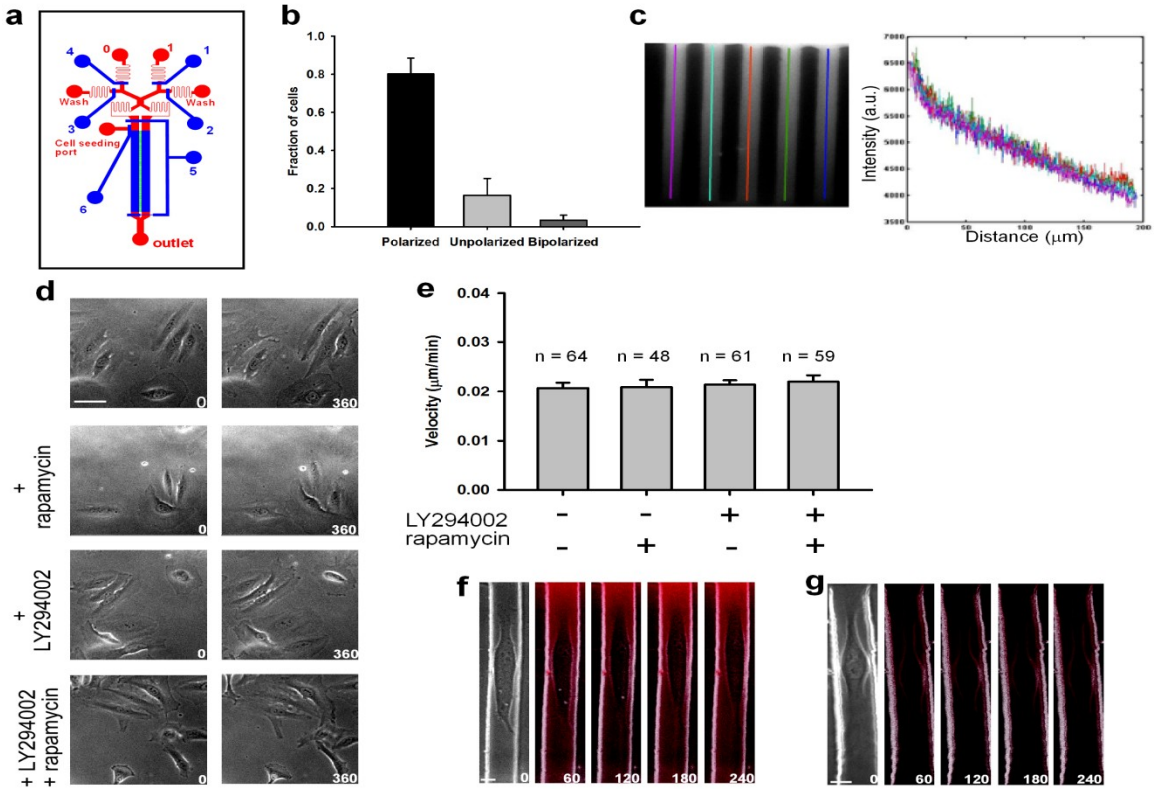

Fig 3.2: Characterization of the microfluidic device and motility controls.

(**a**) The schematic of the microfluidic device used in experiments. The layer labeled in blue is the control layer containing fluidically actuated valves used to control the separate fluidic layer below, labeled in red. The green layer indicates the region where the microchannels are housed and where cells are seeded. (**b**) Quantification of the fractions of HeLa cell polarity phenotypes observed after a four hour attachment period. Data are presented as the mean from n = 8 experiments, with error bars representing the standard error of the mean (SEM). (**c**) Quantification of the gradients of Alexa 594 dye in the microchannels generated to visualize the distribution of rapamycin, with colored lines quantifying fluorescence intensity to demonstrate the linearity of the gradient profiles and consistency of the gradients in multiple adjacent channels. (**d**) Images of HeLa cells on fibronectin coated glass before and after the addition of indicated chemicals. Times are in minutes. Scales bars, 50 μm. (**e**) Average velocities of HeLa cells in various treatment conditions. There is no significant difference between conditions. Number of samples are indicated. (**f-g**) Representative examples of untransfected HeLa cells experiencing a gradient of the dye as in (**c**), with added rapamycin (**e**) and without added rapamycin (**f**). The cells show limited morphological changes through a four hour period. Time values are in minutes. Scale bars, 10 μm.

consequence of using these concentration values was a slow-down of the response times as compared to previously reported values for saturating uniform rapamycin inputs[157]. However, the slower response times allowed a better resolution of the effects of gradually accumulating Rac activity and were far below those reported to affect the function of the mammalian target of rapamycin (mTOR)[163]. As a control, we compared basal cell motility with and without rapamycin and found that the addition of rapamycin had negligible effects (**Fig. 3.2d-e**). We tracked both the initial state and subsequent cell responses by imaging over a four hour time period.

Strikingly, we found that the shallow linear gradient of rapamycin could trigger and direct motility of cells in all initial polarity states in the direction up the gradient (**Fig. 3.1c-f**). Unpolarized (state I) and bipolar cells (state IV) demonstrated symmetry breaking with either the establishment of a leading edge or the enhancement of one lamellipodium and retraction of the other, respectively (**Fig. 3.1c, f**). Cells already polarized in the direction of the gradient (state II), exhibited widening and extension of the leading lamellipodium and movement up the gradient (**Fig. 3.1d**). Interestingly, cells initially oriented in the direction opposite of the gradient (state III) repolarized (**Fig. 3.1e**). In all states, the initiation of migration was followed by a pronounced enhancement of cell polarity (**Fig. 3.1g-j**). The directed cell polarization and migration responses were not observed in untransfected cells (**Fig. 3.2f**), or if the rapamycin gradient was not imposed (**Fig. 3.2g**). For validation of our system, we applied linear gradients of rapamycin to similarly transfected MTLn3 cells, a rat mammary adenocarcinoma line used to assay chemotaxis to epidermal growth factor (EGF) in vitro[79] and in vivo[164] (**Fig.**

3.3). MTLn3 cells exhibited initial polarity states similar to those seen in Hela cells and polarized towards gradients of rapamycin (**Fig. 3.3**). Our data suggests that our system is applicable across multiple cell types and can be used to study signaling pathways regulating chemotaxis.

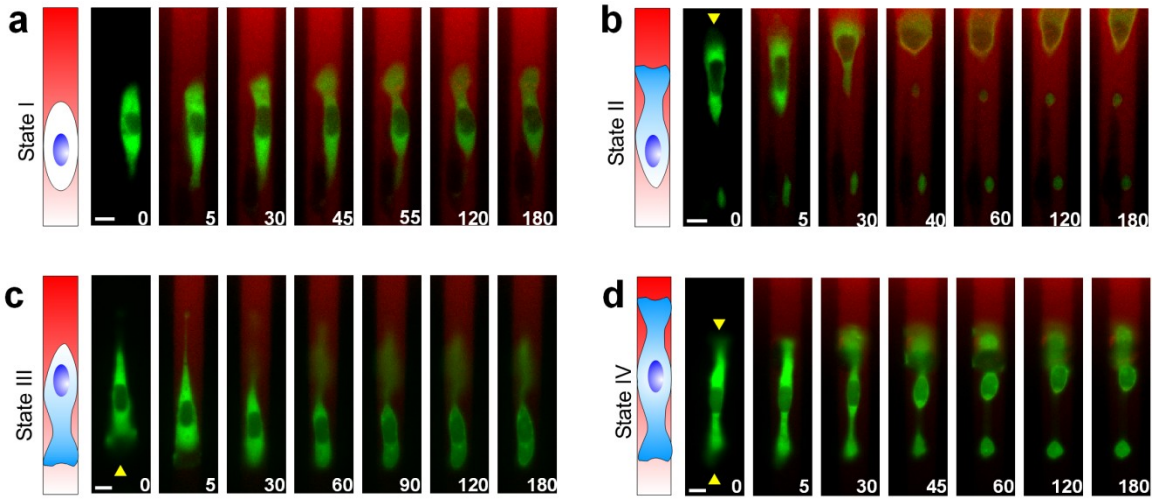

Fig 3.3: MTLn3 cell responses to rapamycin gradients.

(**a-d**) MTLn3 cells in various initial polarity states, similar to those seen in HeLa cells, become polarized towards gradients of rapamycin. The green color indicates expression of YF-TIAM1, while the red color indicates the rapamycin gradient. Yellow arrows indicate initial protrusions. Times are in minutes. Scale bars, 10 μm.

To verify that the externally imposed rapamycin gradient was translating into a graded change in active Rac across cells, we carried out two control experiments. First, we sought to confirm that the Rac activator, YF-TIAM1, translocated to the membrane in a graded fashion over time. Our results above indicated that translocation of YF-TIAM1 results in the formation of ruffling and substantial changes in cell morphology which

obscure translocation, therefore we used an YFP tagged FKBP (YF) without TIAM1 to assess translocation. YF was previously shown to translocate with similar kinetics to YF-TIAM1[165] and therefore could serve as a suitable proxy. We tracked the membrane to cytoplasm ratio of fluorescence intensities across the length of cells in a gradient of rapamycin over time and found that membrane translocation of YF was increasing in a graded manner, with higher translocation towards the high side of the gradient (**Fig. 3.4a-f**). We did not observe a similar response when DMSO was substituted for rapamycin (**Fig. 3.4g-h**). In both conditions we did not observe any significant morphological changes, indicating that translocation of FKBP constructs without effectors does not perturb morphology. Having verified that the rapamycin gradient induced graded membrane translocation of FKBP constructs, we used a Raichu Rac FRET sensor[166] to monitor the resulting changes in Rac activity. In these experiments, we used an mCherry tagged FKBP-TIAM1 (MCHF-TIAM1) to activate Rac. At a basal level before stimulation, state I cells did not show polarized Rac activity (**Fig. 3.5a**) while state II and state III cells exhibited higher levels of Rac at lamellipodia (**Fig. 3.5b,c**). Upon introduction of the rapamycin gradient, we observed increases in Rac activity in the direction of the gradient in all cells, while state III cells exhibited an additional decrease in Rac activity in the original lamellipodium (**Fig. 3.5a-c**). We quantified the average Rac activity across cells over time and found that there was a gradual and spatially graded increase in Rac activity in all cell states (**Fig. 3.5d-f**). State III cells in particular exhibited a sharp increase in Rac activity in the newly formed protrusion and decrease in the initial opposite facing protrusion (**Fig. 3.5f**). As a control, we quantified Rac activity across cells which did not express the Rac activator, MCHF-TIAM1 but had expression of the

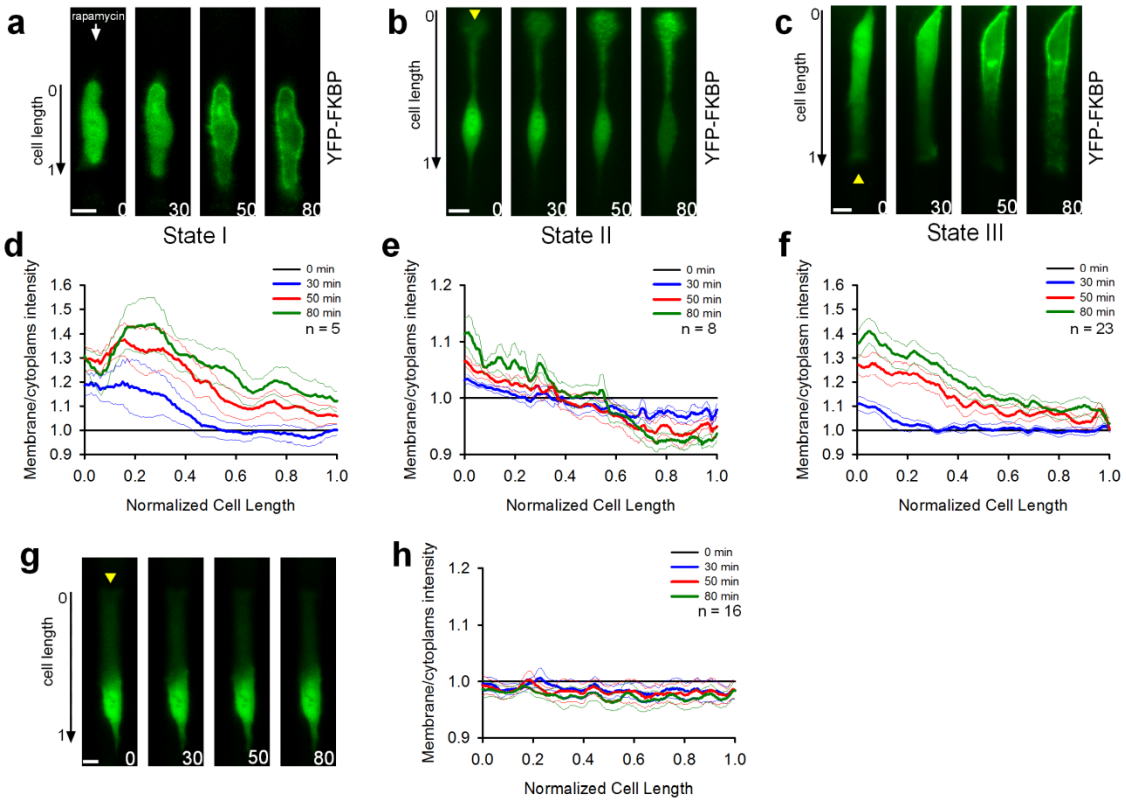

Fig. 3.4: Quantification of graded membrane translocation of FKBP constructs.

(**a-c**) HeLa cells in states I-III transfected with YFP-FKBP exposed to a gradient of rapamycin from top to bottom. Time 0 is chosen as 30 minutes before translocation. Cell length plot indicates axis of quantification in plots (**d-f**). Yellow arrows indicate initial protrusions. Times are in minutes. Scale bars, 10 μm. (**d-f**) Quantification of the average membrane to cytoplasm intensity ratio across state I-III cells over time. Ratios after time 0 are normalized to the membrane to cytoplasm fluorescence intensity ratio at time = 0 (shown in black). Thinner colored lines indicate S.E.M of corresponding ratio profiles. Numbers of samples are indicted. (**g**) Control cells exposed to a gradient of DMSO instead of rapamycin do not show translocation. Cell length plot indicates axis of quantification in (**h**). Times are in minutes. Scales bars, 10 μm. (**h**) Quantification of the membrane to cytoplasm intensity ratio across control cells over time. The ratio fluctuates around the

Rac FRET sensor. Under these conditions, we did not observe any significant changes in Rac activity over time in gradients of rapamycin (**Fig. 3.5g,h**). Overall our results

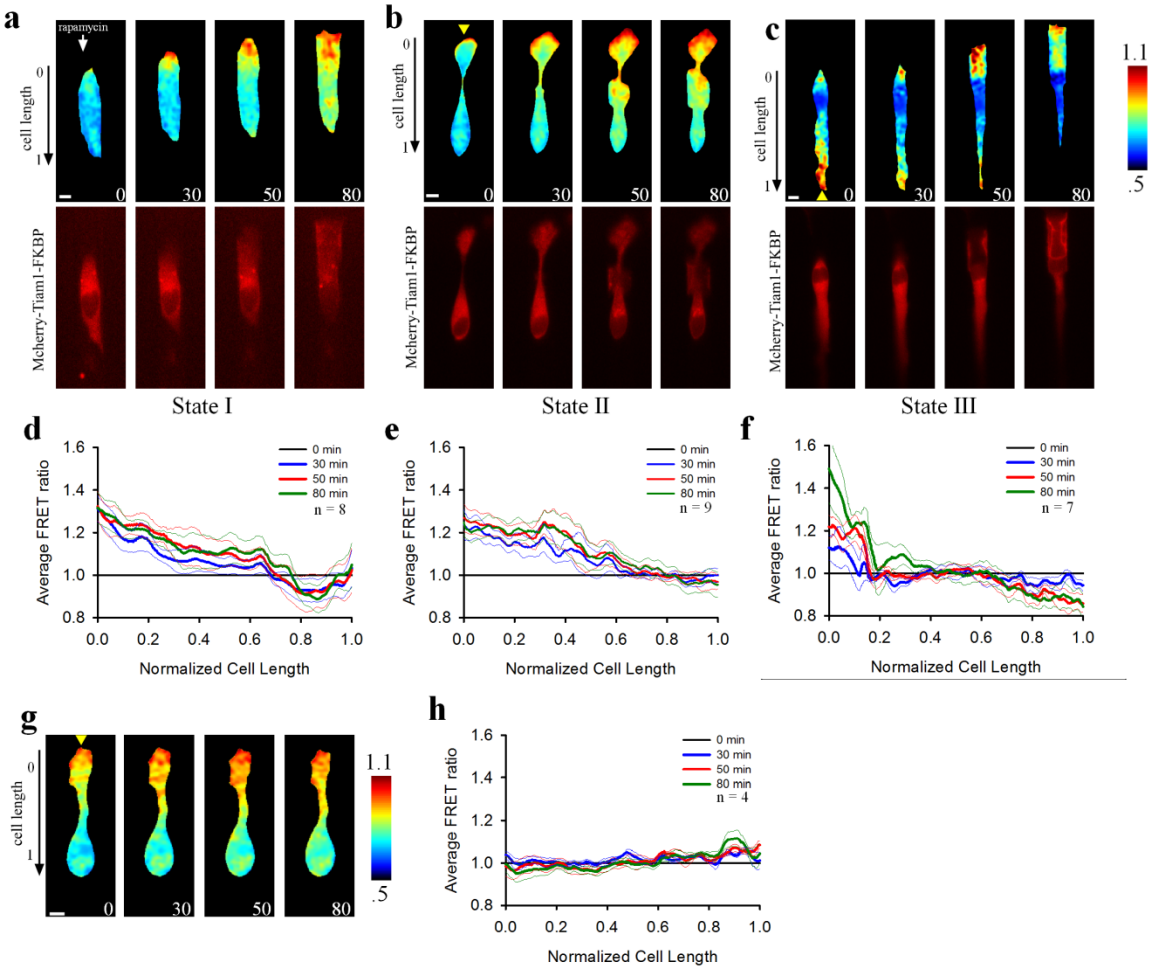

Fig. 3.5: Quantification of graded Rac activity

(**a-c**) HeLa cells in state I-III transfected with a Raichu-Rac FRET probe and an mCherry tagged FKBP-TIAM1 (MCHF-TIAM1) experiencing a gradient of rapamycin from top to bottom over time. Time 0 is chosen as 30 minutes before morphological changes in MCHF-TIAM1 images. Cell length plot indicates axis of quantification in plots (**d-f**). Yellow arrows indicate initial protrusions. Times are in minutes. Scales bars, 10 μm. (**d-f**) Quantification of average FRET activity across state I-III cells over time in gradients of rapamycin. FRET profiles after time 0 are normalized to the initial profile at time 0 (shown in black). Thinner colored lines indicate S.E.M of corresponding average profile. Numbers of samples are indicated. (**g**) Control cells that do not express the Rac activator (MCHF-TIAM1) exposed to gradients of rapamycin. Only slight fluctations in Rac activity were detected. Cell length plot indicates axis of quantification in (**h**). Times are in minutes. Scale bars, 10 μm. (**h**) Quantification of the average FRET profile across control cells over time. FRET activity fluctuates around the basal level at time 0. Numbers of samples are indicated.

suggested that an exogenously applied linear gradient of rapamycin could result in a graded increase in Rac activity which was sufficient to direct motility and polarization of cells from a variety of pre-existing polarity phenotypes.

For further validation of our system, we compared cellular responses to graded rapamycin with responses to uniform rapamycin stimulation. Cells given a uniform stimulus for the entire experimental period displayed extensive uniform flattening with little net motility (**Fig. 3.6a**). This result was in agreement with previous experiments showing that differentiated HL-60 cells exposed to spatially uniform stimulation of Rac displayed membrane ruffling around the entire cell periphery[145]. For a more detailed comparison of the effects of graded and uniform Rac activation, we exposed state II cells to a rapamycin gradient for 2 hours, subsequently followed by uniform stimulation (2 nm) for 3 hours thereafter. As expected, cells polarized and moved in a biased fashion during gradient stimulation; however upon the switch to uniform stimulation, cells started forming protrusions at the rear and showed a decrease in the length of the front (**Fig. 3.6a-d**). This effect indicated the importance of persistent gradient input but might also reflect a gradual saturation of rapamycin binding sites after prolonged treatment. We explored the latter possibility by running the converse experiment, exposing cells to spatially uniform rapamycin (2 nm) for 2 hours followed by a rapamycin gradient for 3 hours (**Fig. 3.6e**). Protrusions developed on both sides of cells during uniform stimulation, and subsequently could not be biased by the gradient (**Fig. 3.6e**). However, cells exposed to a lower uniform stimulation (1 nm) were able to polarize towards the ensuing rapamycin gradient (**Fig. 3.6f**). In combination, these results indicate that cells can be guided by rapamycin gradients as long as the average rapamycin concentration

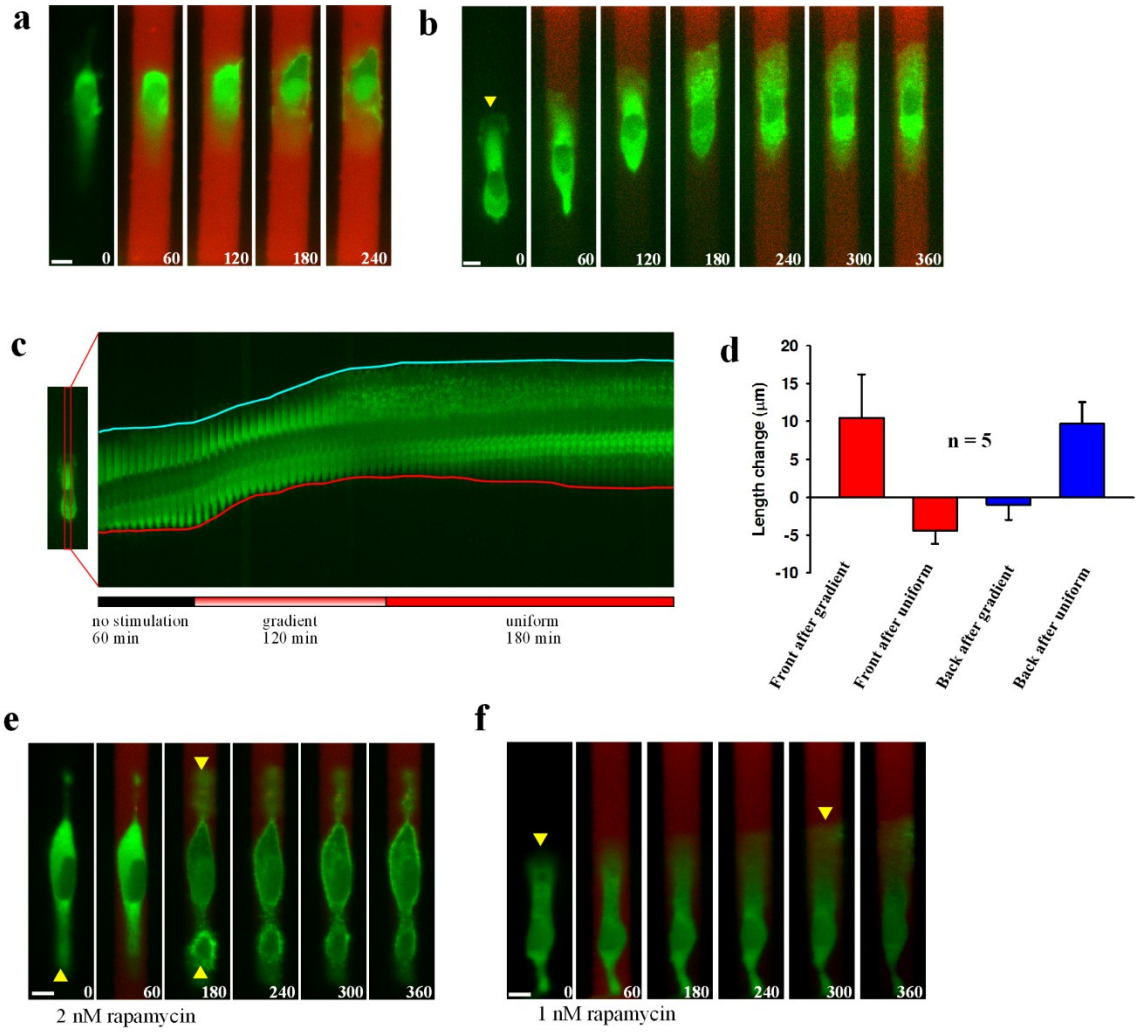

Fig. 3.6: Comparison between graded and uniform rapamycin stimulation.

(**a**) Cells exposed to a uniform concentration of rapamycin (2 nM) flatten and do not show any directed polarity. (**b**) Cells observed for one hour without stimulation and subsequently exposed to a gradient of rapamycin for a two hour period, followed by a switch to a uniform stimulation (2 nM) for three hours. The gradient directs cell motility and amplifies the existing lamellipodium. The switch to a uniform stimulation leads to a protrusion formation in the rear of the cell and retraction of the previously amplified lamellipodium. Times in minutes. Scale bars, 10 µm. (**c**) A kymograph taken from the cell center (specified in accompanying image) depicting the morphological changes of the cell shown in panel (**b**) over various treatment periods. The blue line traces the front of the polarized cell, whereas the red line traces the unpolarized face. (**d**) Quantification of the length changes in cell front and back during the rapamycin gradient exposure and after the switch to uniform rapamycin stimulation. Numbers indicate total number of cells. Error bars are SEM. (**e-f**) Cells observed for one hour, exposed to uniform 2 nM rapamycin (**e**) or uniform 1 nM rapamycin (**f**) for two hours, and a gradient for three hours. Cells given a 2 nM uniform dose exhibit protrusions on both sides, while cells given a 1nM uniform dose can still be guided by the gradient. Yellow arrows indicate initial and final enhanced protrusions. Times are in minutes. Scale bars, 10µm.

does not exceed a saturating level. Below, we explore the effects of the rapamycin dose and exposure time on cell responses in greater detail. Our results suggest that the spatial restriction of Rac activity within a cell is important for maintaining polarization.

3.2.3 Mathematical modeling of graded Rac inputs

To better address the simplified, yet non-intuitive, nature of our imposed graded Rac signaling, we developed a mathematical model of cell polarity. The model is based on a simple scheme of Rac-RhoA-Cdc42 small GTPase and Phospoinositide interactions, expanding on earlier modeling studies[167, 168] (Modeling details found in Supporting Information). The model made three important qualitative predictions: a) a spatially graded activation input can trigger initial polarization of Rac activity (**Fig. 3.7a**), b) the timing of that initial Rac polarization is strongly dependent on the input gradient and weakly dependent on the average input (**Fig. 3.7b**), and c) antagonism between the activities of Rac and Rho small GTPases can trigger a phase transition-like change to a substantially more asymmetric polarization, which can be stably maintained as long as the activity of Rac remains high enough (**Fig. 3.7a**). This transition will be addressed in more detail below. See Supporting information for model details. These predictions could be directly examined in our experimental setup.

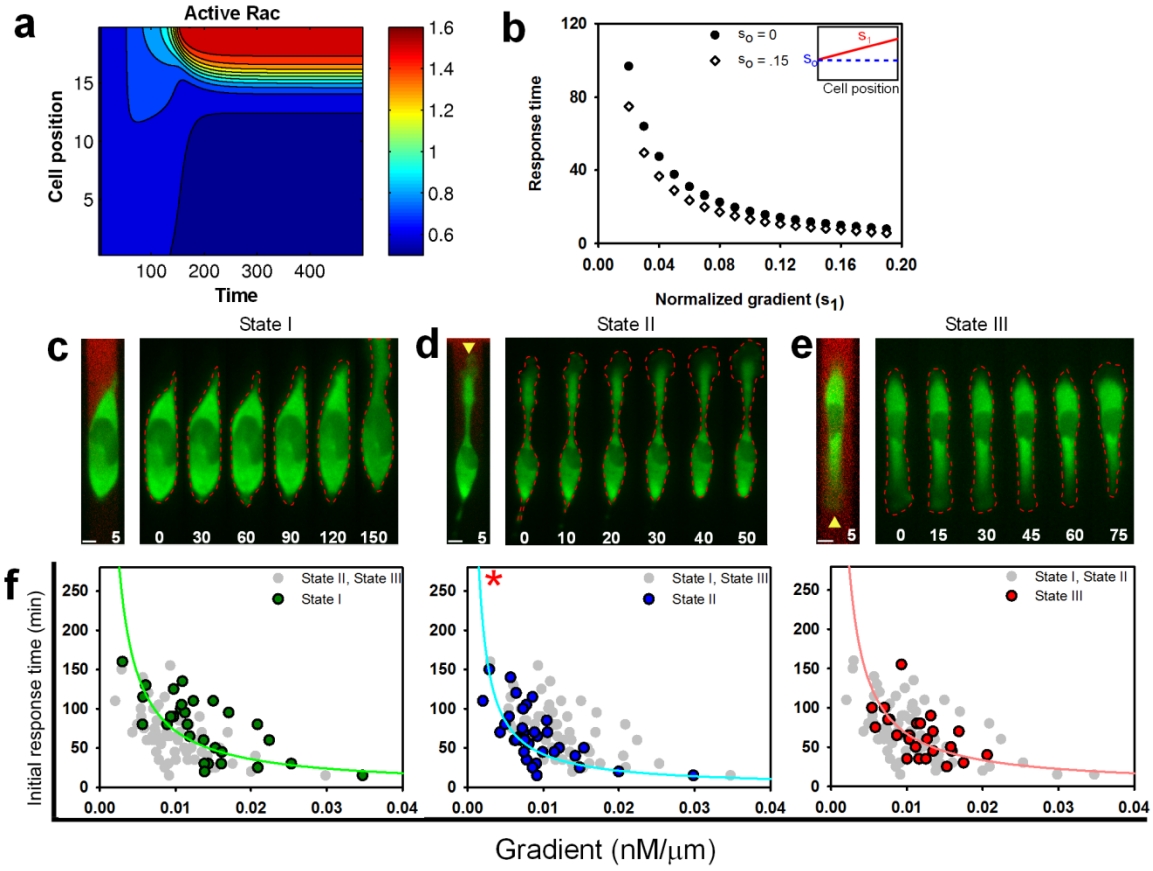

Fig. 3.7: Analysis of the initial response time.

(**a**) Sample kymograph of the mathematical model simulation under graded Rac stimulation. (**b**) Model response time vs. normalized gradient (s_1) for two different values of s_o (input). (**c-e**) Kymographs chronicling typical changes in cell morphology seen during early time periods. The first image before each kymograph depicts the gradient (red) that the cell is experiencing as visualized with Alexa 594 dye. The gradient is not shown in resulting images to promote clarity of morphological changes. The green color indicates expression of YF-TIAM1. Red dotted lines highlight evolving cell boundaries. Yellow arrows indicate initial polarities. Times are in minutes. Scale bars, 10 μm. (**f**) The dependence of initial response times on gradient values. States are color coded; state I (green) n = 29, state II (blue) n = 37, and state III (red) n = 27. In each plot, the colored dots highlight the dependence of that particular state while the grey dots illustrate where the response times of the other states fall. Data is fitted based on simulation results. Spearman correlation coefficient, State I = -.679, State II = -0.655, State III = -0.583. The asterisk indicates a statistically significant difference (State II vs. State I, $p < 1e\text{-}4$, State II vs. State III, $p < 1e\text{-}3$) between the state II curve vs. the other states. There is no statistical difference between state I and state III ($p = 0.54$). Both tests were carried out using an F test.

3.2.4 Analysis of Rac gradient steepness on timing of cellular responses

To validate the model predictions, we next examined the correlates of the initiation of directed cell migration and their dependencies on the local gradient and average value of rapamycin input. HeLa cell responses were characterized by either the retraction of a leading lamellipodium in cells polarized in the direction opposite that of the gradient (state III), or extension of a pre-existing (state II) or new (state I) lamellipodium in the direction of the gradient (**Fig. 3.7c-e**). To quantitatively evaluate these effects, we examined the width and length of the front and rear sides of cells in all states through the entire stimulation period, along with the respective concentrations experienced at each side (**Fig. 3.8**). Cells that exhibited bipolar phenotypes (state IV) were relatively rare (**Fig. 3.1f** and **Fig. 3.2b**) and therefore were excluded from subsequent analysis. Our analysis revealed that these initial directed migration response times, in agreement with the model predictions, were indeed inversely dependent on the steepness of the rapamycin gradient across each cell (**Fig. 3.7f**). This trend was seen across all polarity states (Spearman correlation coefficients; -0.679, -0.655, and -0.583 for state I, II, and III, respectively). Similar dependencies were also observed in MTLn3 cells (**Fig. 3.9a-c**). The initial response times of state I cells also showed a discernible but much weaker dependency on the average rapamycin concentration, consistent with the model predictions. Cells in states II and III had relatively weaker dependencies (**Fig.3.10a-c**, Spearman correlation coefficients; -0.582, -0.478, and -0.377 for state I, II,

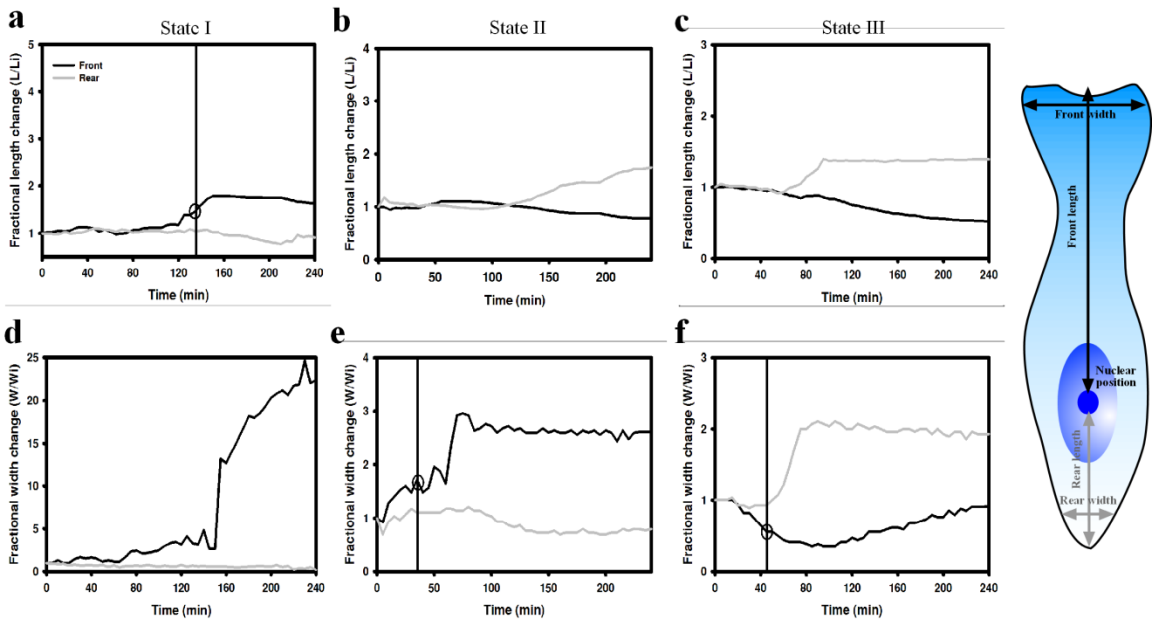

Fig. 3.8: Tracking changes in cell morphology to assay the initial response time**.**

The plots correspond to the cells in different states, as seen in Figure 2. Various morphology metrics are illustrated in the schematic accompanying the graphs. Fractional values of the metrics are shown, with values normalized to those at the beginning of the analysis. (**a-c**) Tracking of changes in the lengths of the cell front and back over time during gradient stimulation. (**d-f**) Tracking of changes in widths of the cell front and back. The time to reach 20% of the maximum magnitude of the first morphological response to gradient exposure was taken as the initial response time. The drop line indicates the initial response time, while the circle indicates the intercept between the dropline and the corresponding metric value.

and III, respectively). State II cells had consistently shorter initial response times for any given gradient steepness when compared to those in state I and state III (**Fig. 3.7f** and **Fig. 3.11**) (F test- State II vs. State I, $p < 0.0001$, State II vs. State III, $p < 0.001$), while state I and III cells behaved similarly (State I vs. State III, $p = 0.54$). For example, when comparing the average initial response times at a gradient of .01nm/μm +/- .001, state II cells had an average initial response time of 51 minutes, while state I had an average of 98 minutes and state III had an average of 71 minutes. These results suggest that cells are

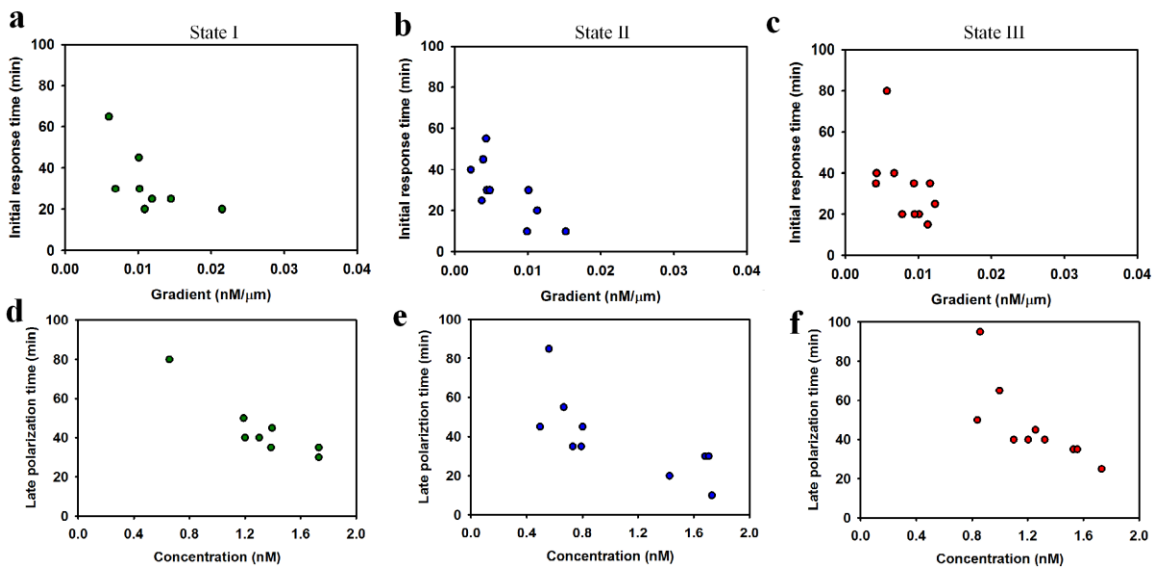

Fig. 3.9: Initial response and late polarization times of MTLn3 cells.

The plots correspond to the cells in different states, as seen in Figure 2. Various morphology metrics are illustrated in the schematic accompanying the graphs. Fractional values of the metrics are shown, with values normalized to those at the beginning of the analysis. (**a-c**) Tracking of changes in the lengths of the cell front and back over time during gradient stimulation. (**d-f**) Tracking of changes in widths of the cell front and back. The time to reach 20% of the maximum magnitude of the first morphological response to gradient exposure was taken as the initial response time. The drop line indicates the initial response time, while the circle indicates the intercept between the dropline and the corresponding metric value.

able to rapidly make migration decisions in the presence of Rac activity gradients overlapping with their initial polarization state. Together, our data demonstrates that the magnitude of active Rac gradients can influence the timing of the onset of directed cell motility.

Besides the initiation of biased cell migration, the spatially graded activation of Rac eventually triggered a striking enhancement in cell polarization, with a substantial enlargement of the directed leading lamellipodium (**Fig. 3.12a**). This morphological

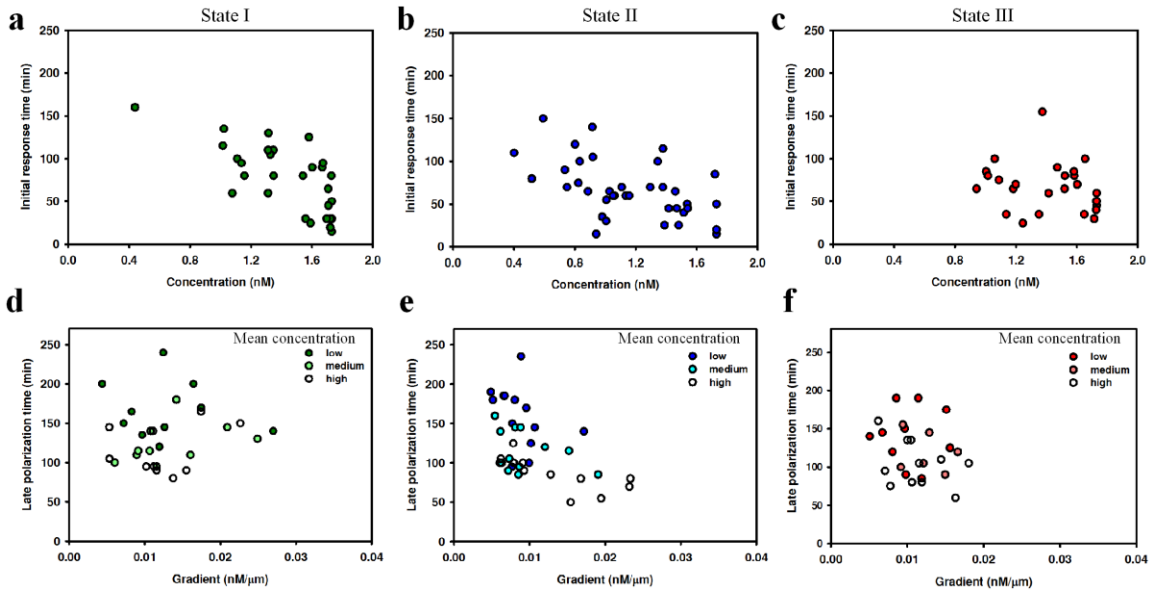

Fig. 3.10: Additional information on dependence of the initial response time and late polarization time on rapamycin gradient and local concentration values.

(**a-c**) The relationship between initial response time and mean rapamycin concentration for all states. Spearmann correlation coefficient values for each curve were determined as follows, state I: -0.582 (**a**), state II: -0.478 (**b**), state III: -0.377 (**c**). (**d-f**) Late polarization times determined for different gradient values for cells in all states. Pearson correlation coefficient values for each curve were determined as follows , state I: 0.103 (**d**), state II: -0.511 (**e**), state III: -0.228 (**f**). Within each plot, the data is binned into three mean concentration levels. State I (green) n = 27, state II (blue) n = 37, and state III (red) n = 29.

change was unexpected, but was consistent with the model prediction that crossing a threshold of Rac activity triggers a rapid, strong and stable polarization, akin to a phase transition. According to the model, a gradual variation of the Rac GEF level caused an abrupt transition from a moderately polarized to a highly polarized state, expressed mathematically as a bifurcation in the model response (**Fig. 3.12b**). We hypothesized that our use of low rapamycin concentrations allowed us to observe the effect of a gradual titration of intracellular Rac GEF and Rac activity levels leading to this strong

polarization. This gradual Rac GEF build-up was expected to follow the simple

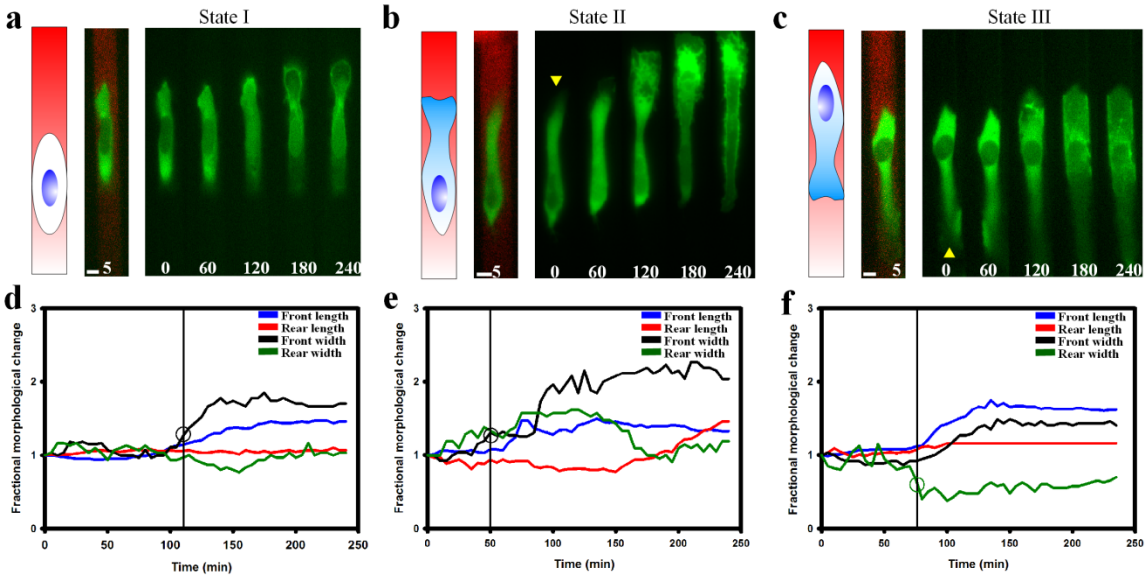

Fig. 3.11: State II cells undergo the initial response faster than cells in other states.

(**a-c**) Examples of the morphological changes in cells in different states experiencing the same gradient of rapamycin (0.01 nM/µm +/- 0.001). Cells were exposed to the gradient for the entire experimental period but only the 5 minute image showing both cells and the gradient visualization is shown for each state to add clarity. Yellow arrows indicate initial protrusions. Times are in minutes. Scale bars, 10 µm. (**d-f**) Quantification of the morphological changes seen in the examples shown in (**a-c**). The dropline indicates the initial response time. The circle indicates the metric used to determine it, with the color of the circle corresponding to the metric.

mathematical representation of accumulation of Rac GEF concentration over the duration t of exposure to rapamycin is

$$\Delta[\text{Rac GEF}] = k[\text{Rapamycin}]t, \qquad (1)$$

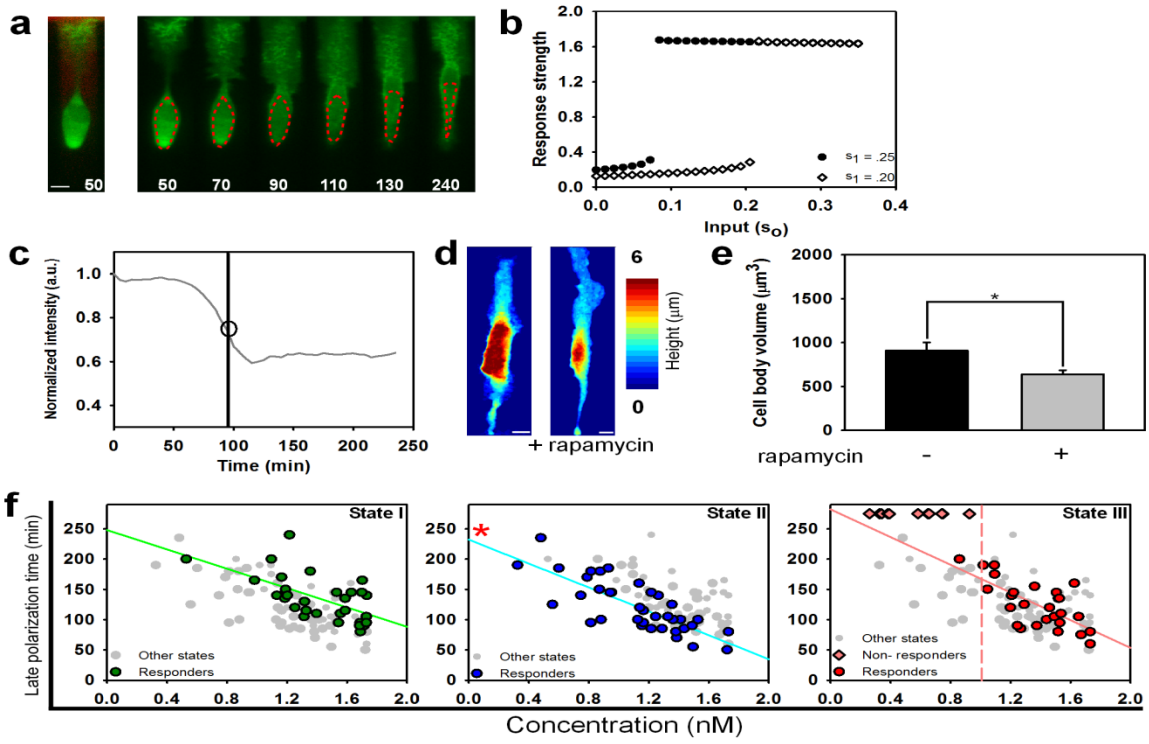

Fig. 3.12: Analysis of the late response time.

(**a**) Kymograph depicting the change in the lamellipodium directed by the gradient and dimming seen in the cell body during the late polarization time. The image preceding the kymograph illustrates the gradient (red), visualized with Alexa 594, received by the cell. The green color visualizes expression of YF-TIAM1. Red dotted lines indicate where the fluorescent values in **c** are taken from. Times are in minutes. Scale bar, 10 μm. (**b**) Simulations showing response strength vs. input (s_o) for two gradient levels (s_1); note bifurcations at distinct s_o values. Response strength is defined as the ratio of Rac activity at the front vs. the back in the model cell. (**c**) The intensity of the cell body normalized to the initial time point. Intensity values are taken as the mean of the fluorescence intensity of the area enclosed by the red trace in **a**. The drop line indicates the late polarization time, with a circle highlighting the inversion of response used to define this time. (**d**) 3D reconstruction of confocal slices of the same cell taken pre- and post- rapamycin addition. The "post-" cell image was taken 240 min after treatment. Scale bar, 10 μm. (**e**) Cell body volume before and after rapamycin addition. The data shows the mean of n = 9 cells and error bars show SEM. The asterisk denotes a statistically significant difference, p = 0.019, using a two sided student's t-test (**f**) The late response time as a function of mean concentration. State I (green) n = 29, state II (blue) n = 37, and state III (red) n = 27. The response times of other states are superimposed on each plot in grey. The pink drop line in the state III plot demarcates the separation point between unresponsive cells and responsive cells. Pearson correlation coefficient of linear regressions- State I = -0.608, State II = -0.783, State III = -0.698). The red asterisk denotes a statistically significant difference (state II vs. state I, p < 1e-4, state II vs. state III, p < 1e-4) between the y intercept of the linear regression for state II vs. the y intercepts of the regression data from other states. There is no significant difference between the y intercept of state I vs. state III (p = 0.13). Both statistical tests were carried out using an ANCOVA test.

where k is the constant defining tripartite rapamycin-FKBP-FRB complex formation. This expression allowed us to test the hypothesis of the existence of a Rac activity threshold mediating enhanced polarization.

One of the immediate consequences of the expansion of the lamellipodium in the direction of the rapamycin gradient was an apparent dimming of the YFP fluorescence signal from the cell body when observed with a wide-field epi-fluroescence microscope (**Fig. 3.12a,c**). The dimming of the fluorescence intensity was likely due to a redistribution of cytoplasmic volume from the cell body to the expanding lamellipodium and an increase in the translocation of YF-TIAM1 complexes to the membrane (**Fig. 3.12d-e**). We thus used the fluorescence intensity of the cell body as a metric for the timing of late polarization. Our analysis indicated that the late polarization time exhibited a linear dependency on the average local rapamycin concentration (**Fig. 3.12f**) (Pearson correlation coefficients; -0.608, -0.783, and -0.698 for state I, II, and III, respectively), in agreement with model predictions. MTLn3 cells also showed similar dependencies on mean rapamycin concentrations (**Fig. 3.9d-f**). A weaker dependence on the sharpness of the rapamycin gradient, consistent with the model, was also detected in these experiments (**Fig. 3.10d-f**) (Pearson correlation coefficients; 0.103, -0.511, and -0.228 for state I, II, and III, respectively). As with observations of early cell responses, state II cells reached the late polarization phase significantly faster than cells in other states for a given rapamycin concentration (**Fig. 3.12f** and **Fig. 3.13**) (ANCOVA test of y intercept, State II vs. State I, $p < 0.0001$, State II vs. State III, $p < 0.0001$) while the difference between the other two states was negligible (State I vs. State III, $p = 0.13$). We

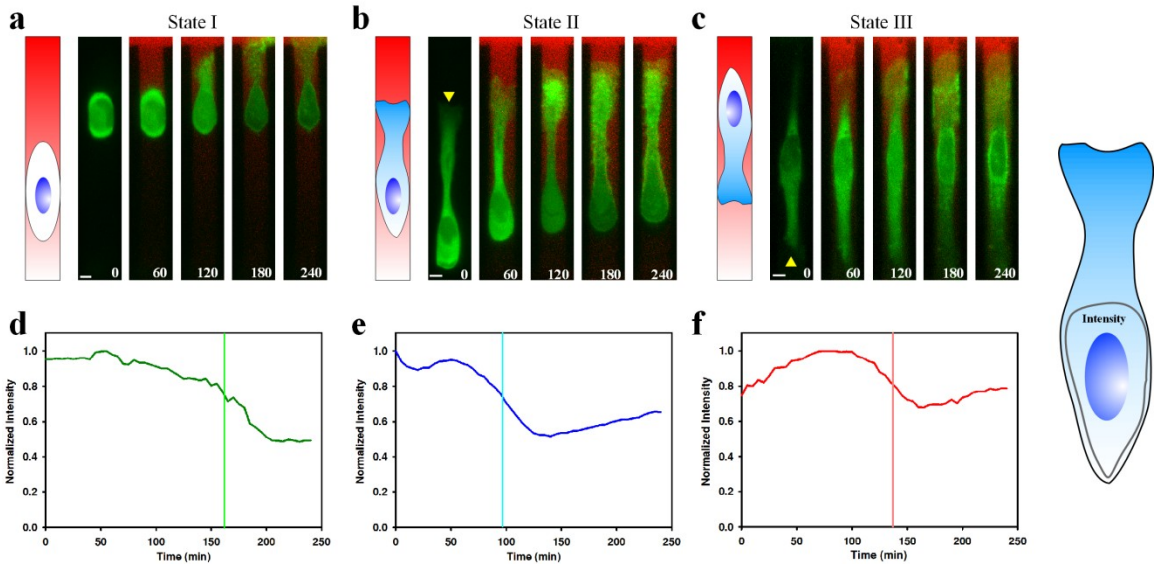

Fig. 3.13: State II cells undergo the late polarization response faster than cells in other states.

(**a-c**) The late polarization response of cells in all three states experiencing the same concentration gradient and the same local concentration of rapamycin. Yellow arrowheads indicate the direction of initial cell polarity. (**d-f**) Quantification of the average fluorescence intensity in cell bodies of the cells shown in (**a-c**) (see the schematic for the cell body definition). Drop lines indicate the late polarization times for each example. Note that the cell in state II reaches the late polarization phase faster than the cells in the other two states. Times are in minutes. Scale bars, 10 μm.

also found that a sub-population of state III cells exposed to lower concentrations of rapamycin completely failed to reach late polarization (**Fig. 3.12f**). In combination, these results suggested the existence of a threshold for late polarization, variable across individual cells and dependent on the initial polarity state.

3.2.5 Transient graded Rac activation

Equation (1) suggests that the duration of rapamycin exposure is as critical as the

local rapamycin concentration in exceeding the polarization threshold. Based on *in vitro* estimates of rapamycin-FKBP-FRB complex formation, the characteristic binding time estimated for 1 nM rapamycin is in the range of tens of minutes[162]. To test this prediction, we varied the time interval of rapamycin stimulation, taking into account the earliest polarization time observed for the rapamycin concentrations tested, i.e., 30 min and the estimated equilibration time above. We exposed cells to transient rapamycin gradients of 0.01 nM/μm for 30 min or 1 hr, followed by perfusion of the devices with rapamycin-free media for the rest of the experiment. We found no cells undergoing late polarization after a 30 minute rapamycin gradient exposure (Fig. **3.14a-c**), however, after a 1 hr stimulation, we found subsets of cells in all polarity states able to undergo late polarization, provided that they were exposed to sufficiently high concentrations of rapamycin (**Fig. 3.14d-f**). The polarization responses were morphologically similar to those seen earlier during continuous stimulation (**Fig 3.14d,e**), with the timing to late polarization indistinguishable from those observed for continuous stimulation (**Fig. 3.14f**). Responding cells continued to polarize even after the stimulus was withdrawn, suggesting fixation of the induced polarity and migration states (**Fig. 3.14d-e**), in contrast to their loss during the transition to spatially homogeneous Rac activation (**Fig. 3.6**).This behavior was in agreement with model predictions of a stable polarization beyond a Rac activity threshold which enables cells to maintain a strongly polarized state whose direction is based on but not continuously informed by the input gradient. Using a classification algorithm to separate responding and non-responding cells, we found that the minimum concentrations needed to elicit a response varied across the polarity states (**Fig. 3.14f**). In agreement with the earlier observation of distinct responses in state II

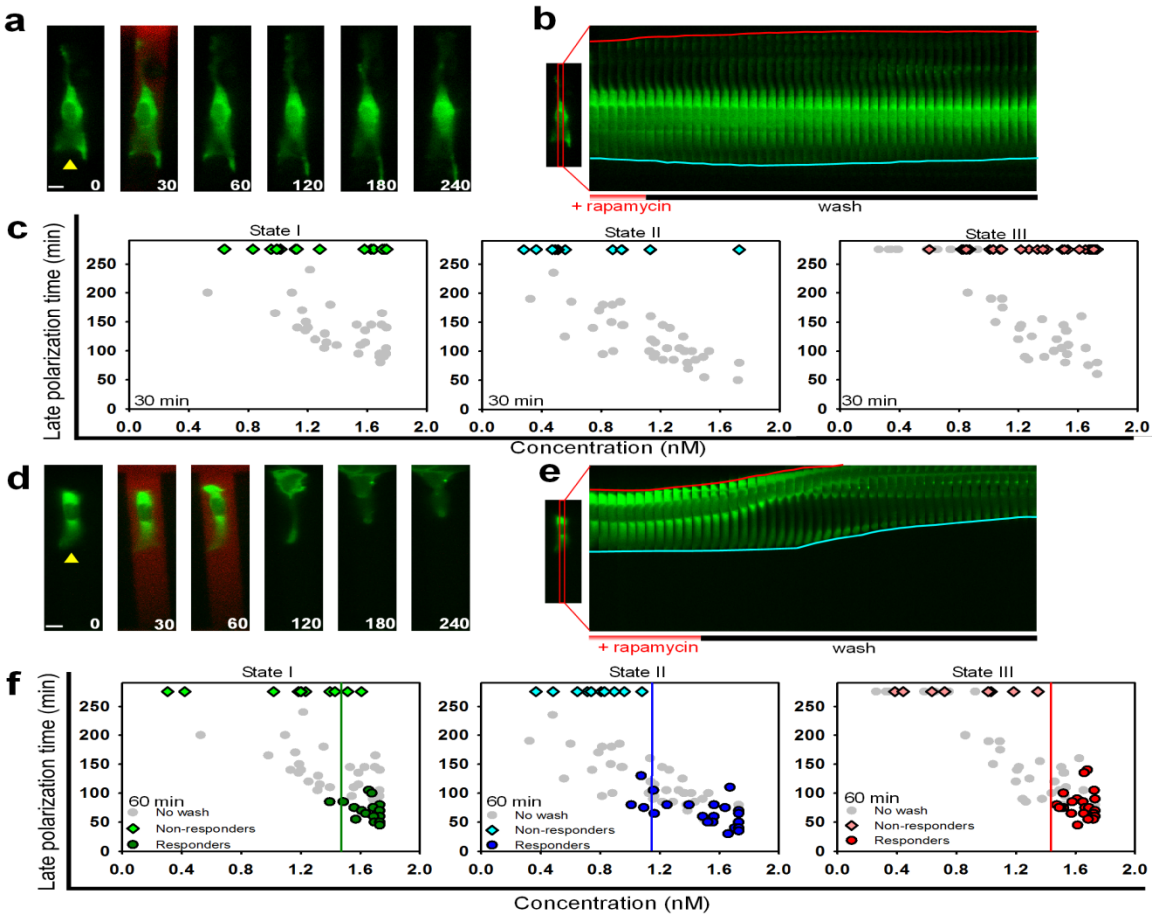

Fig. 3.14: Overcoming a Rac activity threshold determines the late polarization time.

(**a,d**) Time series of representative cells stimulated with a gradient of rapamycin for 30 minutes and 60 minutes respectively. Yellow arrows indicate the initial direction of cell polarity. Times are in minutes. Scale bars, 10 μm. (**b,e**) Kymographs taken from the center of cells (specified in accompanying image) illustrating morphological changes seen in **a**,**d** respectively. Blue lines track the initially polarized cell face while red lines track the opposite face. Below the kymograph is the experimental scheme used to stimulate the cell. (**c,f**) Late polarization time for a 30 minute and 60 minute stimulation period for all three states, respectively. For 30 minutes- State I (green) n = 17, state II (blue) n = 13, and state III (red) n = 31. For 60 minutes- State I (green) n = 32, state II (blue) n = 37, and state III (red) n = 32. Diamonds indicate cells that did not respond within the experimental time frame (240 minutes), while circles indicate responsive cells. Grey dots in each plot represent the late polarization times for cells in each state from Fig. 3f. The drop lines demarcate a threshold between responding and non-responding cells.

cells, cells in this state possessed the lowest response threshold (**Fig. 3.14f**) (State I= 1.5 nM, State II = 1.1 nM, State III = 1.4 nM). These data further support the existence of a

well-defined, initial polarity-dependent, Rac activation threshold essential for the rapid and profound induced changes in polarized cell morphology.

3.2.6 Inhibition of upstream activators

Direct activation of Rac allows bypassing of many signaling species commonly thought to be either upstream of Rac or involved in a regulatory feedback with this molecule. A well studied example of such a molecule is phosphatidylinositol 3,4,5-triphosphate (PIP_3)[145, 169, 170]. In chemoattractant gradients, phosphatidylinositol 3-kinase (PI3K), is recruited to the plasma membrane and phosphorylates the abundant phosphatidylinositol 4,5-bisphosphate (PIP_2) to yield PIP_3 (2, 43). Due to spatial regulation of PI3K recruitment, PIP_3 is often enriched at the front areas of migrating cells[78], displaying an intracellular gradient that is sharper than the gradient of the extracellular chemoattractant[142, 171]. It is thought that PI3K can influence cell guidance through its interaction with small GTPases and actin, but the mechanism of these interactions and the resultant role of PI3K in regulating chemotaxis are still under investigation[12, 13]. If, as sometimes assumed, PI3K is upstream of Rac activation in chemotactic signaling systems, its perturbations are not expected to lead to alteration of cell response to rapamycin-based Rac GEF stimulation. If, on the other hand, PI3K forms a feedback loop with Rac[143, 145, 150], or otherwise enables Rac-mediated outputs, cell responses might be affected by its inhibition, with the change in cell behavior potentially suggesting the mechanism of PI3K regulatory involvement. We used a pharmacological inhibitor of PI3K, LY294002, to inhibit PI3K activity during gradient stimulation with

rapamycin. As a control, we first observed the effects of LY294002 with and without rapamycin on basal cell motility and found no significant effects (**Fig. 3.2d,e**). After induction of the gradient, in contrast to the responses of cells in which PI3K was not perturbed, we observed large subsets of cells exhibiting no response, both in terms of the initial and late polarization, for all three initial polarity states across various gradients and concentrations (**Fig. 3.15a**, **Fig. 3.16**). Interestingly, the cells that did undergo the initial

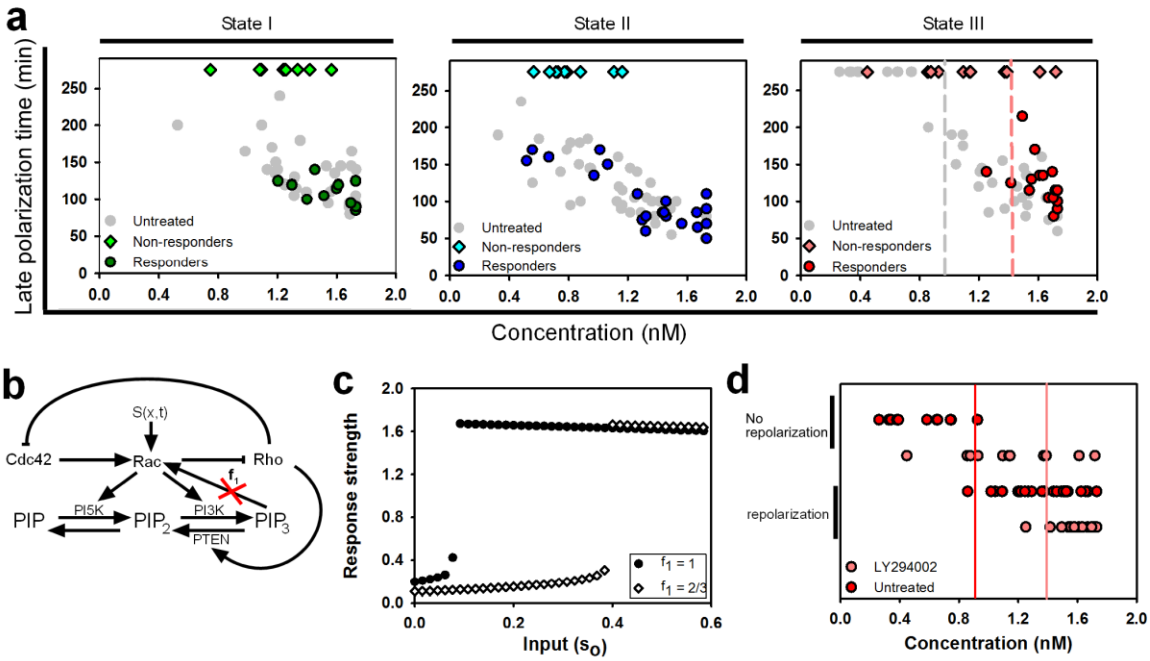

Fig. 3.15: PI3K modulates Rac mediated polarization.

(**a**) Late polarization time dependence against mean concentration with LY294002 treatment. State I (green) n = 21, state II (blue) n = 31, and state III (red) n = 27. Diamonds represent non-responder cells while circles represent responding cells. Grey dots on each plot illustrate the late polarization times seen in Fig. 3f. The grey drop line in the state III cell response plot represents the previous response threshold between non-responding and responding untreated cells, while the colored line represents the shifted threshold following LY294002 treatment. (**b**) Model schematic as in Model Figure 1 with red 'X' indicating that feedback from PIP_3 (f_1) is decreased during the subsequent simulations. (**c**) Simulations of response strength vs. signal strength for different feedback levels (In all previous simulations, $f_1 = 1$). (**d**) The response threshold for state III cells.

migration and late polarization responses did so with the same kinetics as observed in the absence of PI3K perturbation (**Fig. 3.15a**). This was consistent with the model prediction that a decrease in simulated strength of the PI3K-mediated feedback to Rac could lead to an increased threshold for cell responsiveness, requiring a sharper effective internal Rac activity gradient for cells to respond (**Fig. 3.15b-c**). As a consequence, the stochastic differences in internal states of the cells, defining cell sensitivity to the graded signaling input, can lead to a greater degree of cell population separation into responding and non-responding cells, without affecting the timing of responses in responding cells.

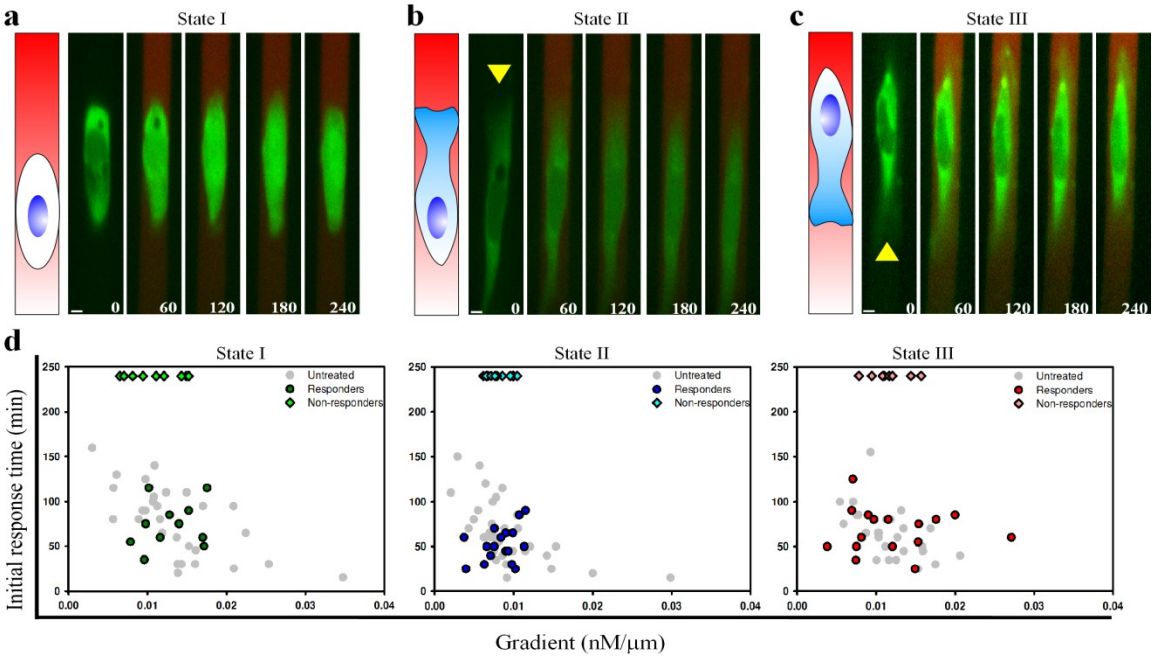

Fig. 3.16: Suppression of polarization responses with LY294002 treatment.

(**a-c**) Time lapse imaging of sample cells selected from subpopulations in different states during LY294002 addition. LY294002 was included at a concentration of 10 μM and was included in both cell medium solutions used to generate the rapamycin gradient. In all examples shown, cells fail to respond within the experimental time frame across all states. Yellow arrows indicate the direction of the initial cell polarity. Times are in minutes. Scale bars, 10 μm. (**d**) Initial response time vs. rapamycin gradient values in cells responding in the presence of LY294002. State I (green) n = 21, state II (blue) n = 31, and state III (red) n = 27. Diamonds represent non-responder cells while circles represent responding cells. Grey dots on each plot illustrate the initial response times seen for cells not exposed to LY294002 (**Fig. 3.7f**).

The results in **Fig. 3.12f** suggested the existence of a relatively high (re-)polarization threshold for state III cells. Thus we explored whether there would be synergy between this threshold and the increase in polarization threshold caused by inhibition of PI3K. We found that this threshold was indeed shifted in the presence of PI3K inhibition to a higher rapamycin concentration level (Fig. 5d) (1.0 nM for untreated state III vs. 1.4 nM for LY294002 treated state III). These results thus support the notion that PI3K can serve to sensitize cells to spatially graded Rac activation, allowing them to more readily exceed polarization and re-polarization thresholds.

3.3 Discussion

The results presented in this report argue that directly induced, spatially graded membrane translocation of a Rac activator, TIAM1, can trigger unambiguous polarization and directed movement of cells aligned with the direction of the stimulation gradient. TIAM1 is a specific Rac GEF[172] and another key regulator of polarity, CDC42, is considered upstream of Rac[62], therefore we attribute our observed phenotypes to be originating from direct Rac activation. The gradients of the inducer of Rac activation, the exogenously added rapamycin, can be effective with values as low as 15% across the cell length, with the rates of cellular responses to the stimulation being defined by the gradient steepness. The results suggest that even mild initial Rac GEF gradients can trigger strongly polarized cell responses, potentially providing insights into the levels at which graded inputs can be amplified in the signaling network. However, the response

kinetics can be enhanced with sharper input gradients (**Fig. 3.7f**) or if these gradients are amplified upstream of Rac activation.

We propose that rapamycin induced graded Rac activation can induce qualitatively similar polarization responses to those seen in chemoattractant gradients. For example, state I cells exhibit an initially low, mostly homogeneous Rac activity followed by the induction of high Rac activity at a newly formed front when a gradient of rapamycin is applied. This pattern of Rac activity is similar to that seen in neutrophils polarizing to a gradient of fMLP[173]. Additionally, state III cells repolarize when given sufficiently high gradients of rapamycin by forming a new front at the rear and retracting the previous front. This behavior is seen when chemoattractant gradients are presented at the rear of polarized cells through microfluidics or micropipette. Chemoattractant induced repolarization can be seen in neutrophils[174], social amoebae [175], and breast cancer cells[79]. Given that rapamycin induced graded Rac activation can mimic polarization behaviors seen with chemoattractant gradients, we believe that polarization can be defined at the level of Rac or at least starting from the level of Rac.

The research platform described here enabled the screening of the effects of a slow variation in the total cellular Rac activity. Both a simple model describing a feedback-based interplay between small GTPases in a cell and the corresponding experimental observations support the novel finding that a rapid and pronounced transition to a much stronger degree of polarization can occur if Rac activity exceeds a threshold level. This threshold was found to be strongly affected by the initial polarization status of the responding cell. Cells initially polarized in the direction of the applied gradient on average have lower response thresholds than cells that are

unpolarized or polarized in the opposite direction. Moreover, only a fraction of cells initially polarized away from the gradient responded to the gradient of Rac activator. These results are consistent with the following view supported by the model: an existing endogenous gradient of Rac activity in state II cells would lead to a smaller difference between the maximum local initial Rac activity within a cell and the polarization threshold value.

Our results further suggest that signal processing upstream of Rac activation in the context of chemoattractant stimulation may limit the degree of total Rac activation and thus the ability of the cell to reach the threshold controlling transition into the strongly polarized state. Thus, a single ligand may not induce such a transition. However, the threshold might potentially be reached and exceeded given multiple inputs converging on Rac activation, which may be affected by cell type-specific peculiarities of the signaling apparatus, such as basal levels of Rac activation and the expression of the signaling proteins.

The rapamycin stimulation system described here also allows a more detailed study of the interplay between Rac activation and activity of other signaling species, including those that might be involved in various feedback interactions. This analysis is akin to the more common epistasis assays, but with subtler phenotypes related more closely to gradient sensing responses. In particular, our analysis suggested that PI3K interplay with Rac activation, while consistent with the recently proposed formation of an AND gate in terms of the response[145] where both inputs are necessary to induce directed migration, acts more specifically by controlling the threshold of cell responsiveness to Rac activity gradients. Whereas PI3K inhibition does not prevent the ability of the cells

to undergo directed cell polarization or migration responses, it can strongly reduce the fraction of cells capable of these responses within the same set of experimental conditions.

The analysis here represents a more general framework extensible to other rapamycin-activatable signaling molecules[157, 176, 177], as well as other cell types and multicellular systems. Furthermore, the effects of gradients of other proteins engineered to be sensitive to small, membrane permeable molecules, such as ATP-analogues[178] and imidazole[179], could also be analyzed to refine our understanding of the mechanisms of cell responses to graded intracellular signaling activity. As also demonstrated in this report, such efforts could help develop qualitatively and quantitatively improved mathematical and computational models of gradient sensing and chemotaxis phenomena, extending common approaches to these processes. We suggest that, as the repertoire of methods for direct control of cellular events increases, microfluidics-based tools will play an important role in exploitation of these methods in cell navigation research.

3.4 Materials and Methods

3.4.1 Modeling

We have developed a simple model based primarily on the antagonistic relationship between the two small Rho family GTPases involved in polarized cell migration, Rac and Rho, modulated by Cdc42, based on sequential model selection. The model was implemented as a system of partial differential equations (PDEs) for Rho

GTPases in 1 space dimension and explored numerically using Matlab® (MathWorks). (See **3.4.14** for details).

3.4.2 Device fabrication

Microfluidic chips were created using a two layer soft lithography process[116]. PDMS (GE RTV) was used to create molds for the devices as described previously[180]. To increase the height of the flow through channels, the membrane between the control layer and flow layer was removed. Before an experiment, each device was treated with HCL, cleaned with 70% ethanol, and was allowed to bond to a clean 22x40 mm coverslip (Fisher).

3.4.3 Cell culture and transfection

HeLa cells were maintained in Dulbecco's modified Eagle's medium with 10% FBS and 1% Penicillin Streptomycin (Gibco). MTLn3 cells were cultured in Alpha minimum essential medium supplemented with 5% FBS and 1% Penicillin Streptomycin (Gibco). Both cell lines were kept in a 37°C and 5% CO_2 environment during culture and in experiment. MTLn3 cells were kindly provided by the Segall lab. The constructs, YF-TIAM1, YF, and Lyn_{11}-FRB were transfected into cells using Fugene HD (Roche) per manufacturer's recommendations. The Raichu-Rac FRET probe was kindly provided by the Matsuda lab and was transfected in a similar manner. During FRET experiments, MF-

TIAM1 was used in place of YF-TIAM1. MF-Tiam1 has a mCherry fluorophore in place of YFP and was used to avoid spectral overlap with the FRET probe.

3.4.4 Imaging

Microfluidic experimental imaging was performed using an inverted Zeiss Axiovert 200M epifluorescence microscope under 37°C and 5% CO_2, coupled to a Cascade II:1024 EMCCD camera (Photometrics) using a 40x, 1.3 numerical aperture oil immersion objective (Zeiss). The microscope was driven by Slidebook software (Intelligent Imaging Innovations). Images were taken every 5 minutes in the YFP channel using a 494 nm excitation filter and 530 emission filter set (Semrock) and Alexa 594 dye was imaged using a 572 nm excitation filter and 628 emission filter (Semrock) over a four hour period. A spectral 2D template autofocus algorithm was employed between images to account for any focus fluctuations. To correct for uneven illumination, all images were normalized with the following correction C = (I-D/F-D)*M where C = corrected image, I = initial image, D = darkfield image, F = flatfield image, and M = mean of difference between flatfield and darkfield images. The flatfield and darkfield images were taken as averages of multiple images. FRET images were taken using using a CFP excitation filter (Semrock), an appropriate dichroic (Semrock), and a YFP/CFP emission filters (Semrock).Volume analysis was performed on an inverted Zeiss Axiovert 200 spinning disk confocal microscope, coupled to a CCD camera (Hamamatsu) using a 40× objective (Zeiss). The microscope was driven by Metamorph 7.5 imaging software (Molecular Devices). YFP excitation was trigged with an argon laser (CVI-Melles Griot)

which was fiber-coupled (OZ optics) to the spinning disk confocal unit (CSU10; Yokogawa) mounted with a YFP dichroic mirror (Semrock) and an appropriate YFP filter (Chroma Technology).

3.4.5 Analysis of gradient and mean values of rapamycin

All analysis was performed using custom written codes in Matlab 2007b (Mathworks). Cell-based data (Cell length, centroid, etc.) was obtained from the YFP images while gradient based data was obtained from the Alexa 594 dye images. Cells were segmented from the YFP channel based on intensity. The signal to noise ratio was sufficiently high to preclude the use of more sophisticated segmentation techniques. Once cell boundaries were determined from the segmentation, concentration lines spanning the width of the channel were generated from the front and back of the cell to obtain local concentration data. The concentration lines were restricted to the width and length of an individual channel by manually selecting the boundaries of the channel from the Alexa 594 dye image. For any cell that extended out of the channel, the concentration lines were restricted to the respective ends of the channel to avoid spurious measurements associated with the height difference between the arms of the flow channels and the cross channels. Dye intensities were extrapolated to the intensities at the respective ends of the channel to determine concentration.

3.4.6 Cell tracking

Cell velocity was tracked by obtaining the coordinates of cell nuclei using a semi-automated script written in Matlab.

3.4.7 Quantification of the membrane distribution of YFP-FKBP

The translocation of YFP-FKBP to the membrane was quantified by taking the ratio of intensities at the cell periphery to the intensity in the cytoplasm. First, the cytoplasm and membrane were segmented by intensity thresholding from cell images and a subsequent morphological erosion was used to obtain each component separately. To obtain the membrane intensity across the cell length, the max value of each row of pixels in the membrane segmentation was taken. The cytoplasm intensity was obtained by taking the mean value of each row of pixels from the cytoplasm segmentation. Ratio values across the length of the cell were normalized between 0 and 1 and smoothed with a 10 point moving average. To aggregate data from multiple cells, time 0 was chosen as 30 minutes before visible translocation and subsequent profiles were normalized to values at time 0. For control cells, time 0 was chosen at times comparable to cells positioned in similar locations during rapamycin experiments.

3.4.8 FRET analysis

FRET analysis was done according to a previously described protocol[181]. Briefly, FRET images were analyzed by first subtracting background from each individual CFP and YFP FRET image (CFP excitation, YFP emission). Images were thresholded and

subsequently aligned with a dft registration algorithm[182]. The FRET ratio was calculated by dividing the YFP FRET image by the registered CFP image. Final images were Gaussian filtered to remove noise. To obtain the distribution of FRET activity across the cell length, the mean value of each row of pixels composing the ratio image was taken and final values were normalized between 0 and 1 for the cell length and smoothed with a 10 point moving average. To aggregate data from multiple cells, time 0 was chosen as 30 minutes before the appearance of morphological changes in accompanying MCHF-TIAM1 images. FRET profile data in later time points were normalized to time 0. For control cells, time 0 was chosen based on comparably located stimulated cells.

3.4.9 Volume analysis

Cell heights were generated by first taking calibrated Z slices of cells before and after rapamycin treatment. Afterwards, each slice was segmented and the summation of slices was used to generate the final image. The cell volume was determined by taking a region of interest (ROI) in the cell body from 3D reconstructions carried out using Matlab. The number of pixels in the ROI were then converted to □m based on pre-calibration of the slice height.

3.4.10 Measurement of the initial response time and late polarization time

All measurements were performed using Matlab. To determine the length of a cell's front and back, the cell nucleus was tracked by manually fitting an ellipse to the nucleus image and taking the centroid of the fitted ellipse as the position of the nucleus. Nuclei were clearly distinguishable in all YFP images analyzed due to exclusion of the construct. Cell front and back lengths were calculated by taking the coordinates of the front and rear of cells from segmented images and calculating the distance to the nucleus position (SI Appendix (Fig. S6)). To assay the width of the front and rear of each cell, the distance between the rightmost and leftmost coordinates of the cell front (top 10% of pixels) and rear (bottom 10% of pixels) were calculated (SI Appendix (Fig. S6)). The initial response time was taken as the time to reach 20% of the total magnitude of the first morphological change towards the gradient (SI Appendix (Fig. S9)). The initial response time was taken at the 50% level for MTLn3 cells due to the faster kinetics associated with their responses. To find the late polarization time, the decrease in fluorescence of the cell body was measured as a function of time. The fluorescence intensity was determined in ROIs, chosen automatically based on the end coordinates of the cell (front and back) (SI Appendix (Fig. S10)). The ROIs were then further eroded by several pixels to avoid any effects from the cell membrane. The late polarization time was taken as the time to reach 50% of the full fluorescence intensity drop in the ROI from the peak intensity value.

3.4.11 Population separation

Thresholds between non-responding cells and responding cells were determined using quadratic discriminant analysis ('classify' function) in Matlab. The two populations along with their corresponding concentrations were input into the function as training data and a separation point was generated from a given vector of concentrations.

3.4.12 Statistical analysis

Statistical analysis was carried out with Sigmaplot software (Systat) and Graphpad Prism (Graphpad). Experimental results were expressed as means with error bars equal to standard error of the mean (SEM). Comparisons between two groups were carried out with a two sided student t-test when assumptions of normality were fulfilled. For comparisons which did not satisfy the assumption of normality, a Mann-Whitney Rank Sum test was used. Comparisons were deemed to be significant if p values were < 0.05. The comparison between the y-axis intercepts of the linear regressions of the relevant data points was carried out using an analysis of covariance test (ANCOVA). First, the difference between slopes was compared; if the difference was insignificant, a comparison between the y-axis intercepts was performed. To compare fitted curves, an F-test was conducted, using the standard procedure.

3.4.13 Model methods

As described in our previous computational article[183], our model (shown in **Fig. 3.17**) is related to previous work[167, 184]. It was assembled in several stages, with

modifications and geometric considerations relevant to the specific experimental system described in the main text of this paper. Here, we provide a brief description of the ultimate model and how it was analyzed.

We consider the three GTPases implicated in polarized cell morphology, control, and chemotaxis, Cdc42, Rac and Rho (While in principle similar results are obtained without Cdc42, this master signaling component was included for completeness). For each GTPase, we track the levels of active and inactive forms bound to the membrane, G, G^{mi}, as well as an inactive (GDI- bound) cytosolic form G^c , (where $G = C, R, \rho$ represent Cdc42, Rac and Rho concentrations). Each variable is a function of time t and position x in a given cell. See below for details of the cell geometry. We assume that an inactive GTPase can (un)bind from the membrane, cycling between G^c and G^{mi} and that GEF/GAP activity interconverts the membrane bound species G^{mi}, G. We integrate over the depth direction (see below). Every point in the resulting domain is considered to have both cytosolic and membrane components. Crosstalk shown in the figure is directed at GEFs, with enhanced/reduced GEF activity depicted by arrows/inhibitory connections. Linear GAP activity is used in all cases. For phosphoinositides, we track PIP, PIP_2, and PIP_3 (whose levels are denoted P_1 , P_2 , P_3), Their interconversions, mediated by kinases and phosphatases) are assumed to be enhanced by Rac or Rho as indicated in the schematic (**Fig. 3.17**). The feedback from the PIP layer to the GTPase layer is governed by a tunable parameter f_1.

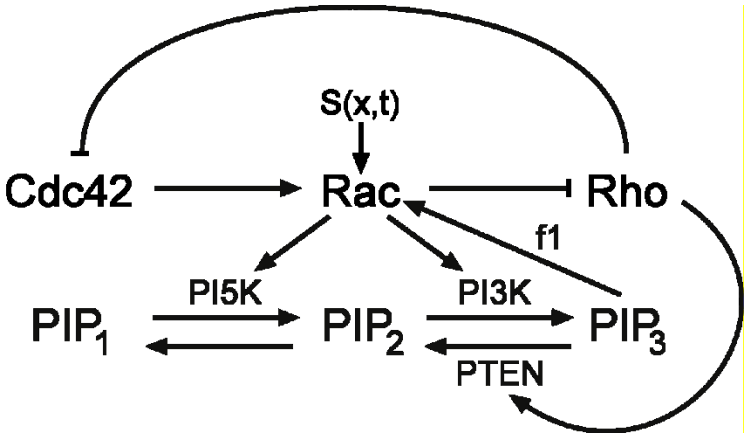

Fig. 3.17: Diagram of the Rho-GTPase/Phosphoinositide signaling network used in the one dimensional spatial cell model.

Activation is denoted by (→) and inhibition by (⊥). The signal is $S(x,t)=s_o + s_1 x / L$, where s_o and s_1 are the basal and gradient input components, and L is cell length.

inactive (cytosolic) GTPases are as follows, for a total of 9 partial differential equations (PDEs).

(1.1-1.3))

$$\frac{\partial G}{\partial t} = I_G - \delta_G G + D_m \Delta G,$$

$$\frac{\partial G^c}{\partial t} = k_{off} G^{mi} - k_{on} G^c + D_c \Delta G^c,$$

$$\frac{\partial G^{mi}}{\partial t} = -I_G + \delta_G G - k_{off} G^{mi} + k_{on} G^c + D_m \Delta G^{mi},$$

where *Dm*, *Dc* are membrane and cytosolic rates of diffusion, δ_G is GAP-mediated inactivation rate, k_{off} is the membrane disassociation rate constant, and k_{on} the membrane association rate constant. The term I_G is GEF-mediated rate of activation that depends on the availability of inactive GTPase, and on crosstalk from other active species. Rates of diffusion in membrane and cytosol are estimated as $D_m = 0.1$ μm/s^2 and $D_c = 100$ μm/s^2

as used previously[184, 185]. These equations, supplemented with no-flux boundary conditions conserve the total amount of each GTPase.

Geometry and simplification. Cells are narrowly confined in microfluidic channels, so that their width is constrained and time independent. In view of this fact, it is reasonable to approximate cell shape as a 3D box of length L, width w, and depth d satisfying $d < w << L$. Due to controlled signal and the physical constraints of the experimental apparatus, it is reasonable to neglect gradients in all but the length direction. Define a 1D projection of the variable G^c as

$$G^{pc}(x) = \int_0^w \int_0^d G^c(x, y, z) dz dy \approx dw G^c(x). \tag{1.4}$$

Here we have approximated G^c as nearly uniform across the width and depth directions. It follows directly that

$$\frac{\partial G^{pc}}{\partial t} = wdk_{off} G^{mi} - k_{on} G^{pc} + D_c \Delta G^{pc}. \tag{1.5}$$

Over the timescale considered, the volume of the cell $V \approx w \cdot d \cdot L$ is roughly constant. Channel diameter determines width w, so the observed lengthening of the cell must be accompanied by depth change. We take the initial values of $d_0 = 0.2$ μm, $L_0 = 20$ μm for a pre-stimulated cell. As L (but not d) is directly observable experimentally, we use $wd = V/L$ to eliminate the less easily measurable cell depth.

A composite inactive form. We consider the cycling of the inactive GTPase between membrane and cytosol to be in quasi steady state, as before[167]. We find the fraction of the

inactive forms on the membrane and in the cytosol to be be $\gamma(L) := k_{on} / (k_{on} + [V/L]\, k_{off})$ and

(1-$\gamma(L)$), respectively. A composite inactive form, G^i , is defined as

(1.6) $$G^i = G^{mi} + G^{pc}, G^{mi} = \gamma(L) G^i, G^{pc} = (1-\gamma(L)) G^i .$$

This accounts for the fact that only the membrane bound fraction of this composite is available for GEF activation. We also define an "effective diffusion constant"

(1.7) $$D_{mc}(L) = \gamma(L) D_m + (1-\gamma(L)) D_c .$$

This weights the diffusion constant of the composite form according to the proportion of time spent on the membrane and the cytosol. A full parameter set is determined by assuming $D_{mc}\,(L_0) = 50$, consistent with previous work(2-4) and $k_{on} = 1\text{s}^{-1}$. k_{off} is then determined by

(1.8) $$k_{off} = \frac{L_0 k_{on}}{V} \frac{(D_m - D_{mc}(L_0))}{(D_{mc}(L_0) - D_c)},$$

completing the parameter set associated with membrane cycling.

Reduced GTPase model. The system is now reduced to a set of three GTPases, each described by a single composite inactive form $G^i\,(x)$ and an active form $G(x)$, the total of which are conserved over the (1D) domain on the experimental timescale. We use the cross-talk depicted in **Fig. 3.17** to formulate a system of 6 PDEs. Linear inactivation by GAP's is assumed for each GTPase and up/down regulation of GEF activation pathways are assumed to take generic functional forms leading to

$$\begin{aligned}\frac{\partial G}{\partial t} &= I_G \frac{\gamma(L)}{\gamma(L_0)} \frac{G^i}{G_t} - \delta_G G + D_m \Delta G, \\ \frac{\partial G^i}{\partial t} &= -I_G \frac{\gamma(L)}{\gamma(L_0)} \frac{G^i}{G_t} + \delta_G G + D_{mc} \Delta G^i,\end{aligned} \tag{1.9}$$

with $G = C$, R, ρ and GEF activation rate functions

$$\begin{aligned}I_c &= \left(\frac{\hat{I}_c}{1 + (\rho / a_1)^n} \right) \frac{\gamma(L)}{\gamma(L_0)} \frac{C_i}{C_t}, \\ I_R &= \left(\hat{I}_R \left[1 + f_1 \frac{P_3}{P_{3b}} \right] + \alpha C + S(x,t) \right) \frac{\gamma(L)}{\gamma(L_0)} \frac{R_i}{R_t}, \\ I_\rho &= \left(\frac{\hat{I}_\rho}{1 + (R / a_2)^n} \right) \frac{\gamma(L)}{\gamma(L_0)} \frac{\rho_i}{\rho_t}.\end{aligned} \tag{1.10}$$

A more complete discussion of the forms of these kinetic terms was given earlier[184]. Note that $n \geq 2$ is required for this system to exhibit appropriate (``wave-pinning"[186]) polarization behavior. Normalization by $\gamma(L_0)$ makes for convenient parameterization. Here f_1 represents PI feedback strength to the GTPase module via Rac.

Phosphoinositide module. A PI feedback module[168], modified from earlier work[167] is based on the following equations:

$$\begin{aligned}\frac{\partial P_1}{\partial t} &= I_{p1} - \delta_{p1} P_1 + k_{21} P_2 - \frac{k_{PI5K}}{2} \left(1 + \frac{R}{R_t} \right) P_1 + D_P P_{1xx}, \\ \frac{\partial P_2}{\partial t} &= -k_{21} P_2 + \frac{k_{PI5K}}{2} \left(1 + \frac{R}{R_t} \right) P_1 - \frac{k_{PI3K}}{2} \left(1 + \frac{R}{R_t} \right) P_2 + \frac{k_{PTEN}}{2} \left(1 + \frac{\rho}{\rho_t} \right) P_3 + D_P P_{2xx}, \\ \frac{\partial P_3}{\partial t} &= \frac{k_{PI3K}}{2} \left(1 + \frac{R}{R_t} \right) P_2 - \frac{k_{PTEN}}{2} \left(1 + \frac{\rho}{\rho_t} \right) P_3 + D_P P_{3xx}.\end{aligned} \tag{1.11}$$

Terms in round braces are feedback from Rac and Rho. For parameter values see **Table 3.1**.

Parameter Name	Value	Definition
C_t, R_t, ρ_t	$2.4, 7.5, 3.1$	Total levels of Cdc42, Rac, and Rho
$\hat{I}_C, \hat{I}_R, \hat{I}_\rho$	$2.95, 0.2, 6.6$	Cdc42, Rac, and Rho activation rates
a_1, a_2	$1.25, 1.0$	Cdc42 and Rho half-max inhibition levels
n	3	Hill coefficient for inhibitory connections
α	0.65	Cdc42-dependent Rac activation
$\delta_C, \delta_R, \delta_\rho$	1.0	GAP decay rates of activated Rho-proteins
I_{P1}	10.5	PIP_1 input rate
δ_{P1}	0.21	PIP_1 decay rate
$k_{PI5K}, k_{PI3K}, k_{PTEN}$	$0.084, 0.00072, 0.432$	Baseline conversion rates
k_{21}	0.021	Baseline conversion rate
P_{3b}	0.15	Typical level of PIP_3
L_0	20	Cell Length
$D_m, D_{mc}(L_0), D_P$	$1.0, 50.0, 5.0$	Diffusion Rates

Table 3.1: Parameter set used for model simulations

Simulation Method. Simulations of the model equations (1.9), (1.10), (1.11) are performed with an implicit diffusion, explicit reaction scheme. Initial GTPase profiles are spatially uniform. The system is allowed to settle to a (parameter dependent) homogeneous steady state by integrating for 50 time units. At $t = 50$, the signal $S(x, t)$ is applied to Rac GEF as shown in Eqn (1.10) and the model is integrated to $t = 500$. We observe that a new polarized steady state emerges on a typical time scale of 100- 300 time units. In all simulations, the rest state was stable to small amplitude noise. The results of a sample simulation are shown in the kymograph of Figure 2a. GTPase asymmetry/polarization strength (**Figs. 3.12b** and **3.15c**) is measured as the absolute difference between the highest and lowest active Cdc42 (C) levels at the final time. (R or ρ can also be used to quantify polarization with similar results.) Response times, shown in **Fig. 3.7b**, are based on a generic inverse relationship between cytoskeletal

reorganization rate and GTPase polarization strength, i.e., response time = 1/response strength.

Predictions. Here we provide a brief overview of the model, referring the interested reader to our companion paper[183], where a detailed development and analysis has been provided.

The model described here, has at its core a polarization mechanism based on a wave of activity that sweeps across a cell and freezes to produce a static profile with large differences between cell poles. This stalling wave behavior has been termed "wave-pinning"(5). A key feature of this mechanism is that a threshold stimulus (either localized or distributed as gradient or noise) is needed to initiate a response. This feature stems from a combination of several factors: (a) active and inactive GTPases diffuse very differently due to their membrane (cytosol) residence. (b) The GTPase circuit shown in Model Fig. 1 contains an effective positive feedback. This causes the active GTPase to promote nearby activation. (c) Cycling between these forms preserves a constant total amount, leading to depletion effects as more and more activity is turned on. This ultimately freezes the wave in its tracks. Thus, if a stimulus provokes local activity exceeding a threshold, it self-amplifies and spreads, but only so long as inactive GTPase is available to be activated. It has been shown that this leads to a plateau of high (low) activity at the cell poles, but the details of the mathematical analysis are technical and beyond our scope.

In contrast to the above, many commonly used models for cell polarization (reviewed in [187]) have no threshold for patterning, and a response is triggered by arbitrarily small amplitude noise, here denoted by the informal term “ultrasensitive”. Such pattern formation is commonly termed Turing-type. Absence of a stable rest state, makes this type of polarization mechanism unsuitable for the HeLa cell system described in this article. Further discussion of various polarization models and their properties appears in [187].

To analyze the behavior of models with slow and fast rates of diffusion, we extended a recently developed technique termed "Local Perturbation Analysis" in [183]. This technique approximates the reaction-diffusion PDEs with simpler ordinary differential equations (ODEs) for the local (slow diffusing) and global (fast diffusing) components of the system. The analysis of the resulting LPA system of ODE’s allowed us to (a) find interesting parameter ranges and classify the dynamics as wave-type or Turing-type behavior, (b) easily explore how changes in model assumptions affect such behavior, and (c) understand how inhibition or upregulation influences the behavior of the system.

We used LPA to identify the wave-pinning parameter regime for the model. To investigate the experimentally modulated Rac GEF activity levels, we tested the model against manipulations of terms corresponding to Rac GEF activity levels. To do so, we defined a stimulus, $S(x,t)=s_o + s_1 x / L$, affecting the Rac GEF term I_R, with s_o the background level and s_1 the stimulus gradient steepness. (see expression for I_R in Eqs. (1.10) and S(x,t) in **Fig. 3.17**)

We ran several tests with various values of s_o and s_1 and studied how the model responds to increases in one of these parameters at various values of the other. We found that s_o modulates the wave pinning response threshold in the PDE model, (**Fig. 3.12b**). For fixed s_1, sufficiently large s_o provokes a response, as expected in the presence of a threshold. Further, the higher the background GEF activity level s_o, the lower the threshold to be breached for a response. Essentially, s_0 sets the response threshold, and s_1 produces spatial heterogeneity in the system. If s_1 is large enough that the solution breaches that threshold, a response similar to a phase transition results. The significance of this finding is that basal GEF activity levels, which can be modulated either internally by the cell or externally by the environment, aids in controlling the sensitivity of a cell to a directed stimulus.

3.4.14 Microfluidic setup

First, control valves (marked blue in **Fig. 3.2a**) were primed by connecting syringes filled with deionized water and pressurized to 20 psi. Experimental solutions were made using DMEM F-12 (Gibco) as a base medium. In a typical experiment, two solutions were injected into the device, one containing rapamycin and the other without. Rapamycin concentrations in microfluidic chips were titrated to uniform stimulation experiments in open chambers by comparing temporal responses. The rapamycin solution was injected into inlet "1" (Marked red in **Fig. 3.2a**). Once the solution reached the intersection of the channel and valve "1", the valve was pressurized to keep the solution

pinned at this location. In the corresponding '0' inlet, the rapamycin-free solution was injected and allowed to flush through inlets marked 'wash' to wash away any rapamycin which may have entered into the channel. After the wash period, plugs were placed into the "wash" inlets. For experiments utilizing LY294002, a 10 μM concentration of the drug was introduced into both experimental solutions. In all experiments, a 10 μg ml^{-1} fibronectin solution was injected into the 'cell' inlet prior to cell introduction. Actuation of valve marked "5" forced the fibronectin solution through the cross channels into the right flow through chamber and out of the outlet labeled 'out'. Fibronectin coating was performed for 50 min at 37°C. After the coating period, another rapamycin-free solution was placed into the outlet and the fibronectin solution was removed from the 'cell' inlet. A HeLa cell suspension, at a concentration of 1 x 10^6 cells ml^{-1}, was injected into the 'cell' inlet with a loading pipette. The outlet pressure was lowered below the atmospheric one, causing flow of the cell suspension and subsequent seeding of cells into the cross channels via the same principle used above for the fibronectin coating. Excess cells in the main flow arms were washed out. In experiments utilizing LY294002, a rapamycin and LY294002 free solution was injected into one of the 'wash" inlets to flush away excess cells to prevent prior exposure of cells to the inhibitor. HeLa cells were allowed to attach for 4 h at 37°C and 5% CO_2.

Chapter 4. Interplay between chemotaxis and contact inhibition of locomotion (CIL) during directed migration

4.1 Introduction

Directed cell migration is the ability of cells to bias their migration towards or away from external cues. It is fundamental to a diverse set of processes, including developmental patterning, cancer metastasis, immunity, and wound healing. During directed cell migration, several attractant or repulsive cues may act on a given cell simultaneously. These cues can arise from the environment or from the surface of similar or disparate cell types. For example, during topographic mapping, retinal growth cones can be directed by cell contact from a series of cell surface expressed ligands on other cell types along with soluble guidance molecules[188]. Alternatively, the directed collective migration of neural crest cells is driven by soluble guidance cues and cell repulsion between neural crest cells[189, 190]. However, it still remains poorly understood how the integration of multiple cues occurs and whether these cues act independently.

Another context in which multiple cues may play a prominent role in modulating directed cell migration is in the dissemination of cancer cells during metastasis. Chemotaxis, directed migration towards soluble chemoattractants, is an important cue in mediating cancer cell migration towards the vasculature[38]. The involvement of chemotaxis in metastasis is particularly well described for breast cancer, where intravital imaging has revealed that cells migrate along collagen fibers towards the vasculature in

response to gradients of epidermal growth factor (EGF)[164, 191, 192]. A second influential migration cue is contact inhibition of locomotion (CIL), discovered approximately 60 years ago by Abercrombie and Heaysman in fibroblasts[193]. This phenomenon is described as the suppression of locomotion upon cell to cell contact and a subsequent redirection of motility. Interestingly, many malignant cells lack CIL with other cell types (heterotypic) but retain CIL with each other (homotypic)[51, 52, 194, 195]. These tendencies have been suggested to increase the invasiveness of cancer by preferentially directing cancer cells away from the primary tumor and into the stromal environment[52, 189, 194, 195]. The molecular basis of this preferential CIL response has recently been explored in prostate cancer cells[52]. Although chemotaxis and CIL have been recognized individually as important regulators of directed cell migration during metastasis, the interactions between these cues are still poorly understood.

Here we investigate the interplay between CIL and chemotaxis through the use of MTLn3 rat breast adenocarcinoma cells overexpressing the epidermal growth factor receptor (EGFR), referred to as MTLn3-B1[196]. These cells are highly metastatic[196], exhibiting enhanced chemotaxis to EGF *in vitro* and *in vivo* and also display CIL[197], as cell collisions redirect cells away from their original migration trajectories. To investigate the relationship between chemotaxis and CIL, we developed a series of new microfluidic devices allowing a controlled, direct comparison of these cues at the single cell level. We explore the molecular mediators of these cues in MTLn3 cells and find that chemotaxis and CIL do not act independently of each other. Modulation of the strength of chemotaxis signaling can alter the directed migration outcomes when both cues are present. We

suggest that this interplay enhances overall directed migration and may be applicable to many other systems.

4.2 Results

4.2.1 Development of a microfluidic device to explore CIL and chemotaxis

We developed a new microfluidic device to study the combined effects of CIL and chemotaxis on the directed migration of MTLn3-B1 cells in a high throughput manner. The device consists of a continually replenished source and sink connected by a parallel array of microchannels[133, 141] (**Fig. 4.1a**, **Fig. 4.2a-c**). Gradients of EGF form across the microchannels via passive diffusion between the source and sink. To ensure that gradients of EGF develop across all microchannels simultaneously, thus allowing an equal comparison of cell response kinetics, we surrounded the microchannels with an intermediate rounded zone, accessible to built in elastomeric valves from above (**Fig. 4.2c**). Pressurizing the valves causes the rounded zones to collapse, effectively isolating the microchannels from the source and sink. In this manner, the source and sink can be pre-established at steady state around the microchannels without any transient stimulation, thus ensuring all microchannels receive the gradient coincidently when the valves are released (**Fig. 4.2b-c**). Gradients reach steady state in ~10 minutes and can be maintained for > 8 hours (**Fig. 4.2b**). We used device simulations to calculate the effect of including the rounded zone on gradient production and found that the effective

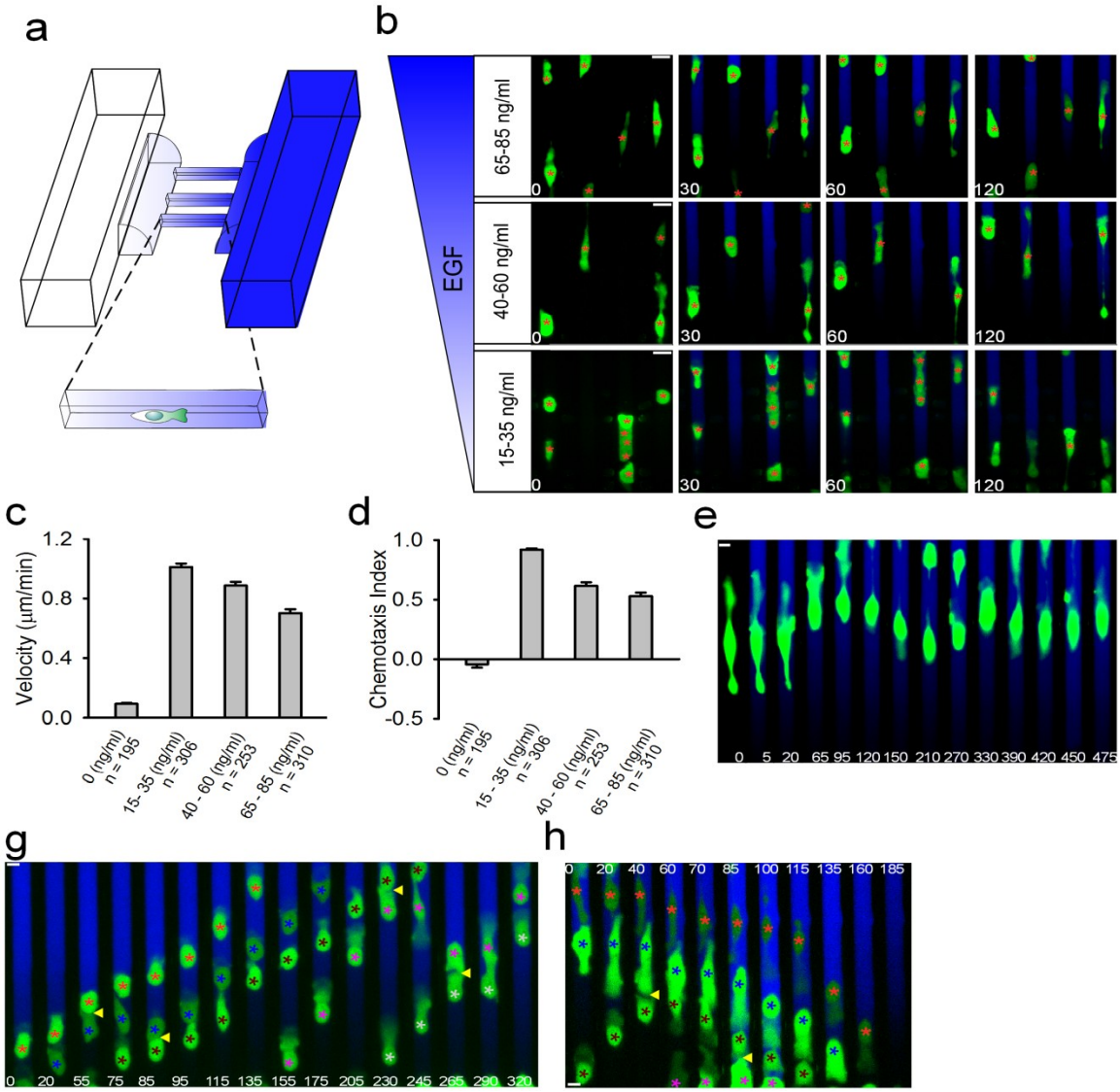

Fig. 4.1: MTln3-B1 chemotaxis in different EGF gradients and influences from CIL.

(**a**) Schematic of the microfluidic device used to produce defined gradients of EGF across microchannels housing MTLn3-B1 cells. (**b**) Representative images of MTLn3-B1 cells undergoing chemotaxis in different EGF gradients. Green color visualizes expression of GFP. The gradient is visualized with a Dextran dye here and in subsequent images. Red asterisks track cell positions from time = 0.Times are in minutes. Scale bars, 20 µm. (**c-d**) Quantification of velocity and chemotaxis index of MTLn3-B1 cells under control (0 ng/ml) and indicated EGF gradients from (**b**). Data is the mean from the number of indicated cells from n >= 3 independent experiments with error bars showing SEM. (**e**) An MTLn3-B1 cell displaying oscillations in migration in 65-85 ng/ml EGF gradients. (**g-h**) MTLn3-B1 cells undergoing CIL during chemotaxis. Colored asterisks track different cells. Yellow arrows highlight CIL events. Times are in minutes. Scale bars, 10 µm.

gradient across the microchannels was 30% on the low side and 70% on the high side, in relation to the source value (**Fig. 4.2d-e**). MTLn3-B1 cells within the microchannels

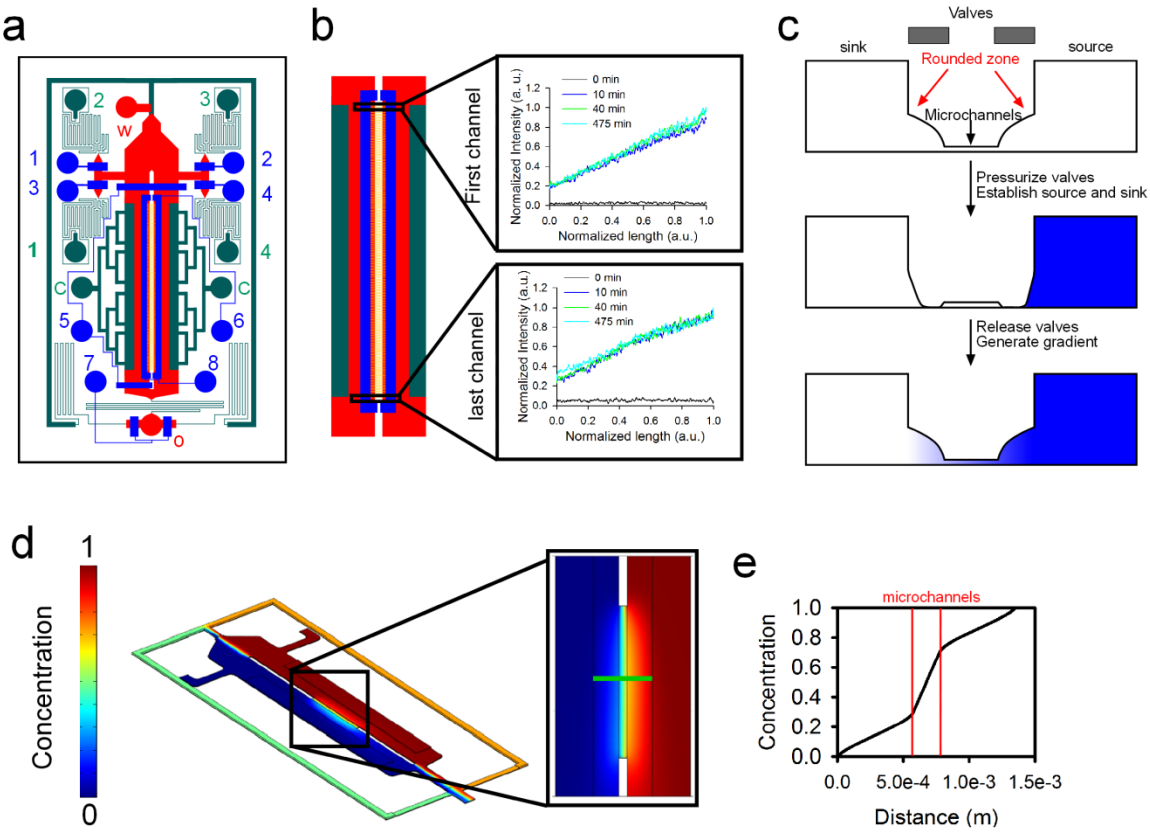

Fig. 4.2: Characterization of the microfluidic device used to study chemotaxis and CIL.

(**a**) Schematic of the microfluidic device. Different colors represent different functional layers. The green fluidic layer is 130 µm, the red rounded fluid layer is 30 µm, and the yellow microchannel layer is 6 µm. The blue layer is a valve layer (40 µm) that controls fluid flow in the underlying red layer. (**b**) Enlarged view of the functional gradient generation area and quantification of gradient formation kinetics in the first microchannelchannel and last microchannel channel. Gradient formation begins simultaneously across all channels, becomes stables in ~10 minutes, and is stable over the 8 hour experimental time period. (**c**) A side view illustrating the gradient formation strategy. (**d-e**) 3D computational fluid dynamics simulations of gradient generation in the microfluidic device. Quantification of the green line shown in the enlarged region is shown in (**e**). The concentration difference across the microchannels is 30-70%.

migrate in a single file, as the dimensions of the microchannels (14 µm by 6 µm, width by height) constrain cell migration to a single dimension. This fixation of one

dimensional motility serves three purposes: 1) it optimizes the opportunities for CIL to occur, 2) it provides an unambiguous readout of cell collision outcomes based on the resulting direction of cell migration, and 3) it matches the motility of MTLn3-B1 cells in MTLn3-B1 derived primary tumors *in vivo*, where individual cells migrate along collagen fibers in the tumor stroma[196].

4.2.2 Characterization of MTLn3-B1 chemotaxis

We first assessed how freely migrating MTLn3-B1 cells would respond to different gradients of EGF with a constant concentration difference (20 ng/ml) and varied mean concentrations (25 ng/ml, 50 ng/ml, and 75 ng/ml) (**Fig. 4.1b**). Upon introduction of EGF gradients, we observed the striking formation of large cell protrusions towards the source of EGF and rapid cell motility up the gradient (**Fig. 4.1b**). MTLn3-B1 cells displayed the highest velocity and greatest accuracy in 15-35 ng/ml EGF gradients, rarely changing directions and maintaining constant velocities (**Fig. 4.1c-d**). In contrast, MTLn3-B1 cells remained relatively stationary without a preferential direction in medium without EGF (**Figure. 4.1c-d**, **Fig. 4.3a**). Cell velocity and accuracy decreased with increasing mean concentration, but still retained a net preference up the gradient as compared to controls (**Fig. 4.1b-d**). In gradients with a high mean concentration of EGF (65- 85 ng/ml), many MTLn3-B1 cells displayed elongated cell morphologies and oscillatory migration patterns characterized by a frequent collapse of protrusions, suggesting a loss of directionality (**Fig. 4.1e**). Increases in gradient steepness (40 ng/ml

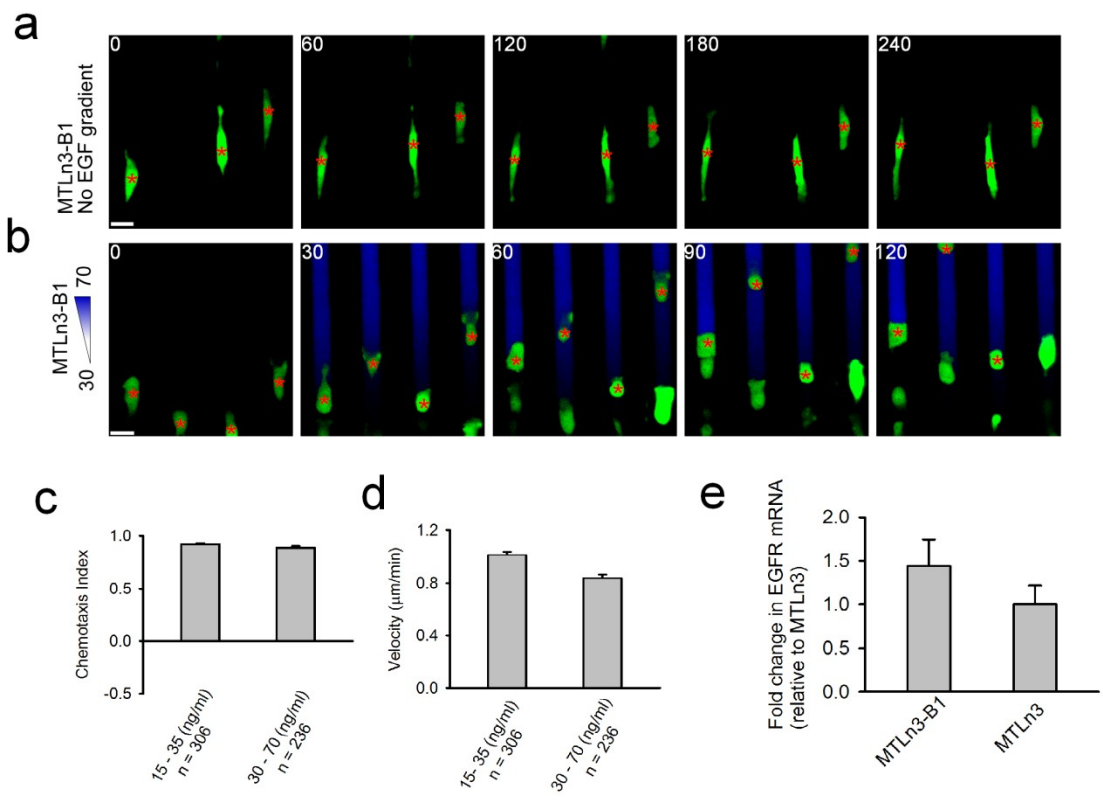

Fig. 4.3: MTLn3-B1 cells in control conditions and sharper EGF gradients.

(**a**) MTLn3-B1 cells in microchannels without EGF. (**b**) MTLn3-B1 cells in 30-70 ng/ml EGF gradients. In **a-b,** green color denotes GFP expression, the blue color visualizes the gradient of EGF using dextran dye as a proxy, and red asterisks track cell positions. Times are in minutes. Scale bars, 20 μm. (**c-d**) Quantification of the chemotaxis index (**c**) and velocity (**d**) of MTLn3-B1 cells in 30-70 ng/ml EGF gradients as compared to 15-35 ng/ml EGF gradients. 15-35 ng/ml EGFis reproduced from **Fig. 4.1d-e**. Data represents the mean from the number of cells indicated from n = 3 independent experiments with error bars showing SEM. (**e**) Relative expression of EGFR mRNA in MTLn3-B1 cells vs. MTLn3 cells. Data is the mean from n = 3 biological replicates and errors bars are S.D.

concentration difference across channels, 30-70 ng/ml EGF) did not enhance chemotactic behavior beyond the optimal gradient found above (15-35 ng/ml EGF) (**Fig. 4.3b-d**).

EGFR overexpression in MTLn3 cells has been previously associated with increased motility and chemotaxis *in vitro* and *in vivo,* along with enhanced metastatic potential[196]. Therefore, to validate our assay, we next investigated EGF chemotaxis in MTLn3 cells without EGFR overexpression (**Fig. 4.3e**, **Fig. 4.4**). MTLn3-B1 cells

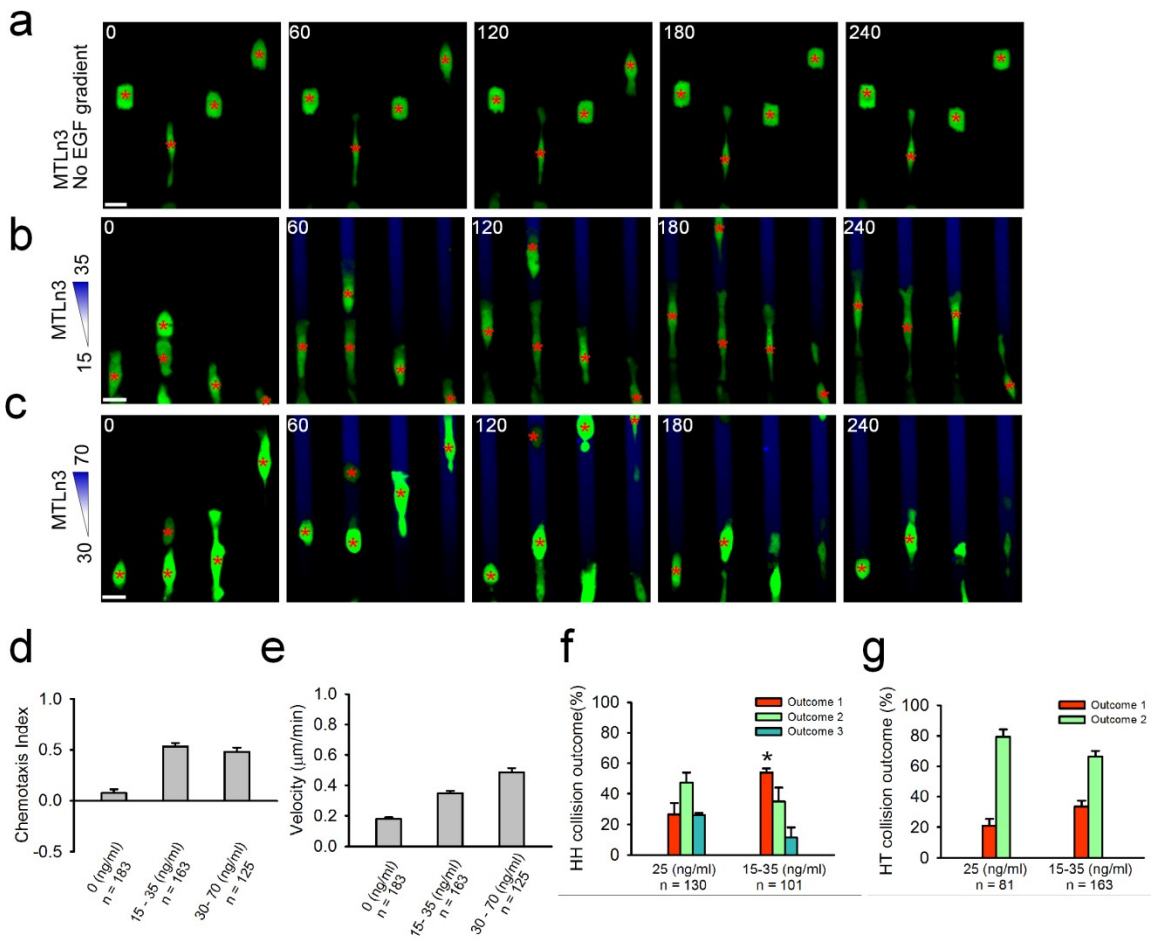

Fig. 4.4: Characterization of chemotaxis and CIL in MTLn3 cells.

(**a**) MTLn3 cells directionally migrating towards a 15-35 ng/ml gradient of EGF. (**b**) MTLn3 cells in microchannels without EGF. (**c**) MTLn3 cells chemotaxing to a 30-70 ng/ml EGF gradient. In **a-c,** green color denotes GFP expression, the blue color visualizes the gradient of EGF using dextran dye as a proxy, and red asterisks track cell positions. Times are in minutes. Scale bars, 20 μm. (**d-e**) Quantification of the chemotaxis index and velocity of MTLn3 cells in control and different EGF gradients. , data represents the mean from the number of cells indicated from n = 3 independent experiments with error bars showing SEM. (**f-g**) HH (**f**) and HT(**g**) collision outcomes in MTLn3 cells in uniform vs. a gradient of EGF at the indicated concentrations. Statistical comparisons are made between the same outcome in uniform vs. gradient. The asterisk denotes a statistically significant difference, p = .025, using a two sided student's t-test. In (h-i), number of total cells are indicated and data represents the mean from n =3 independent experiments with error bars indicating SEM. * = p < .05.

expressed approximately 1.5 fold more EGFR transcripts than MTLn3 cells (**Fig. 4.3e**). Similar to MTLn3-B1 cells, MTLn3 cells displayed little motility and had unbiased

migration in the absence of EGF (**Fig. 4.4a**). MTLn3 cells exhibited chemotaxis in 15-35 ng/ml gradients of EGF, but had decreased velocities and accuracies as compared to MTLn3-B1 cells (**Fig. 4.1c-d**, **Fig. 4.4b,d-e**), in agreement with previous results[196]. In sharper EGF gradients (40 ng/ml concentration difference), MTLn3 cell accuracy did not improve but cell velocity increased (**Fig. 4.4c-e**). Taken together, our results indicate that our device can efficiently assay chemotaxis in MTLn3 cells and can distinguish between MTLn3 cells with different metastatic potential.

4.2.3 CIL alters chemotactic responses

Next, we focused on how CIL might affect the directional migration of MTLn3-B1 cells during chemotaxis to chemical gradients of EGF. We found that CIL could dramatically influence chemotactic behavior by redirecting MTLn3-B1 cells either towards or away from the chemical gradient. This was especially prominent in groups of cells in single channels migrating at different velocities. For example, often times a "ping pong" pattern would emerge where a trailing cell would catch up to a leading cell and be redirected away, but would be subsequently reoriented back up the gradient by a second chemotaxing cell (**Fig. 4.1g**). Conversely, in some cases, CIL could abrogate chemotaxis. This is illustrated in **Fig. 4.1h**, where a cell is redirected back down the gradient and subsequently redirects another entering cell down the gradient, leading to the entire cell group moving away from the gradient (**Fig. 4.1h**). The phenotypes at the interface

between CIL and chemotaxis interactions (**Fig. 4.1g-h**) bring up several questions. Can one directed migration cue supersede the other? If so, under what circumstances does this occur? Are CIL and chemotaxis independent from each other? To answer these questions, we first sought to characterize the typical results of CIL without chemical gradients and to see how these results might shift in the presence of gradients.

4.2.4 CIL in uniform concentrations of EGF

To decouple CIL from EGF chemotaxis, we stimulated MTLn3-B1 cells within microchannels with different uniform concentrations of EGF (25 ng/ml, 50 ng/ml, 75 ng/ml), matching the mean concentrations of the previously imposed gradients. MTLn3-B1 cells in the presence of uniform EGF displayed rapid changes in direction and frequent CIL events (**Fig. 4.5a**). Cell to cell collisions could be categorized into two main groups (**Fig. 4.5b**), head to head collisions and head to tail collisions. In head to head (HH) collisions, two cells migrate towards each other, leading to the collapse of both protrusions upon contact (**Fig. 4.5c**). This collapse is subsequently followed by three different outcomes (**Fig. 4.5c**), both cells either migrate upwards (Outcome 1), in opposite directions (Outcome 2), or downwards (Outcome 3). In head to tail (HT) collisions (**Fig. 4.5d**), one cell (trailing) catches up to another cell (leading) migrating in the same direction. Upon contact with the rear of the leading cell, two outcomes occur; the trailing cell either continues in the same direction (Outcome 1) or is repelled and migrates in the opposite direction (Outcome 2). In all cases, the leading cell remained unaffected by the cell collision, suggesting that cell contact specifically suppresses cell

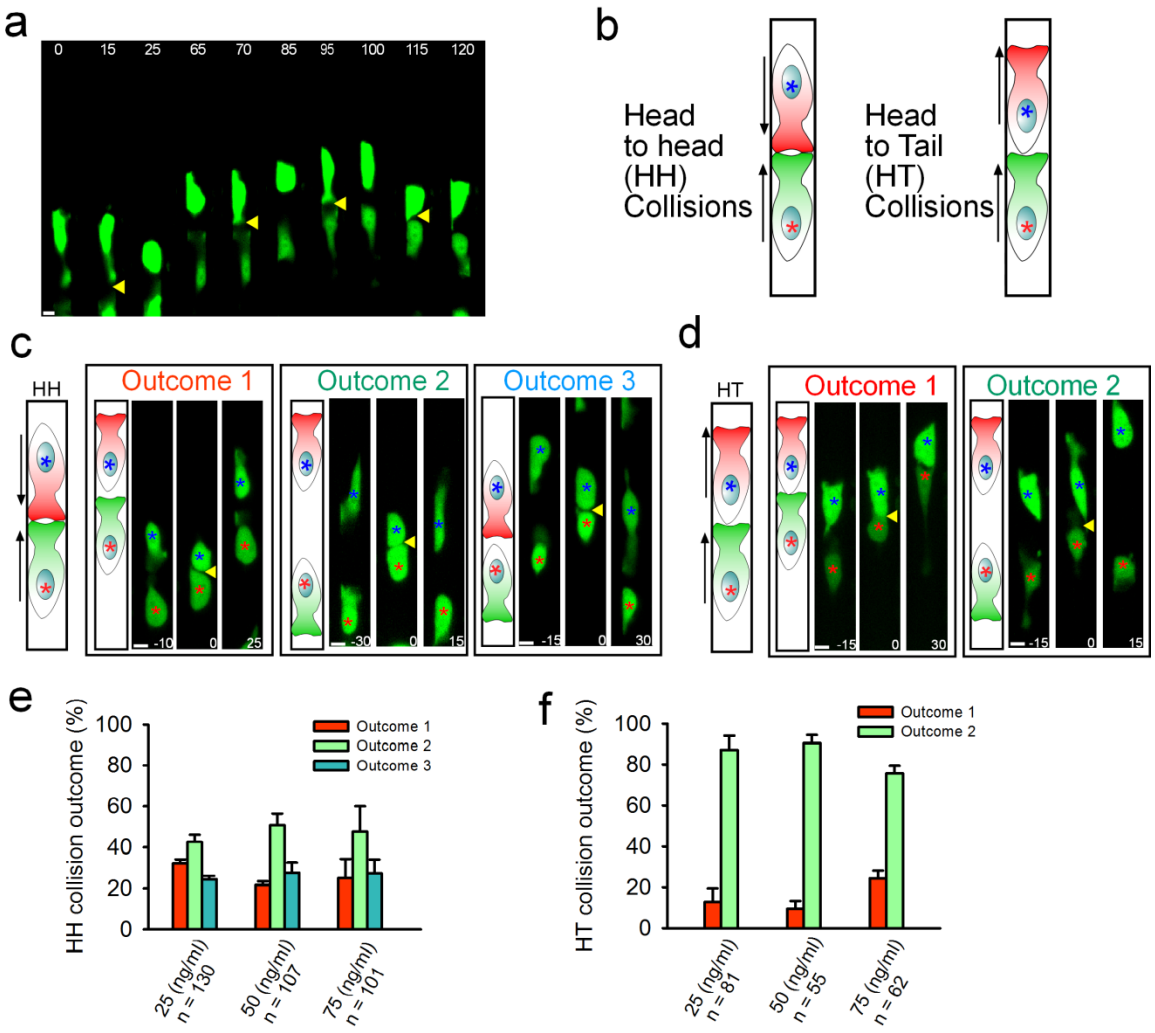

Fig. 4.5: Characterizaton of CIL in uniform concentrations of EGF

(**a**) MTLn3-B1 cells displaying random motility and undergoing multiple CIL events in a uniform concentration of EGF (50 ng/ml). (**b**) Schematic of the two categories of cell collisions leading to CIL. (**c-d**) Examples of the outcomes of head to head and head to tail collisions in MTLn3-B1 cells with corresponding illustrations. Collisions occur at time t = 0. The blue asterisk tracks the top cell, while the red asterisk tracks the bottom cell. Yellow arrows indicate collisions. Times are in minutes. Scale bars, 10 μm. (**e-f**) Probability of head to head and head to tail collision outcomes in the indicated uniform concentrations of EGF. The total number of cells are indicated per condition. Data represesents the mean from n =3 independent experiments per condition and error bars show SEM.

protrusions. We found that regardless of the concentration of EGF, HH collisions typically lead to the repulsion of both cells in opposite directions (Outcome 2),

suggesting a dose independent effect (**Fig. 4.5e**). Similarly, HT collisions primarily resulted in the repulsion of the follower cell (Outcome 2) in an EGF dose independent manner (**Fig. 4.5f**). MTLn3 cells also displayed similar propensities (**Fig. 4.4f-g**).

As CIL is traditionally studied in 2D formats, we also investigated whether MTLn3-B1 cells display CIL in 2D environments in various doses of EGF using a second microfluidic device with traditional CIL metrics (**Fig. 4.6**). MTLn3-B1 cells exhibited CIL in 2D regardless of the dose of EGF (**Fig. 4.6e**), in agreement with our results above (**Fig. 4.5e-f**). We also observed that cell collisions selectively affected protrusions (**Fig. 4.6d**). Our results suggest that CIL functions independent of the levels of uniform EGF signaling in 2D and 1D and specifically affects cell protrusions. To summarize, in uniform doses of EGF, HH collisions tend to result in the repulsion of both cells in opposite directions, while HT collisions repulse the follower cell.

4.2.5 Chemotaxis biases CIL outcomes

Having characterized the outcomes of CIL in uniform doses of EGF, we next revisited how CIL outcomes were influenced by the presence of various gradients of EGF (**Fig. 4.7a-c**). Upon closer inspection, we found several HH collisions where the accurately migrating cell (bottom cell) did not lose its protrusion upon contact, as opposed to the inaccurately migrating cell, whose protrusion collapsed and reformed up the gradient (**Fig. 4.7d**). This result suggests that chemical gradients do not simply polarize cells after their protrusions collapse after contact. In 15-35 ng/ml EGF gradients, the optimal MTLn3-B1 chemotactic gradient found earlier (**Fig. 4.1b-d**), we found a

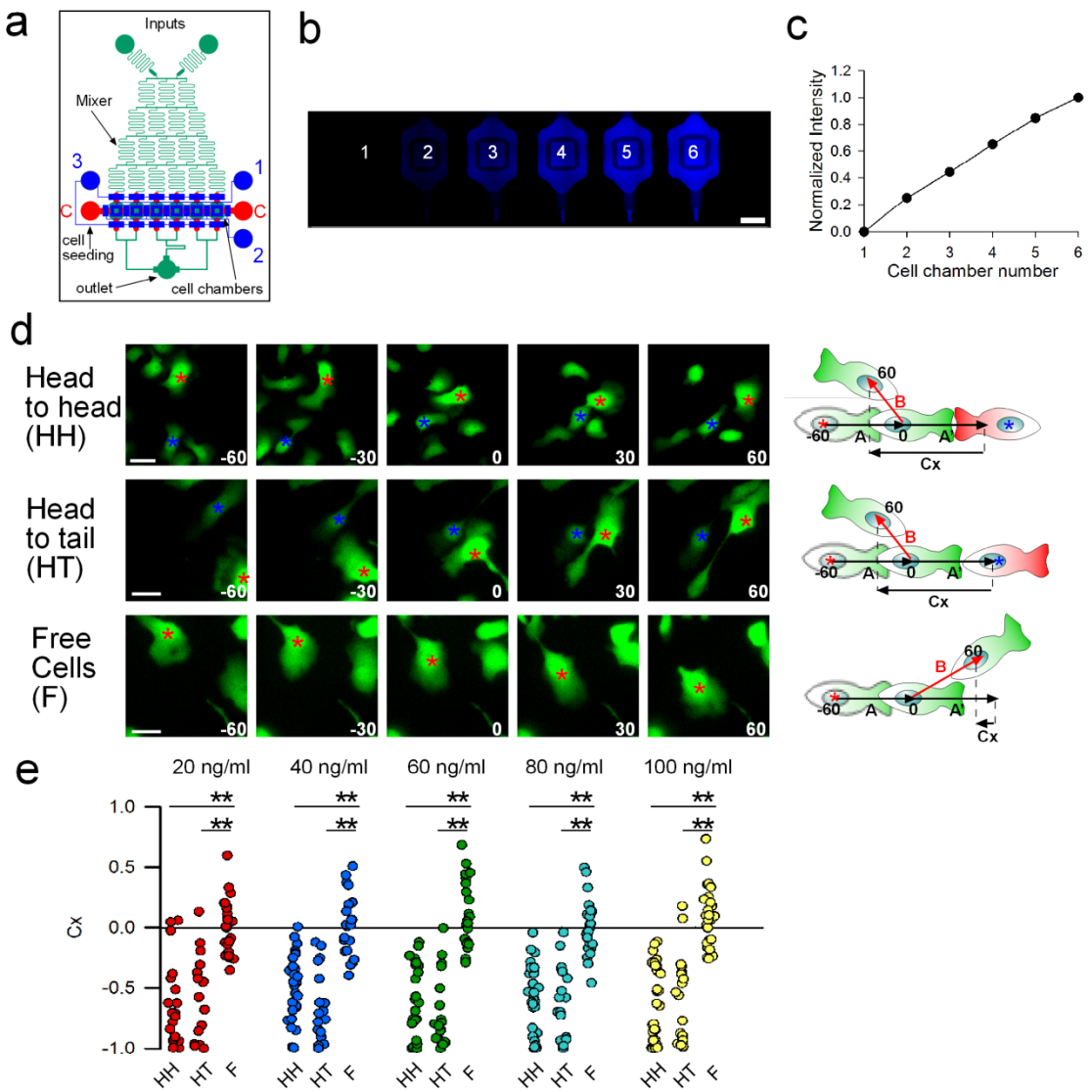

Fig. 4.6: CIL occurs in an EGF dose independent manner in 2D.

(**a**) The schematic of the microfluidic device used to produce multiple doses of EGF in a single experiment. The green gradient generation and cell chamber layer is 100 μm and the red rounded fluid layer is 30 μm. The blue layer (40 μm) is a control valve layer modulating flow in the red layer. (**b**) Sample image of different doses of EGF produced in the numbered cell chambers visualized with a dextran dye. (**c**) Quantification of mean fluorescence intensity in the labeled cell chambers in (**b**), showing the different doses produced. (**d**) MTLn3-B1 cells undergoing head to head (HH) (top panel) or head to tail (HT) (middle panel) collisions as opposed to free movement (**F**) (bottom panel). Corresponding metrics used to analyze them are shown on the side. The vector, Cx, represents the change in acceleration due to either a collision or random migration. Cx is normalized to account for differences in velocity. Green color indicates GFP expression. Colored asterisks track individual cells. Times are in minutes. Scale bars, 20 μm. (e) Quantification of Cx in HH and HT collisions vs. free moving cells (F) in different doses of EGF. . n > = 15 cells from 3 independent experiments per condition. ** = p <1e-3 from a student's t-test.

significant shift in HH collisions towards outcome 1 (migration of both cells up the gradient) as compared to a uniform 25ng/ml EGF dose (**Fig. 4.7e**), clearly suggesting that

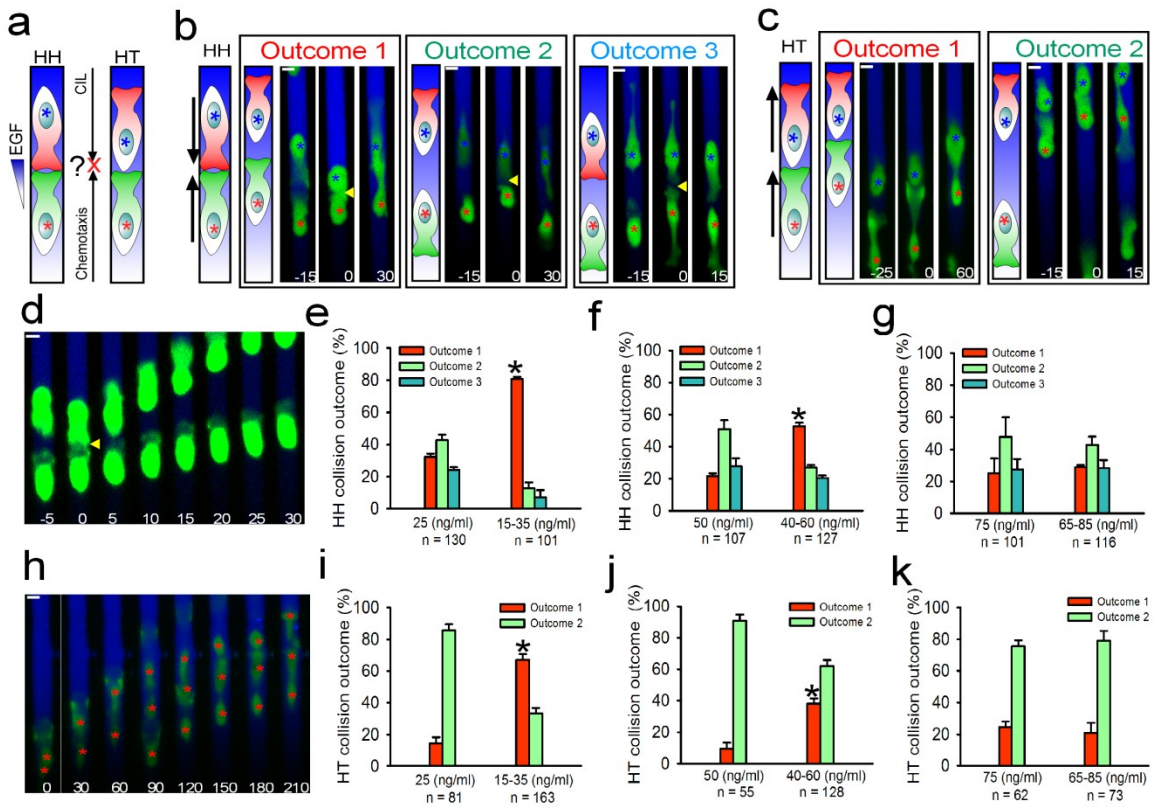

Fig. 4.7: Chemotaxis biases CIL towards gradients

(a) Schematic of how chemotaxis and CIL cues conflict during different cell collisions. **(b-c**) Examples of the outcomes of head to head (**b)** and head to tail (**c**) collisions in MTLn3-B1 cells in gradients of EGF with corresponding illustrations. Collisions occur at time t = 0. Green color indicates expression of GFP. The gradient of EGF is visualized with Dextran dye here and in all subsequent images. Colored asterisks track different cells. Yellow arrows indicate collisions. (**d**) A head to head collision between MTLn3-B1 cells where the bottom cell maintains its protrusion. Yelllow arrow indicates the collision. (**e-g**) Probabilities of head to head collision outcomes in gradients of EGF vs. uniform concentrations. Uniform concentrations are taken from **Fig 4.5e**. Number of collisions analyzed is indicated. Data shown is the mean of n = 3 independent experiments with error bars representing SEM. Statistical comparisons are made between the same outcome in uniform vs. gradient using a student's t-test. (**h**) A group of MTLn3-B1 cells streaming up a gradient of EGF. Red asterisks track cell positions. (**i-k**) Probabilities of head to tail collision outcomes in gradients of EGF vs. uniform concentrations. Uniform concentrations are taken from **Fig. 4.5f**. Total colllisions analyzed per condition are displayed. Data is the mean of n = 3 independent experiments per condition. Error bars are SEM. Statistical comparisons are made between the same outcome in uniform vs. gradient using a student's t-test. Times are in minutes. Scale bars, 10 μm. * = p < 1e-3.

chemotaxis can influence CIL behavior. This shift was diminished but still significant in 40-60 ng/ml EGF gradients as compared to a uniform 50 ng/ml EGF dose (Fig. **4.7f**), but was completely lost in the 65-85 ng/ml EGF gradient (**Fig. 4.7f**), where the collision outcomes mirrored those of the uniform 75 ng/ml EGF dose (**Fig. 4.7f**). HH collisions in MTLn3 cells chemotaxing in 15-35 ng/ml EGF gradients also became biased towards outcome 1 (**Fig. 4.6f**), albeit with a smaller shift than MTLn3-B1 cells (**Fig. 4.7e**), suggesting that EGFR overexpression increases the influence of chemotaxis over CIL. Overall, our results suggest that modulating the strength of chemotactic behavior, either by altering external gradient inputs or changing receptor expression, can dynamically alter the balance between chemotaxis and CIL cues.

Next, we tracked the outcomes of MTLn3-B1 HT collisions in gradients of EGF (**Fig. 4.7b**). We found many MTLn3-B1 cells streaming together in close apposition (**Fig. 4.7h**), as has been observed in MTLn3 derived tumors *in vivo*[196]. This suggested that HT collision induced CIL may be reduced in optimal EGF gradients. In 15-35 ng/ml EGF gradients, we indeed found a significant shift in HT collisions towards outcome 1 (Trailing cell maintains its protrusion and continues migrating up the gradient) as compared to the 25 ng/ml uniform EGF control (**Fig. 4.7i**), providing further evidence that chemotaxis influences CIL. As seen in HH collisions, we saw a similar but diminished shift in 40-60 ng/ml EGF gradients as compared to the 50 ng/ml uniform EGF controls (**Fig. 4.7j**), and total loss of the shift in 65-85 ng/ml EGF gradients, where the outcomes effectively mimicked those of the 75 ng/ml uniform EGF control (**Fig. 4.7k**). The outcomes of HT collisions in MTLn3 cells migrating in 15-35 ng/ml EGF gradients were slightly shifted from uniform 25 ng/ml EGF controls (**Fig. 4.6g**).

Thus far we have shown that chemotaxis and CIL are both cues which can substantially influence directed migration in MTLn3 cells. Furthermore, we have shown that they are not independent from each other when both are present, suggesting that the chemotaxis and CIL signaling pathways dynamically regulate each other. The molecular components which mediate CIL and chemotaxis in MTLn3 cells are still poorly understood. It is also unknown where crosstalk might occur between these two pathways. Therefore we next set out to identify molecular components of the chemotaxis and CIL pathways in MTLn3 cells.

4.2.6 PI3K and Rac activity during chemotaxis and CIL

First, we investigated molecules activated during MTLn3-B1 chemotaxis. Phosphatidylinositol 3-kinase (PI3K) and Rac are well known regulators of directed migration and have been shown to be at active the leading edge of several chemotaxing cells, such as dictyostelium[78, 198], neutrophils[57, 173], and fibroblasts[35, 199]. Their roles in EGF stimulated protrusion formation have been investigated in MTLn3 cells[200, 201], but their localization and activity in living MTLn3 cells during chemotaxis are unknown. Therefore, we transfected MTLn3-B1 cells with PI3K and Rac biosensors and observed their responses during EGF chemotaxis in our microfluidic device. To observe PI3K activity, we used the ph domain of Akt (Akt-ph) tagged with a mCherry fluorophore (mCH-Akt-ph) (**Fig. 4.8a**) and took its ratio to a cytosolic GFP to remove volume effects, as has been done previously[150]. PI3k activity in MTLn3-B1 cells became locally enriched at the cell front in EGF gradients (**Fig. 4.8a**), with a peak of activity at 6 minutes

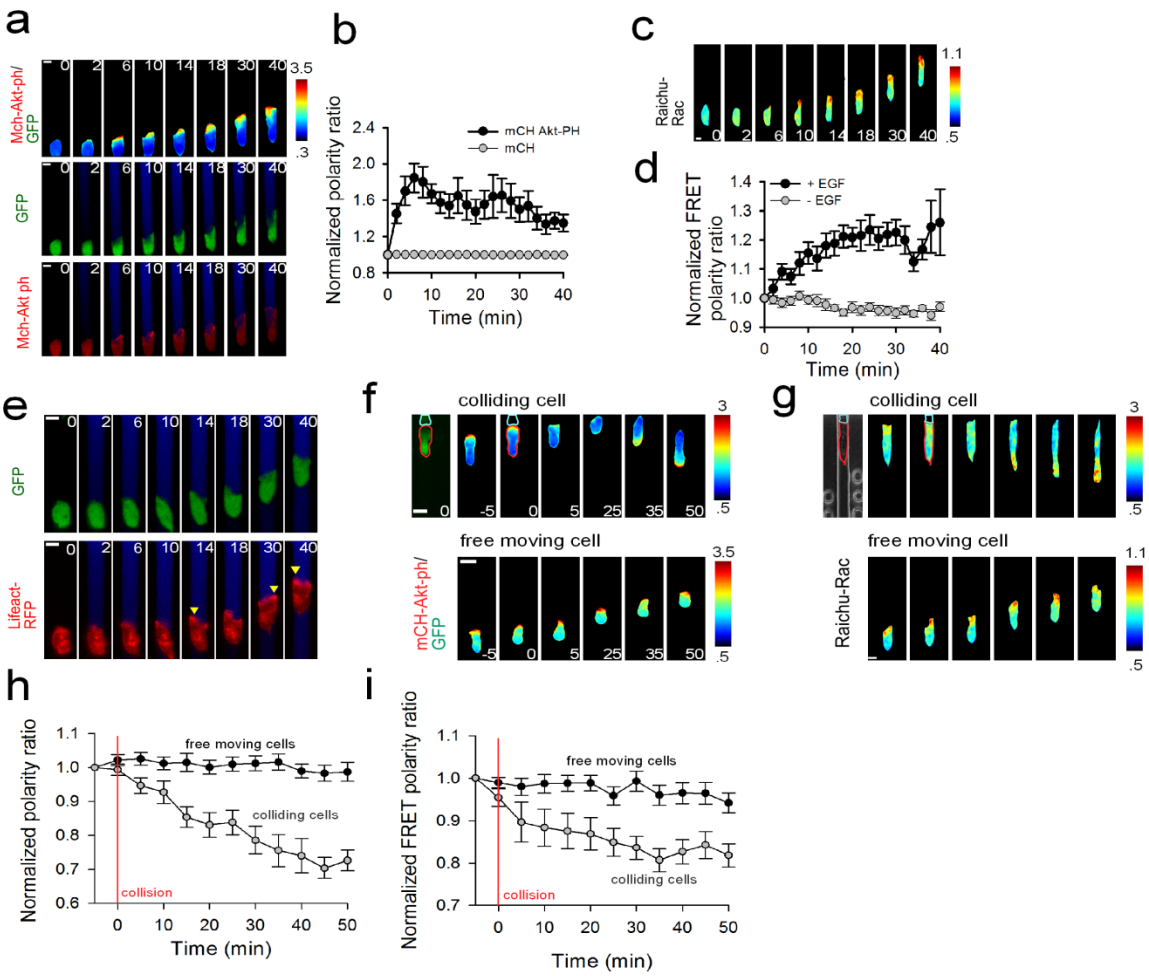

Fig. 4.8: PI3K, Rac, and F-actin are active at the leading edge during chemotaxis and are inhibited by CIL

(a) Representative images of PI3K activity during MTLn3-B1 chemotaxis to EGF (15-35 ng/ml). The pseudcolor images in the top panel represent the ratio between Mch-Akt-ph and GFP. Green color in the middle panel visualize GFP expression. Red color in the bottom panel displays Mch-Akt-ph. **(b)** Quantification of the polarity ratio in chemotaxing mCh-Akt-ph expressing MTLn3-B1 cells vs. control mCh expressing cells. Data represents the mean of n >= 20 cells per condition from n = 3 independent experiments. Error bars are SEM. **(c)** Representative images of Rac activity during MTLn3-B1 chemotaxis to EGF (15-35 ng/ml). Pseudocolor images show the FRET ratio (YFP FRET/CFP) from the Raichu-Rac construct. **(d)** Quantification of the FRET polarity ratio in MTLn3-B1 cells with and without a gradient of EGF. Data represesents the mean from n >= 12 cells from n = 3 independent experiments. Error bars show SEM. **(e)** Representative images of the localization of F-actin during MTLn3-B1 chemotaxis to EGF (15-35ng/ml). Green color in the top panel indicates expression of GFP. Red color in the bottom panel displays Lifeact-RFP. Yellow arrows highlight localized enrichment of F-actin. *Cont-*

Cont- (**f-g**) Visualization of (**f**) PI3K activity and (**g**) Rac activity during CIL.. Collisions occur at time t = 0. The top series of images illustrate colliding cells while the bottom series illustrates free moving cells. The first image in each of the top series of images visualizes the collision, showing the tracked cell outlined in red and the cell it is colliding with in blue. These outlines are reproduced in the ratio image at time = 0. Pseudocolor images represent the ratio between Mch-Akt-ph and GFP in (**f**) and the FRET ratio (YFP FRET/CFP) in (**g**). (**h-i**) Quantification of the polarity ratio in colliding cells and free moving cells for (**h**) PI3K and (**i**) Rac. Free moving cells retain a constant polarity while colliding cells exhibit a decrease after the collision. Data represents the mean from n >= 11 cells per condition from 3 independent experiments with error bars representing SEM. Times are in minutes. Scale bars, 10 μm.

(**Fig. 4.8b**). Conversely, a control mCherry construct without a ph domain did not show any polarization (**Fig. 4.8b**, **Fig. 4.9a**). Next, we used a Raichu-Rac FRET sensor to

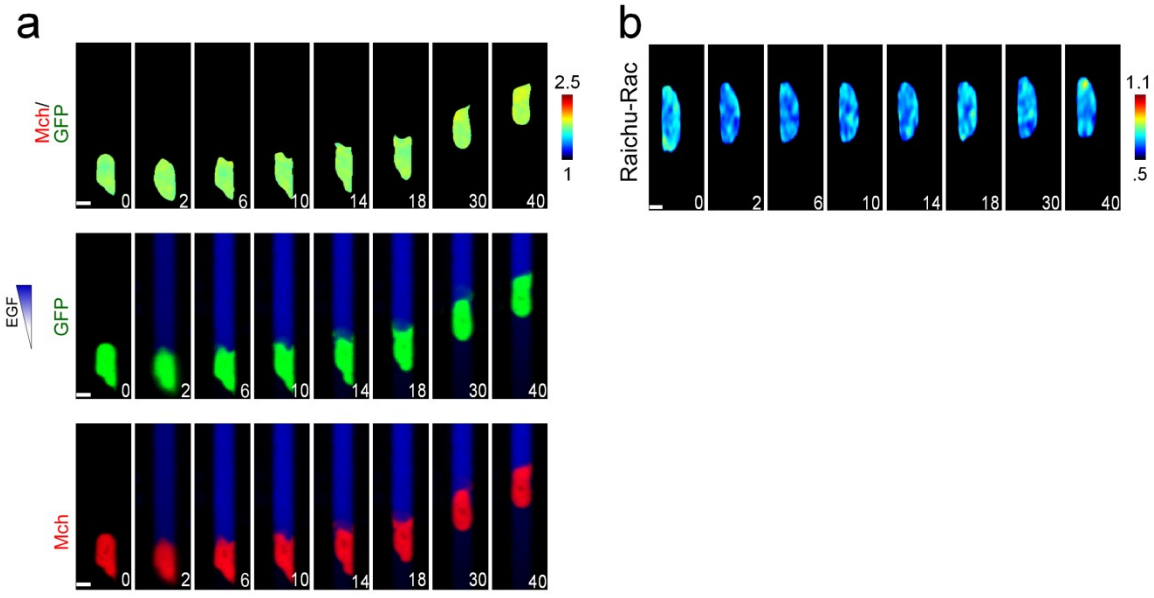

Fig. 4.9: PI3K and Rac activity controls.

(**a**) A representative time series of a MTLn3-B1 cell expressing GFP and Mcherry chemotaxing to a gradient of EGF (15-35 ng/ml). The pseudocolor in the top series of images represents the ratio between Mcherry and GFP. Green color denotes GFP expression, red color denotes Mch expression, and the blue color visualizes the EGF gradient via a dextran dye. Quantification of control data is found in **Fig. 3b**. (**b**) Representative time series of a MTLn3-B1 cell expressing a Raichu-Rac FRET sensor in a microchannel without EGF. Cells do not polarize and remain stationary. The pseudocolor represents the FRET ratio (YFP FRET/CFP). Quantification of control data is found in **Fig. 3d**. Times are in minutes. Scales bars, 10 μm.

observe Rac activity during MTLn3-B1 EGF chemotaxis (**Fig. 4.8c**). Similar to PI3K, Rac also became locally activated at the cell front in EGF gradients (**Fig. 4.8c**), but with slower kinetics (**Fig. 4.8d**). Without EGF, Rac FRET activity remained unpolarized (**Fig 4.8d**, **Fig. 4.9b**). We also looked at the localization of F-actin during MTLn3-B1 chemotaxis, as Cofillin, an actin severing protein, has been shown to be important for directional migration in MTLn3 cells[202]. Using a mCherry tagged Lifeact sensor to detect F-actin, we observed F-actin spikes localized to the front of chemotaxing MTLn3-B1 cells (**Fig. 4.8e**), suggesting that in our assay, chemotaxing MTLn3-b1 cells migrate with F-actin mediated protrusions. Overall, our results indicate that the activity PI3K, Rac, and F-actin are polarized towards the front of MTLn3-B1 cells during EGF chemotaxis.

We next assessed if PI3K and Rac were regulated by CIL by tracking their activity during cell collisions (**Fig. 4.8f-g**). As a control, we compared their activity during collisions to freely chemotaxing MTln3-B1 cells (**Fig. 4.8f-g**). Freely chemotaxing MTLn3-b1 cells maintain constant PI3K and Rac activity at the cell front (**Fig. 4.8f-i**). Conversely, cell collisions induce a local downregulation of both PI3K and Rac at the leading edge of MTLn3-B1 cells as protrusions collapse (**Fig. 4.8f-i**). When contacting MTLn3-B1 cells repolarize and migrate in the opposite direction, PI3K and Rac relocalize to the new protrusion, leading to a decrease in the polarity ratio (**Fig. 4.8h-i**). Taken together, these results suggest that PI3K and Rac may be targets of regulation by CIL.

4.2.7 Activation of Eph B signaling is sufficient to induce CIL

Next, we sought to identify the molecular components which induce CIL in MTLn3-B1 cells. As the upstream mediators of CIL in MTLn3-B1 cells are unknown, we set up a series of obstacles to assess their ability to induce CIL during chemotaxis to EGF (**Fig. 4.10a**). We first investigated two mechanical barriers by seeding either 3T3 fibroblasts or 5 μm diameter protein A coated silica beads directly into microchannels and inducing MTLn3-B1 chemotaxis towards them (**Fig. 4.10a**). Although 3T3 cells encompassed most of the microchannel, we surprising found that the majority of chemotaxing MTLn3-b1 cells could migrate around and actively displace them (9/10 collisions result in migration past 3T3 cells) (**Fig. 4.10b**). This result suggests two ideas- first, that signaling plays a prominent role in inducing CIL, as the mechanical properties of 3T3s should be roughly similar to those of MTLn3-B1 cells, and second, that MTLn3-B1 display reduced heterotypic CIL, which has been noted in other cancer cells[52, 203] and is thought to increase malignancy. Next, we studied collisions between chemotaxing MTLn3-B1 cells and protein A coated silica beads. Single protein A coated silica beads only took up roughly 1/3 of the width of a microchannel, nonetheless, the resulting MTLn3-B1 bead collisions did induce some repulsion events (**Fig. 4.10c-d**), indicating that there may be some mechanical contributions to MTLn3-B1 CIL. The majority of collisions, however, did not affect chemotaxing MTLn3-B1 cells (**Fig. 4.10d**), suggesting again that signaling predominantly mediates CIL in MTLn3-B1 cells.

Protein A coated silica beads can be functionalized with fc tagged proteins and can be used to screen for proteins which induce CIL. We therefore screened a set of fc tagged proteins known to mediate CIL in other cell systems and assessed their ability to induce CIL in chemotaxing MTLn3-B1 cells (**Fig. 4.10a**). As a control, we first studied

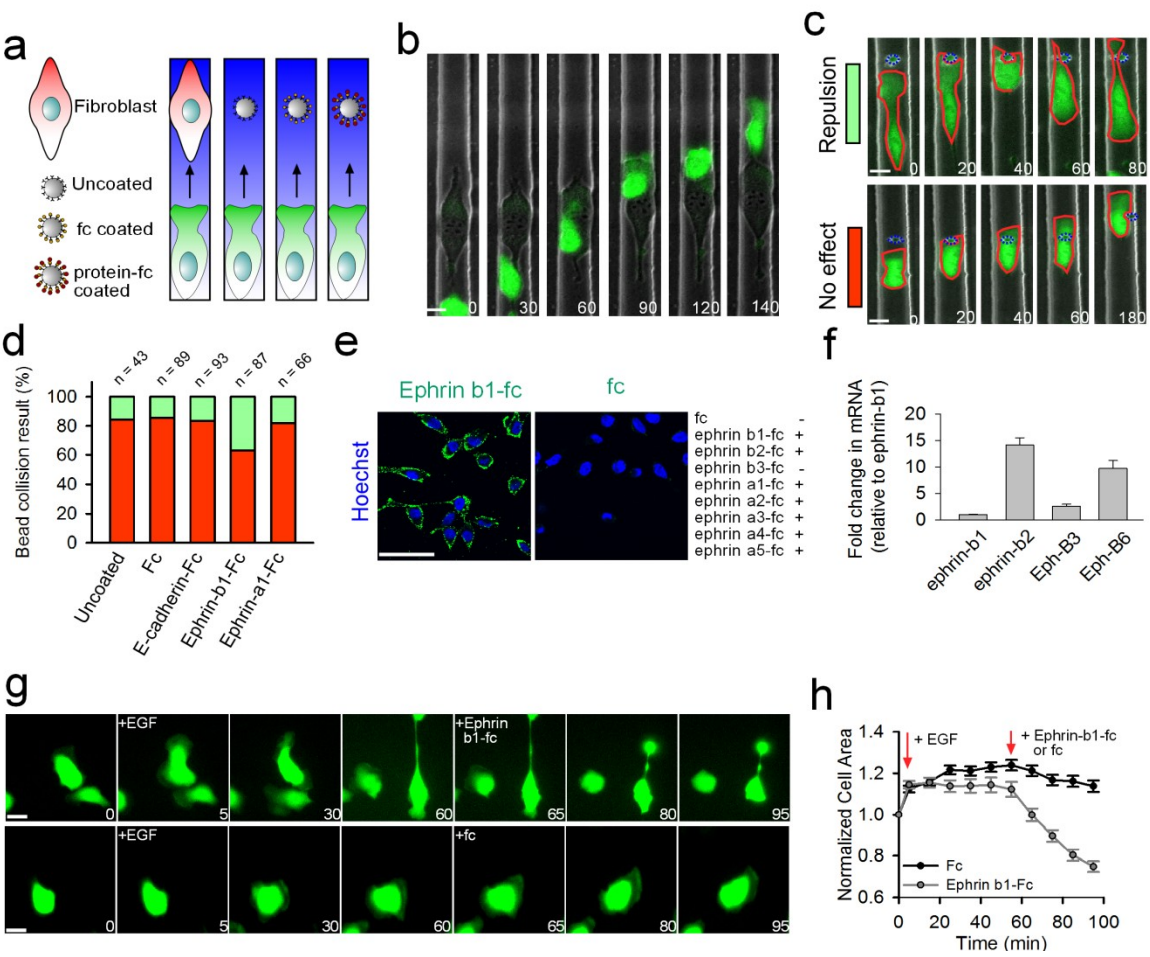

Fig. 4.10: Eph B signaling is sufficient to induce CIL in MTLn3-B1 cells

(a) Schematic of the different obstacles assessed for their ability to induce CIL in chemotaxing cells (15-35 ng/ml EGF gradients). **(b)** Selected images of a MTLn3-B1 cell colliding and migrating around a 3T3 cell during chemotaxis. Green color indicates expression of GFP and identifies the MTLn3-B1 cell. **(c)** Representative images of cells undergoing repulsion (top panel) or being unaffected (bottom banel) by protein A coated silica beads during chemotaxis. Red dashed lines highlight the boundaries of cells shown in green. Blue dashed lines outline silica beads. Times are in minutes. Scale bars, 10 μm. **(d)** Quantification of the results of MTLn3-B1 bead collision events during chemotaxis with different silica bead coatings. Number to total collisions analyzed per condition is indicated from n >= 2 independent experiments. **(e)** Visualization of the binding of ephrin-b1-fc or fc to cells by immunostaining against the fc domain (shown in green). Nuclei are denoted in blue with A summary table is shown on the right for all tested ephrin-fc ligands. Scale bars, 50 mm. **(f)** Relative expression of ephrin b ligand and Eph B receptors in MTLn3-B1 cells from real time RT-PCR. Data represents the mean from n = 3 biological replicates. Error bars are SD. **(g)** Selected images of MTLn3-B1 cells stimulated with EGF and then treated with either clustered ephrin b1-fc (Top panel) or fc (Bottom panel). Green color indicates expression of GFP. Times are in minutes. Scale bars, 20 μm. **(h)** Cell area after indicated treatments in **g**. Data is the mean from n >= 90 cells per condition from n = 3 independent experiments. Error bars are SEM.

the ability of the fc domain itself to induce CIL. Fc domain coated beads induced cell repulsion with an equal probability to that of uncoated protein A beads, indicating that the fc domain itself did not provide any signaling (**Fig. 4.10d**). Next, we tested E-cadherin, as cadherins have been shown to mediate CIL in xenopus neural crest cells[189] and myoblasts[204]. E-cadherin is known to be upregulated in metastatic MTLn3 cells as compared to nonmetastatic variant MTC cells[191] and could be detected with immunostaining (**Fig. 4.11a**). Our results indicated that E-cadherin-fc coated silica beads did not significantly increase the chance of repulsion of chemotaxing MTLn3-B1 cells (**Fig. 4.10d**). Therefore, we next looked to the Eph receptor systems, which are responsible for CIL in a variety of systems, such as axon guidance[188, 205], prostate cancer cells[52], and endothelial cells[206].

The Eph receptors are the largest family of receptor tyrosine kinases[207] (RTKs) and can be split into A and B families based on their affinity for glycosylphospatidylinositol (GPI) linked ephrin a or transmembrane ephrin b ligands[208]. To test the ability of Eph receptor and ephrin ligand interactions to induce CIL in chemotaxing MTLn3-B1 cells, we functionalized beads with either ephrin b1-fc or ephrin a1-fc, which can promiscuously bind Eph B and Eph A receptors[209], respectively. Ephrin b1-fc, but not ephrin a1-fc, coated beads increased the probability of contact repulsion with MTLn3-B1 cells, suggesting that activation of Eph B receptors via ephrin ligands is sufficient to induce CIL in these cells (**Fig. 4.10d**). We verified the presence of Eph B receptors on MTLn3-B1 cells by incubating live MTLn3-B1 cells with various unclustered soluble ephrin b-fc ligands and immunostaining without permeabilization against the fc domain at 4°C to prevent internalization (**Fig. 4.10e**, **Fig. 4.11b**).

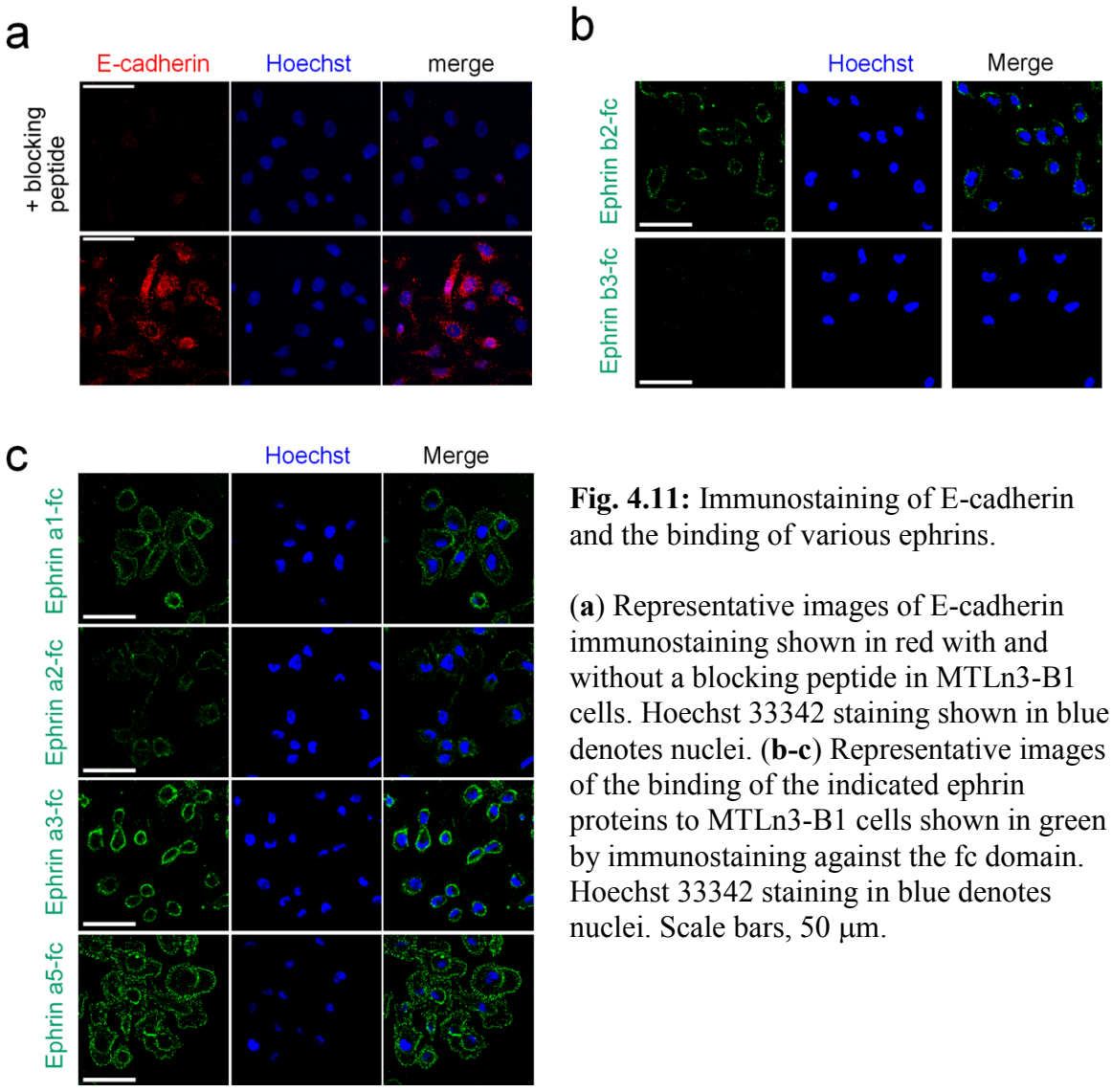

Fig. 4.11: Immunostaining of E-cadherin and the binding of various ephrins.

(**a**) Representative images of E-cadherin immunostaining shown in red with and without a blocking peptide in MTLn3-B1 cells. Hoechst 33342 staining shown in blue denotes nuclei. (**b-c**) Representative images of the binding of the indicated ephrin proteins to MTLn3-B1 cells shown in green by immunostaining against the fc domain. Hoechst 33342 staining in blue denotes nuclei. Scale bars, 50 μm.

Incubation with the fc domain itself did not produce any signal, indicating that the binding of the ephrin b ligands was specific to their substrates, the Eph B receptors (**Fig. 4.10e**). We also verified that MTLn3-B1 cells express Eph A receptors by incubation and subsequent immunostaining with various ephrin a-fc ligands (**Fig. 4.11c**). Ephrin-fc ligand binding results are summarized in **Fig. 4.10e**. Finally, we performed real time RT-PCR in MTLn3-B1 cells to verify the expression of various ephrin b and Eph B transcripts (**Fig. 4.10f**). Ephrin b2 was the predominant ephrin b isoform, however, it

retained similar cell surface binding to ephrin b1 (**Fig. 4.10e**, **Fig. 4.11b**), suggesting that both ephrin b ligands bind Eph B receptors on MTLn3-B1 cells with similar affinity. Overall, our results demonstrate that MTLn3-B1 cells express both ephrin b ligands and Eph B receptors and thus possess the necessary components to induce homotypic CIL.

To clarify the functional effects of Eph B signaling, we tested whether soluble, clustered ephrin-b1 fc could produce functional retraction in EGF stimulated MTLn3-B1 cells. We performed live cell imaging experiments where we first added EGF to MTLn3-B1 cells to induce protrusion formation and then subsequently added either clustered ephrin b1-fc or clustered fc (**Fig. 4.10g**). Clustered ephrin-b1-fc induced significant cell retraction while fc treatment had no effect (**Fig. 4.10h**), suggesting that Eph B signaling is functionally sufficient to suppress protrusions in EGF stimulated MTLn3-B1 cells.

4.2.8 Crosstalk between chemotaxis and CIL occurs above PI3K

After identifying Eph B signaling as an upstream mediator of CIL in MTLn3-B1 cells, we next sought to identify what components downstream of Eph B interact with the chemotaxis pathway. One molecule likely to be downstream of Eph B is RhoA, a member of the small Rho GTPases previously shown to be a mediator of contact repulsion in growth cones, neural crest cells, and prostate cancer cells. RhoA is also known to have an antagonistic relationship with Rac, and therefore could potentially inhibit chemotaxis through Rac. To observe RhoA activity during either EGF or clustered ephrin b1-fc treatment, we used a Dora-Rho FRET construct (**Fig. 4.12**). Surprisingly, we found that RhoA activity increased upon the addition of EGF, but not ephrin-b1 fc

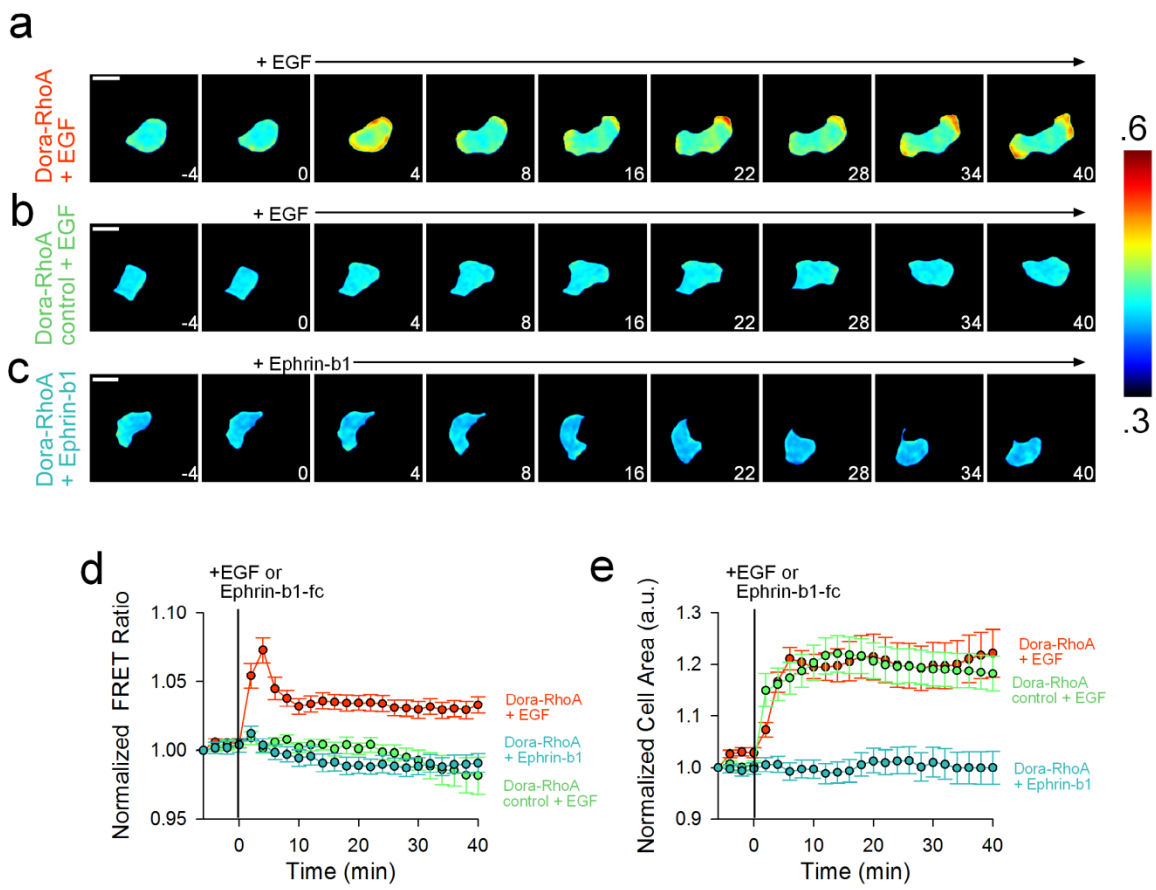

Fig. 4.12: RhoA is not activated by Eph B signaling.

(**a-b**) Representative images of RhoA activity from Dora-RhoA FRET(**a**) or control Dora-Rhoa FRET(**b**) constructs in MTLn3-B1 cells during EGF stimulation. (**c**) Representative images of RhoA activity from a Dora-Rhoa FRET construct in MTLn3-B1 cells during ephrin b1-fc stimulation. Times are in minutes. Scale bars, 20 μm. (**d-e**) Quantification of the FRET ratio (**d**) and cell area (**e**) in the conditions specified above. Data indicates the mean from n >= 26 cells per condition from n = 3 independent experiments with error bars representing SEM.

(**Fig. 4.12a-d**). A point mutated, control Dora RhoA construct did not show an increase with EGF stimulation (**Fig. 4.12b**). These results suggest that RhoA is not downstream of Eph B receptors in MTLn3-B1 cells. The addition of EGF lead to protrusion formation and similar increases in cell area in MTLn3-B1 cells endowed with either FRET construct (**Fig. 4.12e**). However, application of ephrin b1-fc did not induce cell retraction (**Fig. 4.12e**). This was in stark contrast to the MTLn3-B1 cell retraction observed after

the addition ephrin b1-fc in the context of EGF stimulation (**Fig. 4.10g-h**), suggesting that Eph B signaling in MTLn3-B1 cells may function by suppressing components activated by EGF signaling without actively signaling to contractile machinery. To test this idea, we pretreated MTLn3-B1 cells with clustered ephrin b1-fc before adding EGF (**Fig. 4.13a**). We hypothesized that if Eph B signaling mobilizes inhibitory machinery, then EGF mediated cell spreading would be diminished. Indeed, we found that pretreatment with ephrin b1-fc attenuated EGF induced cell spreading (**Fig. 4.13a-b**), suggesting that Eph B signaling induces CIL by suppressing EGFR signaling.

We next sought to identify which components downstream of EGFR were inhibited by Eph B signaling. Earlier, we showed that PI3K was activated in gradients of EGF and was inhibited by cell contact. Therefore, PI3K could potentially be inhibited by Eph B signaling. To assess the possible regulation of PI3K by Eph B signaling, we used chemically induced heterodimerization (CID) technologies to directly activate PI3K by translocating its activator to the plasma membrane after ephrin b1-fc pretreatment (Supplementary Fig. S8c-d). We did not find any significant differences in cell spreading after direct activation of PI3K with and without ephrin b1-fc pretreatment (Supplementary Fig. S8c-d), suggesting that Eph B mediated inhibition of EGFR signaling occurs between PI3K and EGFR. To confirm this, we performed similar experiments for Rac (Supplementary Fig. 8e-f), generally agreed to be downstream of PI3K, and found that ephrin-b1 pretreatment did not affect Rac mediated cell spreading. Taken together, these results suggest that Eph B signaling inhibits EGFR signaling upstream of PI3K.

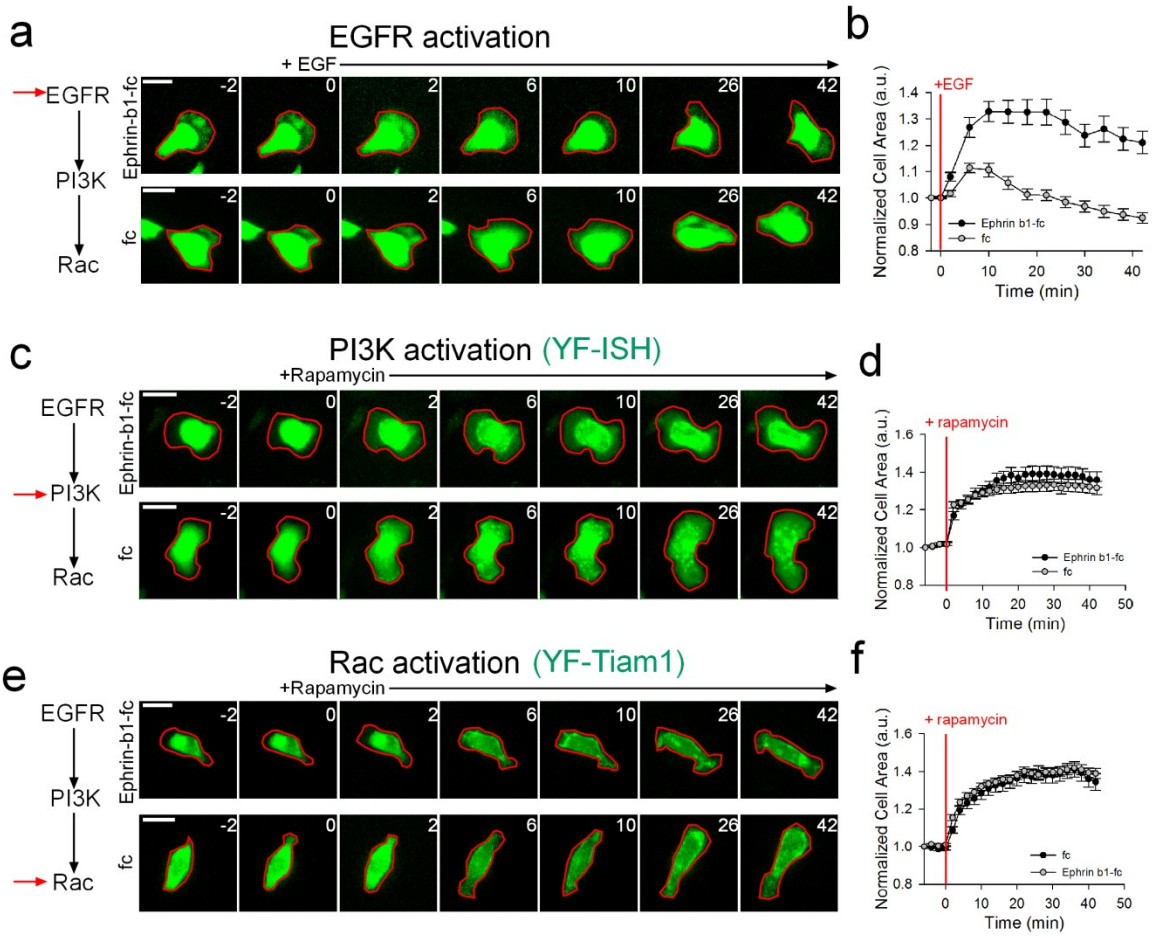

Fig. 4.13: Eph B inhibition of EGFR signaling occurs upstream of PI3K.

In all conditions, MTLn3-B1 cells are pretreated with either clustered ephrin b1-fc or fc for 45 minutes before the addition of either EGF or rapamycin. (**a**) Representative images of MTLn3-B1 cells responding to EGF with either ephrin b1-fc or fc pretreatment. Red outlines trace cell boundaries. Times are in minutes. Scale bars, 20 μm. (**b**) Quantification of cell area after EGF stimulation from (**a**). Data is the mean from n >= 80 cells per conditions from n = 3 independent experiments with error bars being SEM. (**c,e**) Representative images of direct (**c**) PI3K or (**e**) Rac activation after the addtion of 100 nm rapamycin with either ephrin b1-fc or fc pretreatment. Red outlines trace cell area. Times are in minutes. Scale bars, 20 μm. (**d,f**) Quantification of cell area after activation of PI3K(**d**) or Rac (**f**) with 100 nm rapamycin after indicated pretreatments. Data indicates the mean from n >= 40 cells per condition from n = 3 independent experiments with error bars representing SEM.

4.3 Discussion

We have developed a new set of devices to individually and collectively address chemotaxis and CIL in single breast cancer cells in a high throughput and well controlled manner. These devices allow the real time observation of MTLn3 chemotaxis in different gradients of EGF and how CIL affects these processes. We compare CIL in uniform vs. gradients of EGF and make the striking observation that chemotaxis and CIL do not act independently when both cues are present. This is demonstrated by our findings that tuning the strength of chemotaxis signaling can alter the balance between these two cues (**Fig. 4.14a**). Overexpression of EGFR and optimal EGF gradients increase the influence of chemotaxis over CIL, as evidenced by the shift in collision outcomes towards the gradient. Conversely, suboptimal EGF gradients, which elicit weaker chemotactic responses, do not produce any shifts.

We further identify molecular components involved in chemotaxis and CIL in MTLn3 cells and identify where these respective pathways might crosstalk. During chemotaxis, MTLn3 cells respond to gradients of EGF by activating PI3K, Rac, and F-actin at the leading edge (**Fig. 4.14a**). PI3K and Rac retain persistent activity at the leading protrusion in freely chemotaxing MTLn3 cells and are inhibited by CIL. We find that CIL in MTLn3 can be mediated through Eph B signaling (**Fig. 4.14a),** as evidenced by the increased probability of cell repulsion with ephrin b1 coated beads and cell retraction induced by the addition of exogenous ephrin b1 ligands. Crosstalk between chemotaxis and CIL occurs below EGFRs and above PI3K (**Fig. 4.14a**).

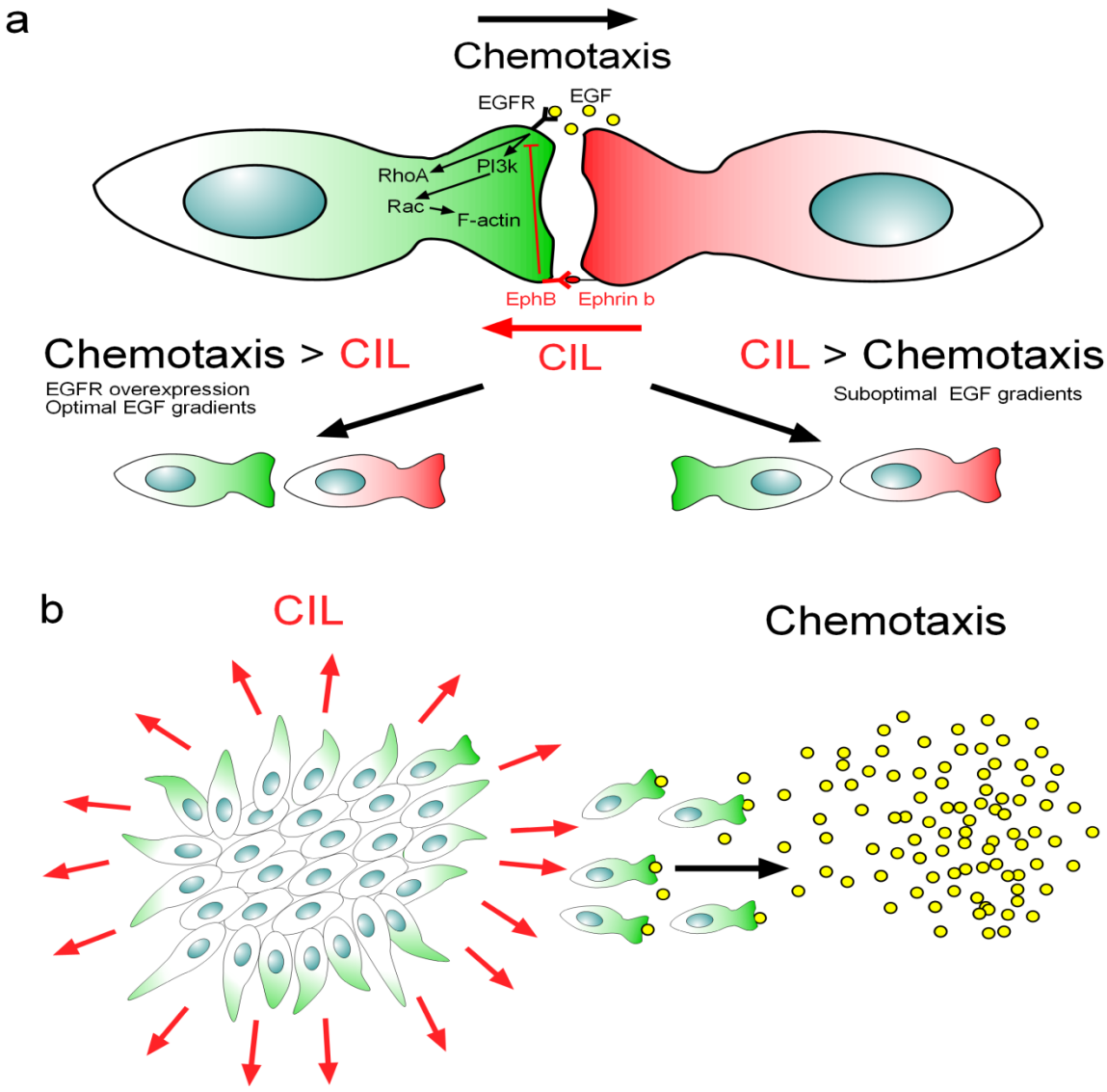

Fig. 4.14: Interplay between CIL and chemotaxis optimizes cell dispersion.

(**a**) CIL presents an efficient search strategy by preferentially directing cells away from cell clusters to explore new space. This cell dispersal enhances the probability of finding chemical gradients to initiate chemotaxis. Chemotaxis is an efficient mechansism to direct cell motility to specific locations. (**b**) The interplay between CIL and chemotaxis is mediated in MTLn3 cells by regulation of EGF (chemotaxis) and EphB/ephrin b (CIL) signaling. Various conditions can shift the balance from one pathway to the other, resulting in the preferential redirection of collding cells.

Where might EphB signaling inhibit EGF signaling between EGFR and PI3K to induce the collapse of protrusions? We found that one of the likely candidates, RhoA,

was not activated in MTLn3 cells in response to EphB signaling (**Fig. 4.12**). Moreover, we found that induction of EphB signaling without prior EGF signaling did not induce cell retraction, suggesting a mechanism of regulation where contractile machinery is not activated by Eph B. We propose, instead, that in MTln3 cells, Eph B signaling induces the collapse of cellular protrusions by directly inhibiting EGF signaling or other factors which induce migration. Therefore, we suggest two possibilities based on the current understanding of Eph signaling. One possible mechanism is through R-Ras, a member of the Ras family of small GTPases[210]. R-Ras can activate PI3k[210, 211] and has been shown to be inactivated by Eph receptors[209]. Another possible mechanism is through endocytosis of EGFR receptors. Previous groups have shown that in cells which demonstrate CIL through Eph B signaling, EphB receptors and ephrin b ligands are trans-endocytosed when cells collide[212, 213], serving as a mechanism for downregulation of Eph receptor signaling. Co-endocytosis of EGFR during these trans-endocytosis events may mediate inhibition of EGF signaling.

A prominent system where the contributions of chemotaxis and CIL during directional migration have been investigated are in neural crest cells[190]. Neural crest cells migrate as a cell cluster with transient cellular interactions. CIL between neural crest cells is mediated through N-cadherin which activates RhoA, which then antagonizes Rac, leading to the collapse of cellular protrusions[214]. During collective neural crest migration, CIL directs protrusions away from the cell cluster and gradients of SDF-1 in turn serve to stabilize these protrusions to generate productive directed migration[190]. The gradients of SDF-1 themselves are not sufficient to induce a directed response without CIL, as mutations of N-cadherin or a reduction in cell density abrogate directional migration[190].

Conversely, we show here that in MTLn3 cells, where directional migration occurs primarily on a single cell basis along collagen fibers[196], chemotaxis to EGF serves as the main driving for inducing directed migration. In some aspects, CIL is a secondary factor, as directed migration can still occur efficiently in the absence of CIL. We also find that CIL mediated inhibition of cell protrusions does not occur through RhoA, but through inhibition of upstream EGFR signaling.

In the context of metastasis, we suggest that being responsive to both CIL and chemotaxis is an optimized strategy for cell dispersion, as each cue imparts its own distinct advantages (**Fig. 4.14b**). Acquisition of homotypic CIL is an effective search strategy which directs cells away from the cell population, maximizes the exploration space, and can occur in the absence of an external stimulus (**Fig. 4.14b**). For example, CIL is sufficient to spread out initially clustered cell populations and drive the uniform distributions of Cajal-Retzius cells[215] and haemocytes[216]. This in turn increases the probability of finding sources of chemical gradients from exit targets, such as blood vessels or lymph nodes (**Fig. 4.14b**). Once these chemical gradients are detected, chemotaxis serves as a potent cue in eliciting a strong directional migration response.

However, being responsive to both CIL and chemotaxis could have potential drawbacks. For example, cells collisions between chemotaxing cells could redirect cells away from their intended targets and reduce overall chemotactic efficiency. Our results demonstrate that CIL outcomes shift in the presence of chemical gradients and thus provide a mechanism to mitigate these drawbacks. In optimal chemical gradients, HH collisions outcomes are biased towards both cells moving up the gradient. This switch in behavior allows inaccurate cells to be repolarized back up the chemical gradient by

trailing cells, thus preserving the fidelity of the original intended direction. Furthermore, we find that in optimal chemical gradients, HT collision induced CIL is suppressed. Therefore, collision induced repulsion between streaming cell populations during chemotaxis would be repressed.

Overall, we show here how multiple guidance cues can be interpreted at a single cell level and how the resulting interactions can produce beneficial phenotypes. We suggest that multiple guidance cues act in a dependent manner, that is dynamic and context dependent.

4.4 Materials and Methods

4.4.1 Cell culture and reagents

MTLn3 GFP, MTLn3-B1 GFP, and MTLn3-B1 cells were a gift from J. Segall (Albert Einstein, NY). MTLn3 GFP, MTLn3-B1 GFP, and MTLn-B1 cells were maintained in αMEM (Cellgro) with 5% FBS (Gibco) and 1% penicillin/streptomycin (Sigma). 3T3 cells were cultured in DMEM (Cellgro) with 10% FBS (Gibco) and 1% penicillin/streptomycin. All cell lines were cultured in a humidified 37 $^{\circ}$C and 5% CO_2 incubator. EGF and Rat tail collagen 1 were obtained from Invitrogen. Ephrin-fc ligands were obtained from R&D systems. Rapamycin used in CID experiments was from LC laboratories.

The following primary antibody was used- monoclonal Rabbit anti-E-Cadherin (Cell Signaling). The following secondary antibodies were used- Goat anti human IgG Fc (Jackson Labs), FITC conjugated Goat anti human IgG Fc (Millipore), and Alexa Fluor 594 Goat anti rabbit IgG (Invitrogen).

Transfections were carried out using Fugene HD (Promega) according to manufacturers recommendation. MTLn3-B1 cells without GFP expression were used for all FRET experiments. The Raichu-Rac FRET construct was a gift from M. Matsuda (Tokyo University, Japan), while the Dora-RhoA FRET constructs were a gift from Y. Wu (UCHC, CT).

4.4.2 Device fabrication

Microfluidic devices were fabricated using a traditional two layer soft lithography process[116] out of polydimethylsiloxane (PDMS) from Momentive by replica molding off of silicon wafer masters. Silicon masters were created using standard photolithography techniques[90]. Device designs were created in Freehand MX (Macromedia) and AutoCAD (Autodesk).

4.4.3 Device protocol

Microfluidic devices were prepared by cleaning with 70% ethanol and an alconox solution. Devices were then bonded to 22 x 40 mm #1 coverglass (Fisher) and incubated

in an oven set at 80°C overnight. Before experiments, devices control valves were first filled with DI water by pressurizing with 10 PSI using solenoid valves (The Lee company). Subsequently, valves "5" and "7" (Shown in blue, Supplementary Fig. S1a) were pressurized to restrict fluid flow to the gradient generation region and a 40 μg/ml collagen 1 solution was introduced into one of the two "c" ports (Shown in green, Supplementary Fig. S1a) in order to fill the source, sink, and microchannel region. Devices were coated with collagen for 1 hour before the collagen solution was exchanged for cell medium. Cells were seeded as follows- Cells were trypsinized and resuspended in normal cell culture medium at a concentration of 10 million cells/ml. The cell suspension was then pipetted onto one of the "c" ports and induced in to the microchannel region by gravity flow. To terminate cell seeding, the valve opposite to where cells were introduced was pressurized (either valve "6" or valve "8") and the pressure in valve "5" was released to allow extraneous cells to be removed from the source and sink channels via flow from the inlet labeled "w" (shown in red, Supplementary figure S1a). Cells were allowed to adhere for 4 hours before experimentation. Typical experiments were run with cell medium solution in the sink side of the device and an EGF containing solution in the source side. Input solutions were introduced from the inlet network labeled "1-4" (Shown in green, Supplementary Fig. S1a). During the establishment of the source and sink, cells in the microchannel region were isolated by pressurizing valves "8" and "6" (Supplementary Fig. S1c). Finally, experiments were initiated when these valves were released and gradients of EGF were allowed to form across the microchannels via diffusion between the pre-established source and sink (Supplementary Fig. S1c).

4.4.4 Imaging

Live cell imaging experiments were performed on a Zeiss Axiovert 200M epifluorescence microscope with a motorized stage (Prior) in an environmental chamber set at 37 $^{\circ}$C and 5% CO_2 with a 40x, 1.3 numerical aperture oil immersion objective (Zeiss) coupled to a Cascade II:1024 EMCCD camera (Photometrics). Slidebook software (Intelligent Imaging Innovations) was used for automated control of the microscope system.

Immunostained samples were imaged on a confocal Zeiss LSM510-Meta using a 63x Planapo oil objective driven by Zen software (Zeiss).

4.4.5 Live cell imaging experiments

MTLn3 cells were seeded onto 25 mm glass coverslips (Fisher) coated with 40 μg/ml Rat Tail Collagen 1 (Invitrogen) for 1 hour at room temperature. Cells were allowed to attach overnight and then were subsequently starved for 3 hours in L15 medium with .35% BSA (Invitrogen). The glass coverslip was then transferred to Attofluor live cell imaging chambers (Invitrogen), mounted onto the microscope, and stimulated with 100 ng/ml EGF (Invitrogen) or1 μg/ml preclustered ephrin b1-fc (R&D systems). Ephrin b1-fc was preclustered at at 1:10 ratio with Goat anti-human Fc for 1

hour at 37 °C. In some experiments, EGF treatment was followed by the addition of 1 μg/ml preclustered ephrin b1-fc or 1 μg/ml preclustered fc. For chemically induced heterodimerization experiments, 100 nM of rapamycin was added.

4.4.6 Image Analysis and metrics

Image analysis was carried out using custom scripts written in Matlab 2007b (Mathworks). All images were first flatfield and darkfield corrected using the following routine- C = (I-D/F-D)*M where C = corrected image, I = initial image, D = darkfield image, F = flatfield image, and M = mean of difference between flatfield and darkfield images. Flatfield and darkfield images were obtained by averaging multiple images. Images were then Gaussian filtered to remove noise.

To analyze cell velocity and the chemotaxis index (CI), cells were semi-automatically segmented by thresholding from GFP images and position data was generated by obtaining the centroid of segmented cells. Only cells which did not come into contact with other cells were used in this analysis. The chemotaxis index is defined as the distance moved up the gradient divided by the total distance traveled. Positive values were given to migration up the gradient, while negative values were given to migration in the opposite direction.

To analyze mCherry-Akt-ph biosensor data, cell images were background subtracted and then segmented by thresholding from GFP images to create a binary mask. This mask was then multiplied into both the original mCherry image and the GFP image

to isolate the fluorescence data of a single cell. The single cell mCherry image was then divided by the single cell GFP image to obtain the ratio.

To analyze FRET data (Raichu-Rac, Dora-RhoA), we followed a previously described protocol[181]. Brielfy, CFP and YFP FRET images (CFP excitation, YFP emission) were background subtracted, thresholded based on intensity, and aligned with a dft registration algorithm. The final ratio images were obtained by dividing the YFP FRET image by the registered CFP image. Final ratio images were Gaussian filtered. FRET data from Dora-Rhoa was obtained by taking a whole cell average from the ratio image.

The polarization ratio in microfluidic experiments was obtained by segmenting ratio images into binary images. Rows of the resulting binary images were then used to define the cell length. The polarization ratio was then obtained by taking the ratio between the mean value of the front 20% of the cell length and the rear 20% of the cell length from the original ratio images. We define front as where a protrusion is generated.

CIL outcomes in microfluidic experiments were analyzed by observing GFP time series and assessing the direction of migration within 60 minutes post collision. In HT collisions, we considered cells which did not repolarize in 60 minutes as outcome 1. CIL in 2D was analyzed using a previously described metric[51, 52] by tracking cell positions 60 minutes before and after.

Cell areas under EGF stimulation were analyzed by manually segmenting cells from Phase images. Only cells which did not contact other cells were used in this analysis.

4.4.7 Immunostaining

For live cell immunostaining, MTLn3-b1 cells were seeded onto collagen coated glass coverslips and allowed to attach overnight. Cells were subsequently starved for 3 hours and incubated with either 1 μg/ml unclustered ephrin fc or fc for 5 minutes at 37 °C. Next, cells were washed thrice with cold starvation medium and then incubated with a FITC conugated Goat anti human IgG fc antibody on ice for 1 hour. Finally, cells were washed thrice in starvation medium, fixed for 15 minutes in 1% paraformaldehyde (Sigma) with Hoechst 33342 (Sigma), washed twice in PBS, and mounted onto slides (Fisher) with ProLong (Invitrogen).

All other immunostaining was carried out as follows- MTLn3-b1 cells were seeded onto collagen coated glass coverslips and allowed to attach overnight. Cells were subsequently starved for 3 hours and fixed for 25 minutes in 4% PFA, permeabilized in .1% Triton for 7 minutes, blocked with 10% Goat serum in PBS for 1 hour, incubated with primary antibodies for 1 hour, incubated with secondary antibodies with Hoechst 33342 for 1 hour, and then mounted onto glass coverslides with ProLong. PBS washes were carried out in between steps.

4.4.8 Bead preparation

5 μm protein A coated silica beads were obtained from G. Kisher. To coat beads, either 50 μg/ml fc or ephrin-fc were incubated with 1 μl of beads for 1 hour at room

temperature under agitation. After coating, beads were centrifuged and washed thrice with PBS + 1% BSA to remove weakly bound ligands and left in 4 $^{\circ}$C under gentle agitation overnight. The protein concentration in the solutions containing ephrin-fc or fc, were measured using a nanodrop (Thermo Scientific) before and after the addition of beads to confirm that beads were coated.

4.4.9 Real time RT-PCR

MTLn3 cells were harvested from cell culture dishes using RNA protect (Qiagen). An RNeasy Plus kit (Qiagen) was then used to extract RNA from MTLn3-b1 cells. cDNA was created using a Quantitect Reverse transcription kit (Qiagen). Real time RT-PCR assays were carried out on a Quantstudio system (Applied Biosystems) using Taqman gene expression assays with a Taqman gene expression mastermix (Invitrogen). The following Taqman primers were used and obtained from Invitrogen- EGFR, ephrin-b1, ephrin-b2, Eph-B1, Eph-B2, Eph-B3, Eph-B4, Eph-B6. All results were normalized to Beta Actin from the same well. Each experiment was carried out in quadruplicate in three independent biological replicates. EGFR was used as an endogenous control between MTLn3-B1 cells and MTLn3 cells.

Chapter 5. Conclusions

5.1 Summary of results

This dissertation has investigated the molecular mechanisms underlying directed cell migration and provides new insights into the intracellular signaling enabling it. Our approach capitalized on principles from engineering and the life sciences. Specifically, we developed several new microdevices which enabled intimate control of the cellular microenvironment through physical confinement and the presentation of chemical gradients. These devices were tailored to answer specific questions in directed cell migration- 1) Is the graded activity of a core component sufficient in itself to induce directed migration? 2) How are multiple cues integrated during directed migration? We anticipate that the technological advances made here will be useful, as they allow the perturbation and characterization of new cellular behavior and can be applied to other fields.

In chapter 2, we detailed the development and rationale of two new microfluidic devices utilized in chapter 3 and 4. We provided new design solutions to many of the current issues with available chemotaxis assays. The devices are high throughput, function without shear stress on cells, capable of accounting for unbalanced inputs, and can study early gradient sensing events due to the incorporation of valves which allow precise temporal control of inputs across all experimental regions. The devices increased in sophistication from chapter 3 to chapter 4, owing to the more stringent design constraints imposed by the biological questions.

In chapter 3, we developed a new technique to directly establish an intracellular gradient of protein activity without receptor activation. We utilized this technique to address a fundamental question in the field of directed cell migration- Are intracellular gradients of small Rho GTPase activity themselves sufficient to induce direction migration? This technique relies on two components, a microfluidic device to generate spatial gradients of soluble chemicals and chemically induced dimerization (CID) technologies. We demonstrated the utility of this technique by imposing gradients of different steepness of the active form of a Rho GTPase, Rac, across living cells. We found that shallow gradients of Rac alone were sufficient to direct the polarity and movement of cells and could recapitulate phenotypes of chemoattractant induced migration, suggesting that cell polarity can be defined starting from a downstream node, Rac. Based on analysis of gradient steepness and cellular response times, we developed a refined mathematical model of cell chemotaxis and found that Rac activity needed to exceed a threshold in order for cells to polarize. Finally, we suggested a novel role for an upstream kinase, PI3K, in sensitizing cells to Rac activation.

In chapter 4, we explored how cells integrate multiple directional migration cues and how this integration might be beneficial for cell dispersion. Specifically, we looked at how the interactions between chemotaxis and CIL could shape directional migration responses. Using MTLn3-B1 cells as a model cell line exhibiting chemotaxis and CIL, we first characterized chemotactic responses in different EGF gradients. Subsequently, we found that CIL could disrupt chemotaxis, leading us to characterize CIL with and without external gradients of EGF. We found that EGF gradients could bias CIL outcomes, suggesting that these cues do not function independent of each other. The balance between the guidance imposed by chemotaxis and CIL could be shifted by augmenting or diminishing chemotactic signaling through changing external EGF inputs

or overexpression of EGFR, indicating that the cross regulation of these cues is dynamic. We next characterized some of the intracellular components involved in chemotaxis and found that PI3K and Rac were activated at the leading edge of MTLn3 cells. These same molecules were subject to downregulation upon the initiation of CIL, suggesting that they might be targets of regulation from CIL. As the molecular mediators of CIL in MTln3 cells are unknown, we developed a cell collision assay where chemotaxing MTLn3 encountered beads coated with various proteins previously shown to mediate CIL in other systems. We found that Eph B signaling, initiated during contact with ephrin b ligand coated beads, was sufficient to induce CIL and demonstrated that MTLn3 cells express both the ligand, ephrin b and receptors, Eph B. Application of the exogenous ephrin b ligand was sufficient to induce cellular retraction, further suggesting that Eph B signaling was the primary mediator of CIL in MTLn3 cells. Surprisingly, we found that Eph B did not active RhoA, one of the downstream effectors of CIL in many systems, suggesting that Eph B may induce CIL by inhibiting EGF signaling. Finally, we used CID to suggest that the crosstalk between Eph B and EGF signaling occurs above PI3K.

5.2 Future outlook and directions

We anticipate that the techniques developed in this dissertation should be applicable to other questions in directed cell migration and other areas of cell biology dependent on graded inputs. We will enumerate several possibilities below.

5.2.1 Graded Signaling

The technological platform developed in Chapter 3 should be applicable to studying other signaling species involved in directed migration as long as the limitations of the technique are kept in mind. One of the main limitations is the lack of reversibility, as rapamycin binds to both FRB and FKBP with very high affinity. This means that the graded signaling across a cell will inevitably saturate and become uniform across a cell with continuous stimulation. However, if this saturation period is delayed, for example, by using lower concentrations of rapamycin, there will be a time window where graded signaling will be maintained. Alternatively, we showed that using a pulse of graded rapamycin was sufficient to induce a response. This pulse should be sufficient to induce a graded distribution of activators and the removal of external rapamycin should theoretically ensure that this distribution does not change. However, these distributions may evolve due to lateral diffusion of FKBP-FRB-rapamycin complexes. We suggest another alternative technique is to simultaneously add a gradient of a second dimerizer during stimulation with graded rapamycin. Our lab recently demonstrated that the addition of an orthogonal dimerizer could turn off rapamycin dimerization induced signaling[217]. A careful titration between the concentrations of both dimerizers should allow the maintenance of graded signaling. A second limitation of this technique is that it is only currently applicable to proteins activated at cell membranes. However, given that the vast majority of signaling in directed migration occurs at the cell membrane, we do not anticipate this to be a major roadblock. There is a vast and ever-expanding library of rapamycin activatable molecular species, including activators of other canonical

migration components, such as Cdc42, RhoA, Ras, PI3K etc. We suggest that graded activation of these components should reveal interesting signaling hierarchies and allow the testing of positive or negative feedbacks through the addition of pharmacological compounds. Molecules which can directly induce curvature, such as Bin–Amphiphysin–Rvs (BAR) represent another interesting research area. It will be fascinating to test whether localized, graded curvature will be sufficient to induce cell migration. Finally, our technique could be used to explore how cell polarization is regulated, for example, by locally recruiting PAR complexes.

5.2.2 Chemotaxis in Cancer

We anticipate that the microdevices utilized in this dissertation will allow a more in depth look at the gradient sensitivity of different cancer cells and other slower migrating cells in general. Most current chemotaxis studies are carried out in neutrophils and dictyostelium, which migrate about an order of magnitude faster than their slower counterparts (cancer cells, fibroblasts)[36]. This faster migration allows the use of simpler chemotaxis assays, such as the micropipette assay. Although micropipettes have been utilized to study chemotaxis in cancer cells[196] and fibroblasts[35], these assays are relatively short lived and are low throughput. Another compounding issue is that substantial chemotaxis in these cell types occurs on the time scale of hours. We showed in Chapter 4**,** that we could assay chemotaxis in hundreds of MTLn3 breast cancer cells in a single experiment for over 8 hours. This allowed us to map out the EGF gradient sensitivity of MTLn3 cells. We

anticipate that similar studies will be possible in other breast cancers cell lines and other migratory cancer cells.

Generally speaking, mechanistic insights into cancer cell chemotaxis are relatively sparse when compared to neutrophils, dictyostelium, and even fibroblasts. For example, it is unknown whether intracellular gradient amplification occurs or whether cancer cells adapt to external chemoattractants. We believe that research in this area will be aided by the tools developed in this dissertation. Many of the seminal studies carried out in neutrophils, dictyostelium, and fibroblasts have been carried out through the use of fluorescently tagged biosensors. We show in chapter 4 that our device is compatible with such sensors, by visualizing the activity of canonical chemotaxis mediating proteins, PI3K and Rac. It will be interesting to compare chemotaxis paradigms between different cell types and to speculate on why these differences might occur.

Our microdevices currently assay chemotaxis in 1D, where cells migrate along a collagen coated glass coverslip. In reality, chemotaxis in vivo occurs in 3D, where a given cell may receive input from the ECM around the entire cell diameter. It will be of interest to implement gels into the microchannels of our current devices and to assess chemotaxis through them. A recent paper from the Sixt group recently correlated *in vivo* chemokine deposited gradients with *in vivo* dendritic cell guidance[218], suggesting a mechanism in which long term guidance could be achieved. We propose that a similar assay could be carried out *in vitro* with MTLn3 cells by pre-depositing EGF gradients across collagen gel filled microchannels. Alternatively, macrophages, shown to be sources of EGF for cancer cells[219], could be patterned on one side of a gel with MTLn3 on the other. Such assays may more faithfully recreate the *in vivo* guidance scenarios. An

additional benefit to studying directed migration through collagen gels in our system could be the simplification of imaging. The pseudo one dimensional environment narrows the plane in which a chemotaxing cell could reside and thus may allow faster imaging. Imaging multiple Z planes is typically a rate limiting step in 4D imaging.

5.2.3 Perspective on microfluidics

A current trend in microfluidics is to simplify device setup and implementation in order to increase their use among the general scientific community. For example, in the cell migration community, there are a variety of companies which offer simple microfluidic devices for population level assays. However, I would argue that the future of microfluidics should branch not only towards simplification, but also towards increased complexity. Adding complexity is justified in applications which require sensitive control, such as those presented here. More complex assays should also be possible with the refinement of new modules within microfluidic devices. For example, the development of microfluidic valves from the Quake group[116], greatly expanded the applications of microfluidics.

Another current trend is to use microdevices as proxies for physiological or pathological processes, such as in the Organ on a chip project. This necessitates a bridge in scale between the hundreds of cells typically used in microdevices to the level of tissues. We suggest that 3D printing technologies will become more and more prominent in this area, as the typical Z restrictions found in photolithography are absent. This

freedom in the Z dimension should allow the fabrication of shapes which are currently impossible with current microfluidic techniques.

5.3 Final thoughts

This dissertation represents a multi-faceted approach to studying cell biology, where techniques from engineering and concepts from the life sciences were integrated to allow the exploration of new questions in directed cell migration. We believe that similar multi-disciplinary, tailored approaches will continue to become more frequent in the scientific community.

Bibliography

1. Keller, R. Cell migration during gastrulation. *Current Opinion in Cell Biology* **17**, 533-541 (2005).
2. Mortimer, D., Fothergill, T., Pujic, Z., Richards, L.J. & Goodhill, G.J. Growth cone chemotaxis. *Trends in Neurosciences* **31**, 90-98 (2008).
3. Luster, A.D. Chemokines — Chemotactic Cytokines That Mediate Inflammation. *New England Journal of Medicine* **338**, 436-445 (1998).
4. Gillitzer, R. & Goebeler, M. Chemokines in cutaneous wound healing. *Journal of Leukocyte Biology* **69**, 513-521 (2001).
5. Muller, A. *et al.* Involvement of chemokine receptors in breast cancer metastasis. *Nature* **410**, 50-56 (2001).
6. Singh, M., Berkland, C. & Detamore, M.S. Strategies and Applications for Incorporating Physical and Chemical signal gradients in tissue engineering. *Tissue Engineering: Part B* **14**, 341-366 (2008).
7. Crimeen-Irwin, B., Scalzo, K., Gloster, S., Mottram, P.L. & Plebanski, M. Failure of Immune Homeostasis - The Consequences of Under and Over Reactivity. *Current Drug Targets - Immune, Endocrine & Metabolic Disorders* **5**, 413-423 (2005).
8. Kedrin, D., van Rheenen, J., Hernandez, L., Condeelis, J. & Segall, J. Cell Motility and Cytoskeletal Regulation in Invasion and Metastasis. *Journal of Mammary Gland Biology and Neoplasia* **12**, 143-152 (2007).
9. Ghigo, A., Damilano, F., Braccini, L. & Hirsch, E. PI3K inhibition in inflammation: Toward tailored therapies for specific diseases. *BioEssays* **32**, 185-196 (2010).
10. Parent, C.A. A Cell's Sense of Direction. *Science* **284**, 765-770 (1999).
11. Ridley, A.J. Cell Migration: Integrating Signals from Front to Back. *Science* **302**, 1704-1709 (2003).
12. Hoeller, O. & Kay, R.R. Chemotaxis in the Absence of PIP3 Gradients. *Current Biology* **17**, 813-817 (2007).
13. Ferguson, G.J. *et al.* PI(3)Kγ has an important context-dependent role in neutrophil chemokinesis. *Nature Cell Biology* **9**, 86-91 (2006).
14. Ward, S.G. Do phosphoinositide 3-kinases direct lymphocyte navigation? *Trends in Immunology* **25**, 67-74 (2004).
15. Chen, L. *et al.* PLA2 and PI3K/PTEN Pathways Act in Parallel to Mediate Chemotaxis. *Developmental Cell* **12**, 603-614 (2007).
16. Kamimura, Y. *et al.* PIP3-Independent Activation of TorC2 and PKB at the Cell's Leading Edge Mediates Chemotaxis. *Current Biology* **18**, 1034-1043 (2008).
17. Merriam-Webster, Vol. 2013 (Merriam-Webster.
18. Zhao, M. *et al.* Electrical signals control wound healing through phosphatidylinositol-3-OH kinase-[gamma] and PTEN. *Nature* **442**, 457-460 (2006).
19. Carter, S.B. Haptotaxis and the Mechanism of Cell Motility. *Nature* **213**, 256-260 (1967).
20. Petrie, R.J., Doyle, A.D. & Yamada, K.M. Random versus directionally persistent cell migration. *Nat Rev Mol Cell Biol* **10**, 538-549 (2009).

21. Hedgecock, E.M. & Russell, R.L. Normal and mutant thermotaxis in the nematode Caenorhabditis elegans. *Proceedings of the National Academy of Sciences* **72**, 4061-4065 (1975).
22. Kim, D.-H. *et al.* Mechanosensitivity of fibroblast cell shape and movement to anisotropic substratum topography gradients. *Biomaterials* **30**, 5433-5444 (2009).
23. Zigmond, S.H. Ability of polymorphonuclear leukocytes to orient in gradients of chemotactic factors. *The Journal of Cell Biology* **75**, 606-616 (1977).
24. Tozluoğlu, M. *et al.* Matrix geometry determines optimal cancer cell migration strategy and modulates response to interventions. *Nat Cell Biol* **15**, 751-762 (2013).
25. Petrie, R.J., Gavara, N., Chadwick, R.S. & Yamada, K.M. Nonpolarized signaling reveals two distinct modes of 3D cell migration. *The Journal of Cell Biology* **197**, 439-455 (2012).
26. Parent, C.A. & Devreotes, P.N. Molecular Genetics of Signal Transduction in Dictyostelium. *Annual Review of Biochemistry* **65**, 411-440 (1996).
27. Manahan, C.L., Iglesias, P.A., Long, Y. & Devreotes, P.N. CHEMOATTRACTANT SIGNALING IN DICTYOSTELIUM DISCOIDEUM. *Annual Review of Cell and Developmental Biology* **20**, 223-253 (2004).
28. Kolaczkowska, E. & Kubes, P. Neutrophil recruitment and function in health and inflammation. *Nat Rev Immunol* **13**, 159-175 (2013).
29. Luo, Y. & Dorf, M.E. Isolation of Mouse Neutrophils, in *Current Protocols in Immunology* (John Wiley & Sons, Inc., 2001).
30. Hauert, A.B., Martinelli, S., Marone, C. & Niggli, V. Differentiated HL-60 cells are a valid model system for the analysis of human neutrophil migration and chemotaxis. *The International Journal of Biochemistry & Cell Biology* **34**, 838-854 (2002).
31. Collins, S. The HL-60 promyelocytic leukemia cell line: proliferation, differentiation, and cellular oncogene expression. *Blood* **70**, 1233-1244 (1987).
32. Martin, P. Wound Healing--Aiming for Perfect Skin Regeneration. *Science* **276**, 75-81 (1997).
33. Seppä, H., Grotendorst, G., Seppä, S., Schiffmann, E. & Martin, G.R. Platelet-derived growth factor in chemotactic for fibroblasts. *The Journal of Cell Biology* **92**, 584-588 (1982).
34. Monypenny, J. *et al.* Cdc42 and Rac Family GTPases Regulate Mode and Speed but Not Direction of Primary Fibroblast Migration during Platelet-Derived Growth Factor-Dependent Chemotaxis. *Molecular and Cellular Biology* **29**, 2730-2747 (2009).
35. Haugh, J.M., Codazzi, F., Teruel, M. & Meyer, T. Spatial Sensing in Fibroblasts Mediated by 3' Phosphoinositides. *The Journal of Cell Biology* **151**, 1269-1280 (2000).
36. Schneider, I.C. & Haugh, J.M. Mechanisms of Gradient Sensing and Chemotaxis: Conserved Pathways, Diverse Regulation. *Cell Cycle* **5**, 1130-1134 (2006).
37. Wells, A., Grahovac, J., Wheeler, S., Ma, B. & Lauffenburger, D. Targeting tumor cell motility as a strategy against invasion and metastasis. *Trends in Pharmacological Sciences* **34**, 283-289 (2013).
38. Roussos, E.T., Condeelis, J.S. & Patsialou, A. Chemotaxis in cancer. *Nat Rev Cancer* **11**, 573-587 (2011).
39. Neri, A., Welch, D., Kawaguchi, T. & Nicolson, G.L. Development and Biologic Properties of Malignant Cell Sublines and Clones of a Spontaneously Metastasizing Rat Mammary Adenocarcinoma. *Journal of the National Cancer Institute* **68**, 507-517 (1982).
40. Segall, J. *et al.* EGF stimulates lamellipod extension in metastatic mammary adenocarcinoma cells by an actin-dependent mechanism. *Clin Exp Metast* **14**, 61-72 (1996).

41. Friedl, P., Locker, J., Sahai, E. & Segall, J.E. Classifying collective cancer cell invasion. *Nat Cell Biol* **14**, 777-783 (2012).
42. Ridley, A.J. *et al.* Cell Migration: Integrating Signals from Front to Back. *Science* **302**, 1704-1709 (2003).
43. Montell, D.J. Border-cell migration: the race is on. *Nat Rev Mol Cell Biol* **4**, 13-24 (2003).
44. Haas, P. & Gilmour, D. Chemokine signaling mediates self-organizing tissue migration in the zebrafish lateral line. *Developmental Cell* **10**, 673-680 (2006).
45. Theveneau, E. & Mayor, R. Neural crest delamination and migration: From epithelium-to-mesenchyme transition to collective cell migration. *Developmental Biology* **366**, 34-54 (2012).
46. Ewald, A.J. Isolation of Mouse Mammary Organoids for Long-Term Time-Lapse Imaging. *Cold Spring Harbor Protocols* **2013**, pdb.prot072892 (2013).
47. Nguyen-Ngoc, K.-V. *et al.* ECM microenvironment regulates collective migration and local dissemination in normal and malignant mammary epithelium. *Proceedings of the National Academy of Sciences* **109**, E2595–E2604 (2012).
48. Abercrombie, M. & Heaysman, J.E.M. Observations on the social behaviour of cells in tissue culture: II. "Monolayering" of fibroblasts. *Experimental Cell Research* **6**, 293-306 (1954).
49. Abercrombie, M. Contact Inhibition in Tissue Culture. *In Vitro* **6**, 128-142 (1970).
50. Batson, J., Astin, J.W. & Nobes, C.D. Regulation of contact inhibition of locomotion by Eph–ephrin signalling. *Journal of Microscopy* **251**, 232-241 (2013).
51. Paddock, S.W. & Dunn, G.A. Analysing collisions between fibroblasts and fibrosarcoma cells: fibrosarcoma cells show an active invasionary response. *Journal of Cell Science* **81**, 163-187 (1986).
52. Astin, J.W. *et al.* Competition amongst Eph receptors regulates contact inhibition of locomotion and invasiveness in prostate cancer cells. *Nat Cell Biol* **12**, 1194-1204 (2010).
53. Xiao, Z., Zhang, N., Murphy, D.B. & Devreotes, P.N. Dynamic Distribution of Chemoattractant Receptors in Living Cells During Chemotaxis and Persistent Stimulation. *The Journal of Cell Biology* **139**, 365-374 (1997).
54. Bailly, M. *et al.* Epidermal Growth Factor Receptor Distribution during Chemotactic Responses. *Molecular Biology of the Cell* **11**, 3873-3883 (2000).
55. Servant, G., Weiner, O.D., Neptune, E.R., Sedat, J.W. & Bourne, H.R. Dynamics of a Chemoattractant Receptor in Living Neutrophils during Chemotaxis. *Molecular Biology of the Cell* **10**, 1163-1178 (1999).
56. Parent, C.A., Blacklock, B.J., Froehlich, W.M., Murphy, D.B. & Devreotes, P.N. G Protein Signaling Events Are Activated at the Leading Edge of Chemotactic Cells. *Cell* **95**, 81-91 (1998).
57. Servant, G. *et al.* Polarization of Chemoattractant Receptor Signaling During Neutrophil Chemotaxis. *Science* **287**, 1037-1040 (2000).
58. Iijima, M. & Devreotes, P. Tumor Suppressor PTEN Mediates Sensing of Chemoattractant Gradients. *Cell* **109**, 599-610 (2002).
59. Hall, A. Rho GTPases and the Actin Cytoskeleton. *Science* **279**, 509-514 (1998).
60. Ridley, A.J. & Hall, A. The small GTP-binding protein rho regulates the assembly of focal adhesions and actin stress fibers in response to growth factors. *Cell* **70**, 389-399 (1992).
61. Ridley, A.J., Paterson, H.F., Johnston, C.L., Diekmann, D. & Hall, A. The small GTP-binding protein rac regulates growth factor-induced membrane ruffling. *Cell* **70**, 401-410 (1992).

62. Nobes, C.D. & Hall, A. Rho, Rac, and Cdc42 GTPases regulate the assembly of multimolecular focal complexes associated with actin stress fibers, lamellipodia, and filopodia. *Cell* **81**, 53-62 (1995).
63. Kraynov, V.S. Localized Rac Activation Dynamics Visualized in Living Cells. *Science* **290**, 333-337 (2000).
64. Pertz, O., Hodgson, L., Klemke, R.L. & Hahn, K.M. Spatiotemporal dynamics of RhoA activity in migrating cells. *Nature* **440**, 1069-1072 (2006).
65. Nalbant, P. Activation of Endogenous Cdc42 Visualized in Living Cells. *Science* **305**, 1615-1619 (2004).
66. Wong, K., Pertz, O., Hahn, K. & Bourne, H. Neutrophil polarization: Spatiotemporal dynamics of RhoA activity support a self-organizing mechanism. *Proceedings of the National Academy of Sciences of the United States of America* **103**, 3639-3644 (2006).
67. Andrew, N. & Insall, R.H. Chemotaxis in shallow gradients is mediated independently of PtdIns 3-kinase by biased choices between random protrusions. *Nat Cell Biol* **9**, 193-200 (2007).
68. Devreotes, P.N. & Zigmond, S.H. Chemotaxis in Eukaryotic Cells: A Focus on Leukocytes and Dictyostelium. *Annual Review of Cell Biology* **4**, 649-686 (1988).
69. Tinevez, J.-Y. *et al.* Role of cortical tension in bleb growth. *Proceedings of the National Academy of Sciences* (2009).
70. Takenawa, T. & Miki, H. WASP and WAVE family proteins: key molecules for rapid rearrangement of cortical actin filaments and cell movement. *Journal of Cell Science* **114**, 1801-1809 (2001).
71. Krugmann, S. *et al.* Cdc42 induces filopodia by promoting the formation of an IRSp53:Mena complex. *Current Biology* **11**, 1645-1655 (2001).
72. Fackler, O.T. & Grosse, R. Cell motility through plasma membrane blebbing. *The Journal of Cell Biology* **181**, 879-884 (2008).
73. Higashida, C. *et al.* Actin Polymerization-Driven Molecular Movement of mDia1 in Living Cells. *Science* **303**, 2007-2010 (2004).
74. Webb, D.J., Parsons, J.T. & Horwitz, A.F. Adhesion assembly, disassembly and turnover in migrating cells - over and over and over again. *Nat Cell Biol* **4**, E97-E100 (2002).
75. Desgrosellier, J.S. & Cheresh, D.A. Integrins in cancer: biological implications and therapeutic opportunities. *Nat Rev Cancer* **10**, 9-22 (2010).
76. Huttenlocher, A. & Horwitz, A.R. Integrins in Cell Migration. *Cold Spring Harbor Perspectives in Biology* **3** (2011).
77. Zigmond, S.H., Foxman, E.F. & Segall, J.E. Chemotaxis Assays for Eukaryotic Cells, in *Current Protocols in Cell Biology* (John Wiley & Sons, Inc., 2001).
78. Parent, C.A., Blacklock, B.J., Froehlich, W.M., Murphy, D.B. & Devreotes, P.N. G protein Signaling Events Are Activated at the Leading Edge of Chemotactic Cells. *Cell* **95**, 81-91 (1998).
79. Bailly, M., Yan, L., Whitesides, G.M., Condeelis, J.S. & Segall, J.E. Regulation of Protrusion Shape and Adhesion to the Substratum during Chemotactic Responses of Mammalian Carcinoma Cells. *Experimental Cell Research* **241**, 285-299 (1998).
80. Keenan, T.M. & Folch, A. Biomolecular gradients in cell culture systems. *Lab on a Chip* **8**, 34-57 (2008).
81. Boyden, S. THE CHEMOTACTIC EFFECT OF MIXTURES OF ANTIBODY AND ANTIGEN ON POLYMORPHONUCLEAR LEUCOCYTES. *The Journal of Experimental Medicine* **115**, 453-466 (1962).

82. Zicha, D., Dunn, G.A. & Brown, A.F. A new direct-viewing chemotaxis chamber. *Journal of Cell Science* **99**, 769-775 (1991).
83. Muinonen-Martin, A.J., Veltman, D.M., Kalna, G. & Insall, R.H. An Improved Chamber for Direct Visualisation of Chemotaxis. *PLoS ONE* **5**, e15309 (2010).
84. Heit, B., Tavener, S., Raharjo, E. & Kubes, P. An intracellular signaling hierarchy determines direction of migration in opposing chemotactic gradients. *The Journal of Cell Biology* **159**, 91-102 (2002).
85. Li Jeon, N. *et al.* Neutrophil chemotaxis in linear and complex gradients of interleukin-8 formed in a microfabricated device. *Nature Biotechnology* (2002).
86. Effenhauser, C.S., Bruin, G.J.M., Paulus, A. & Ehrat, M. Integrated Capillary Electrophoresis on Flexible Silicone Microdevices: Analysis of DNA Restriction Fragments and Detection of Single DNA Molecules on Microchips. *Analytical Chemistry* **69**, 3451-3457 (1997).
87. Kopp, M.U., Mello, A.J.d. & Manz, A. Chemical Amplification: Continuous-Flow PCR on a Chip. *Science* **280**, 1046-1048 (1998).
88. McEnery, M. *et al.* Liquid chromatography on-chip: progression towards a [small mu]-total analysis system. *Analyst* **125** (2000).
89. Fu, A.Y., Spence, C., Scherer, A., Arnold, F.H. & Quake, S.R. A microfabricated fluorescence-activated cell sorter. *Nat Biotech* **17**, 1109-1111 (1999).
90. McDonald, J.C. *et al.* Fabrication of microfluidic systems in poly(dimethylsiloxane). *ELECTROPHORESIS* **21**, 27-40 (2000).
91. Xia, Y. & Whitesides, G.M. Soft Lithography. *Angewandte Chemie International Edition* **37**, 550-575 (1998).
92. Weibel, D.B. & Whitesides, G.M. Applications of microfluidics in chemical biology. *Current Opinion in Chemical Biology* **10**, 584-591 (2006).
93. Hung, P.J., Lee, P.J., Sabounchi, P., Lin, R. & Lee, L.P. Continuous perfusion microfluidic cell culture array for high-throughput cell-based assays. *Biotechnology and Bioengineering* **89**, 1-8 (2005).
94. Beebe, D.J., Mensing, G.A. & Walker, G.M. PHYSICS AND APPLICATIONS OF MICROFLUIDICS IN BIOLOGY. *Annual Review of Biomedical Engineering* **4**, 261-286 (2002).
95. Folch, A., Jo, B.-H., Hurtado, O., Beebe, D.J. & Toner, M. Microfabricated elastomeric stencils for micropatterning cell cultures. *Journal of Biomedical Materials Research* **52**, 346-353 (2000).
96. Stine, M.J. *et al.* Integration of Genotypic and Phenotypic Screening Reveals Molecular Mediators of Melanoma–Stromal Interaction. *Cancer Research* **71**, 2433-2444 (2011).
97. Folch, A. & Toner, M. Cellular Micropatterns on Biocompatible Materials. *Biotechnology Progress* **14**, 388-392 (1998).
98. Takayama, S. *et al.* Patterning cells and their environments using multiple laminar fluid flows in capillary networks. *Proceedings of the National Academy of Sciences* **96**, 5545-5548 (1999).
99. Park, J. *et al.* Simple haptotactic gradient generation within a triangular microfluidic channel. *Lab on a Chip* **10**, 2130-2138 (2010).
100. Cheong, R., Wang, C.J. & Levchenko, A. High Content Cell Screening in a Microfluidic Device. *Molecular & Cellular Proteomics* **8**, 433-442 (2009).
101. Cheong, R., Wang, C.J. & Levchenko, A. Using a Microfluidic Device for High-Content Analysis of Cell Signaling. *Sci. Signal.* **2**, pl2- (2009).

102. Fosbrink, M., Aye-Han, N.-N., Cheong, R., Levchenko, A. & Zhang, J. Visualization of JNK activity dynamics with a genetically encoded fluorescent biosensor. *Proceedings of the National Academy of Sciences* **107**, 5459-5464 (2010).
103. Kaneda, A. *et al.* Enhanced sensitivity to IGF-II signaling links loss of imprinting of IGF2 to increased cell proliferation and tumor risk. *Proceedings of the National Academy of Sciences* **104**, 20926-20931 (2007).
104. Gómez-Sjöberg, R., Leyrat, A.A., Pirone, D.M., Chen, C.S. & Quake, S.R. Versatile, Fully Automated, Microfluidic Cell Culture System. *Analytical Chemistry* **79**, 8557-8563 (2007).
105. Tay, S. *et al.* Single-cell NF-[kgr]B dynamics reveal digital activation and analogue information processing. *Nature* **466**, 267-271 (2010).
106. Taylor, R.J. *et al.* Dynamic analysis of MAPK signaling using a high-throughput microfluidic single-cell imaging platform. *Proceedings of the National Academy of Sciences* **106**, 3758-3763 (2009).
107. Balaban, N.Q., Merrin, J., Chait, R., Kowalik, L. & Leibler, S. Bacterial Persistence as a Phenotypic Switch. *Science* **305**, 1622-1625 (2004).
108. Groisman, A. *et al.* A microfluidic chemostat for experiments with bacterial and yeast cells. *Nat Meth* **2**, 685-689 (2005).
109. Cho, H. *et al.* Self-Organization in High-Density Bacterial Colonies: Efficient Crowd Control. *PLoS Biol* **5**, e302 (2007).
110. Chen, C.S., Mrksich, M., Huang, S., Whitesides, G.M. & Ingber, D.E. Geometric Control of Cell Life and Death. *Science* **276**, 1425-1428 (1997).
111. Carlo, D.D., Wu, L.Y. & Lee, L.P. Dynamic single cell culture array. *Lab on a Chip* **6** (2006).
112. Skelley, A.M., Kirak, O., Suh, H., Jaenisch, R. & Voldman, J. Microfluidic control of cell pairing and fusion. *Nat Meth* **6**, 147-152 (2009).
113. Ryley, J. & Pereira-Smith, O.M. Microfluidics device for single cell gene expression analysis in Saccharomyces cerevisiae. *Yeast* **23**, 1065-1073 (2006).
114. Yun, K.-S. & Yoon, E. Micro/Nanofluidic Device for Single-Cell-Based Assay. *Biomedical Microdevices* **7**, 35-40 (2005).
115. Wheeler, A.R. *et al.* Microfluidic Device for Single-Cell Analysis. *Analytical Chemistry* **75**, 3581-3586 (2003).
116. Unger, M.A., Chou, H.-P., Thorsen, T., Scherer, A. & Quake, S.R. Monolithic Microfabricated Valves and Pumps by Multilayer Soft Lithography. *Science* **288**, 113-116 (2000).
117. Cai, L., Friedman, N. & Xie, X.S. Stochastic protein expression in individual cells at the single molecule level. *Nature* **440**, 358-362 (2006).
118. Yin, Z., Noren, D., Wang, C.J., Hang, R. & Levchenko, A. Analysis of pairwise cell interactions using an integrated dielectrophoretic-microfluidic system. *Mol Syst Biol* **4** (2008).
119. Wang, C.J., Bergmann, A., Lin, B., Kim, K. & Levchenko, A. Diverse Sensitivity Thresholds in Dynamic Signaling Responses by Social Amoebae. *Sci. Signal.* **5**, ra17- (2012).
120. Lipan, O. & Wong, W.H. The use of oscillatory signals in the study of genetic networks. *Proceedings of the National Academy of Sciences of the United States of America* **102**, 7063-7068 (2005).
121. Paliwal, S., Wang, C.J. & Levchenko, A. Pulsing cells: How fast is too fast? *HFSP Journal* **2**, 251-256 (2008).
122. Mettetal, J.T., Muzzey, D., Gómez-Uribe, C. & van Oudenaarden, A. The Frequency Dependence of Osmo-Adaptation in Saccharomyces cerevisiae. *Science* **319**, 482-484 (2008).

123. Hersen, P., McClean, M.N., Mahadevan, L. & Ramanathan, S. Signal processing by the HOG MAP kinase pathway. *Proceedings of the National Academy of Sciences* **105**, 7165-7170 (2008).
124. Bennett, M.R. *et al.* Metabolic gene regulation in a dynamically changing environment. *Nature* **454**, 1119-1122 (2008).
125. Jeon, N.L. *et al.* Generation of Solution and Surface Gradients Using Microfluidic Systems. *Langmuir* **16**, 8311-8316 (2000).
126. Dertinger, S.K.W., Chiu, D.T., Jeon, N.L. & Whitesides, G.M. Generation of Gradients Having Complex Shapes Using Microfluidic Networks. *Analytical Chemistry* **73**, 1240-1246 (2001).
127. Li Jeon, N. *et al.* Neutrophil chemotaxis in linear and complex gradients of interleukin-8 formed in a microfabricated device. *Nat Biotech* **20**, 826-830 (2002).
128. Herzmark, P. *et al.* Bound attractant at the leading vs. the trailing edge determines chemotactic prowess. *Proceedings of the National Academy of Sciences* **104**, 13349-13354 (2007).
129. Irimia, D. *et al.* Microfluidic system for measuring neutrophil migratory responses to fast switches of chemical gradients. *Lab on a Chip* **6** (2006).
130. Lin, F. *et al.* Neutrophil Migration in Opposing Chemoattractant Gradients Using Microfluidic Chemotaxis Devices. *Annals of Biomedical Engineering* **33**, 475-482 (2005).
131. Campbell, K. & Groisman, A. Generation of complex concentration profiles in microchannels in a logarithmically small number of steps. *Lab on a Chip* **7** (2007).
132. Thompson, D.M. *et al.* Dynamic Gene Expression Profiling Using a Microfabricated Living Cell Array. *Analytical Chemistry* **76**, 4098-4103 (2004).
133. Paliwal, S. *et al.* MAPK-mediated bimodal gene expression and adaptive gradient sensing in yeast. *Nature* **446**, 46-51 (2007).
134. Hao, N. *et al.* Regulation of Cell Signaling Dynamics by the Protein Kinase-Scaffold Ste5. *Molecular Cell* **30**, 649-656 (2008).
135. Skoge, M. *et al.* Gradient sensing in defined chemotactic fields. *Integrative Biology* **2** (2010).
136. Irimia, D., Charras, G., Agrawal, N., Mitchison, T. & Toner, M. Polar stimulation and constrained cell migration in microfluidic channels. *Lab on a Chip* **7** (2007).
137. Takayama, S. *et al.* Laminar flows: Subcellular positioning of small molecules. *Nature* **411**, 1016-1016 (2001).
138. Sawano, A., Takayama, S., Matsuda, M. & Miyawaki, A. Lateral Propagation of EGF Signaling after Local Stimulation Is Dependent on Receptor Density. *Developmental Cell* **3**, 245-257 (2002).
139. Kretzmer, G. & Schügerl, K. Response of mammalian cells to shear stress. *Appl Microbiol Biotechnol* **34**, 613-616 (1991).
140. Irimia, D., Charras, G., Agrawal, N., Mitchison, T. & Toner, M. Polar stimulation and constrained cell migration in microfluidic channels. *Lab on a Chip* **7**, 1783 (2007).
141. Lin, B. *et al.* Synthetic spatially graded Rac activation drives cell polarization and movement. *Proceedings of the National Academy of Sciences* **109**, E3668–E3677 (2012).
142. Servant, G. *et al.* Polarization of Chemoattractant Receptor Signaling During Neutrophil Chemotaxis. *Science* **287**, 1037-1040 (2000).
143. Weiner, O.D. *et al.* A PtdInsP3- and Rho GTPase-mediated positive feedback loop regulates neutrophil polarity. *Nature Cell Biology* **4**, 509-513 (2002).
144. Sasaki, A.T. *et al.* G protein-independent Ras/PI3K/F-actin circuit regulates basic cell motility. *The Journal of Cell Biology* **178**, 185-191 (2007).

145. Inoue, T. & Meyer, T. Synthetic Activation of Endogenous PI3K and Rac Identifies an AND-Gate Switch for Cell Polarization and Migration. *PLoS ONE* **3**, e3068 (2008).
146. Niggli, V. A membrane-permeant ester of phosphatidylinositol 3,4,5-triphosphate (PIP_3) is an activator of human neutrophil migration. *FEBS Letters* **473**, 217-221 (2000).
147. Iijima, M. & Devreotes, P.N. Tumor Suppressor PTEN mediates sensing of chemoattracting gradients. *Cell* **109**, 599-610 (2002).
148. Wu, Y.I. *et al.* A genetically encoded photoactivatable Rac controls the motility of living cells. *Nature* **461**, 104-108 (2009).
149. Wang, X., He, L., Wu, Y.I., Hahn, K.M. & Montell, D.J. Light-mediated activation reveals a key role for Rac in collective guidance of cell movement in vivo. *Nature Cell Biology* **12**, 591-597 (2010).
150. Yoo, S.K. *et al.* Differential Regulation of Protrusion and Polarity by PI(3)K during Neutrophil Motility in Live Zebrafish. *Developmental Cell* **18**, 226-236 (2010).
151. Levskaya, A., Weiner, O.D., Lim, W.A. & Voigt, C.A. Spatiotemporal control of cell signalling using a light-switchable protein interaction. *Nature* **461**, 997-1001 (2009).
152. Umeda, N., Ueno, T., Pohlmeyer, C., Nagano, T. & Inoue, T. A Photocleavable Rapamycin Conjugate for Spatiotemporal Control of Small GTPase Activity. *Journal of the American Chemical Society* **133**, 12-14 (2010).
153. Yazawa, M., Sadaghiani, A.M., Hsueh, B. & Dolmetsch, R.E. Induction of protein-protein interactions in live cells using light. *Nature Biotechnology* **27**, 941-945 (2009).
154. Ghosh, M. *et al.* Cofilin Promotes Actin Polymerization and Defines the Direction of Cell Motility. *Science* **304**, 743-746 (2004).
155. Roy, P. *et al.* Local Photorelease of Caged Thymosin Β4 in Locomoting Keratocytes Causes Cell Turning. *The Journal of Cell Biology* **153**, 1035-1047 (2001).
156. Zheng, J.Q. Turning of nerve growth cones induced by localized increases in intracellular calcium ions. *Nature* **403**, 89-93 (2000).
157. Inoue, T., Heo, W.D., Grimley, J.S., Wandless, T.J. & Meyer, T. An inducible translocation strategy to rapidly activate and inhibit small GTPase signaling pathways. *Nature Methods* **2**, 415-418 (2005).
158. Rivera, V.M. *et al.* A humanized system for pharmacological control of gene expression. *Nature Medicine* **2**, 1028-1032 (1996).
159. Carlo, D.D., Wu, L.Y. & Lee, L.P. Dynamic single cell culture array. *Lab on a Chip* **6**, 1445 (2006).
160. Yin, Z., Noren, D., Wang, C.J., Hang, R. & Levchenko, A. Analysis of pairwise cell interactions using an integrated dielectrophoretic-microfluidic system. *Molecular Systems Biology* **4** (2008).
161. Faure-Andre, G. *et al.* Regulation of Dendritic Cell Migration by CD74 the MHC Class II-Associated Invariant Chain. *Science* **322**, 1705-1709 (2008).
162. Banaszynski, L.A., Liu, C.W. & Wandless, T.J. Characterization of the FKBP·Rapamycin·FRB Ternary Complex. *Journal of the American Chemical Society* **127**, 4715-4721 (2005).
163. McMahon, L.P., Choi, K.M., Lin, T.A., Abraham, R.T. & Lawrence, J.C. The Rapamycin-Binding Domain Governs Substrate Selectivity by the Mammalian Target of Rapamycin. *Molecular and Cellular Biology* **22**, 7428-7438 (2002).
164. Wyckoff, J.B., Segall, J.E. & Condeelis, J.S. The Collection of the Motile Population of Cells from a Living Tumor. *Cancer Research* **60**, 5401-5404 (2000).

165. Inoue, T., Heo, W.D., Grimley, J.S., Wandless, T.J. & Meyer, T. An inducible translocation strategy to rapidly activate and inhibit small GTPase signaling pathways. *Nat Meth* **2**, 415-418 (2005).
166. Itoh, R.E. *et al.* Activation of Rac and Cdc42 Video Imaged by Fluorescent Resonance Energy Transfer-Based Single-Molecule Probes in the Membrane of Living Cells. *Molecular and Cellular Biology* **22**, 6582-6591 (2002).
167. Dawes, A.T. & Edelstein-Keshet, L. Phosphoinositides and Rho Proteins Spatially Regulate Actin Polymerization to Initiate and Maintain Directed Movement in a One-Dimensional Model of a Motile Cell. *Biophysical Journal* **92**, 744-768 (2007).
168. Marée, A.F.M., Grieneisen, V.A. & Edelstein-Keshet, L. How Cells Integrate Complex Stimuli: The Effect of Feedback from Phosphoinositides and Cell Shape on Cell Polarization and Motility. *PLoS Comput Biol* **8**, e1002402 (2012).
169. Aoki, K., Nakamura, T., Inoue, T., Meyer, T. & Matsuda, M. An essential role for the SHIP2-dependent negative feedback loop in neuritogenesis of nerve growth factor-stimulated PC12 cells. *The Journal of Cell Biology* **177**, 817-827 (2007).
170. Stephens, L., Milne, L. & Hawkins, P. Moving towards a Better Understanding of Chemotaxis. *Current Biology* **18**, R485-R494 (2008).
171. Janetopoulos, C. Chemoattractant-induced phosphatidylinositol 3,4,5-trisphosphate accumulation is spatially amplified and adapts, independent of the actin cytoskeleton. *Proceedings of the National Academy of Sciences* **101**, 8951-8956 (2004).
172. Worthylake, D.K., Rossman, K.L. & Sondek, J. Crystal structure of Rac1 in complex with the guanine nucleotide exchange region of Tiam1. *Nature* **408**, 682-688 (2000).
173. Gardiner, E.M. *et al.* Spatial and Temporal Analysis of Rac Activation during Live Neutrophil Chemotaxis. *Current Biology* **12**, 2029-2034 (2002).
174. Irimia, D. *et al.* Microfluidic system for measuring neutrophil migratory responses to fast switches of chemical gradients. *Lab on a Chip* **6**, 191-198 (2006).
175. Meier, B. *et al.* Chemotactic cell trapping in controlled alternating gradient fields. *Proceedings of the National Academy of Sciences* (2011).
176. Suh, B.-C., Inoue, T., Meyer, T. & Hille, B. Rapid Chemically Induced Changes of PtdIns(4,5)P2 Gate KCNQ Ion Channels. *Science* **314**, 1454-1457 (2006).
177. Fegan, A., White, B., Carlson, J.C.T. & Wagner, C.R. Chemically Controlled Protein Assembly: Techniques and Applications. *Chemical Reviews* **110**, 3315-3336 (2010).
178. Bishop, A.C. *et al.* A chemical switch for inhibitor-sensitive alleles of any protein kinase. *Nature* **407**, 395-401 (2000).
179. Qiao, Y., Molina, H., Pandey, A., Zhang, J. & Cole, P.A. Chemical Rescue of a Mutant Enzyme in Living Cells. *Science* **311**, 1293-1297 (2006).
180. Joanne Wang, C. *et al.* A microfluidics-based turning assay reveals complex growth cone responses to integrated gradients of substrate-bound ECM molecules and diffusible guidance cues. *Lab on a Chip* **8**, 227-237 (2008).
181. Hodgson, L., Shen, F. & Hahn, K. Biosensors for Characterizing the Dynamics of Rho Family GTPases in Living Cells, in *Current Protocols in Cell Biology* (John Wiley & Sons, Inc., 2001).
182. Guizar-Sicairos, M., Thurman, S.T. & Fienup, J.R. Efficient subpixel image registration algorithms. *Opt. Lett.* **33**, 156-158 (2008).
183. Holmes, W.R., Lin, B., Levchenko, A. & Edelstein-Keshet, L. Modelling Cell Polarization Driven by Synthetic Spatially Graded Rac Activation. *PLoS Comput Biol* **8**, e1002366 (2012).

184. Jilkine, A., Marée, A. & Edelstein-Keshet, L. Mathematical Model for Spatial Segregation of the Rho-Family GTPases Based on Inhibitory Crosstalk. *Bulletin of Mathematical Biology* **69**, 1943-1978 (2007).
185. Marée, A.M., Jilkine, A., Dawes, A., Grieneisen, V. & Edelstein-Keshet, L. Polarization and Movement of Keratocytes: A Multiscale Modelling Approach. *Bulletin of Mathematical Biology* **68**, 1169-1211 (2006).
186. Mori, Y., Jilkine, A. & Edelstein-Keshet, L. Wave-Pinning and Cell Polarity from a Bistable Reaction-Diffusion System. *Biophysical Journal* **94**, 3684-3697 (2008).
187. Jilkine, A. & Edelstein-Keshet, L. A Comparison of Mathematical Models for Polarization of Single Eukaryotic Cells in Response to Guided Cues. *PLoS Comput Biol* **7**, e1001121 (2011).
188. Schmitt, A.M. *et al.* Wnt-Ryk signalling mediates medial-lateral retinotectal topographic mapping. *Nature* **439**, 31-37 (2006).
189. Carmona-Fontaine, C. *et al.* Contact inhibition of locomotion in vivo controls neural crest directional migration. *Nature* **456**, 957-961 (2008).
190. Theveneau, E. *et al.* Collective Chemotaxis Requires Contact-Dependent Cell Polarity. *Developmental Cell* **19**, 39-53 (2010).
191. Wang, W. *et al.* Single Cell Behavior in Metastatic Primary Mammary Tumors Correlated with Gene Expression Patterns Revealed by Molecular Profiling. *Cancer Research* **62**, 6278-6288 (2002).
192. Wyckoff, J.B., Jones, J.G., Condeelis, J.S. & Segall, J.E. A Critical Step in Metastasis: In Vivo Analysis of Intravasation at the Primary Tumor. *Cancer Research* **60**, 2504-2511 (2000).
193. Abercrombie, M. & Heaysman, J.E.M. Observations on the social behaviour of cells in tissue culture: I. Speed of movement of chick heart fibroblasts in relation to their mutual contacts. *Experimental Cell Research* **5**, 111-131 (1953).
194. Mayor, R. & Carmona-Fontaine, C. Keeping in touch with contact inhibition of locomotion. *Trends in Cell Biology* **20**, 319-328 (2010).
195. Abercrombie, M. Contact inhibition and malignancy. *Nature* **281**, 259-262 (1979).
196. Xue, C. *et al.* Epidermal Growth Factor Receptor Overexpression Results in Increased Tumor Cell Motility In vivo Coordinately with Enhanced Intravasation and Metastasis. *Cancer Research* **66**, 192-197 (2006).
197. Sharma, V.P. *et al.* Reconstitution of in vivo macrophage-tumor cell pairing and streaming motility on one-dimensional micro-patterned substrates. *IntraVital* **1**, 77-85 (2012).
198. Park, K.C. *et al.* Rac regulation of chemotaxis and morphogenesis in Dictyostelium. *EMBO J* **23**, 4177-4189 (2004).
199. Kraynov, V.S. *et al.* Localized Rac Activation Dynamics Visualized in Living Cells. *Science* **290**, 333-337 (2000).
200. Yip, S.-C. *et al.* Quantification of PtdIns(3,4,5)P3 dynamics in EGF-stimulated carcinoma cells: a comparison of PH-domain-mediated methods with immunological methods. *Biochem J* **411**, 441-448 (2008).
201. Yip, S.-C. *et al.* The distinct roles of Ras and Rac in PI 3-kinase-dependent protrusion during EGF-stimulated cell migration. *Journal of Cell Science* **120**, 3138-3146 (2007).
202. Sidani, M. *et al.* Cofilin determines the migration behavior and turning frequency of metastatic cancer cells. *The Journal of Cell Biology* **179**, 777-791 (2007).
203. Abercrombie, M. & Heaysman, J.E.M. Invasiveness of Sarcoma Cells. *Nature* **174**, 697-698 (1954).

204. Huttenlocher, A. *et al.* Integrin and Cadherin Synergy Regulates Contact Inhibition of Migration and Motile Activity. *The Journal of Cell Biology* **141**, 515-526 (1998).
205. Orioli, D. & Klein, R. The eph receptor family:axonal guidance by contact repulsion. *Trends in Genetics* **13**, 354-359 (1997).
206. Oike, Y. *et al.* Regulation of vasculogenesis and angiogenesis by EphB/ephrin-B2 signaling between endothelial cells and surrounding mesenchymal cells. *Blood* **100**, 1326-1333 (2002).
207. Pasquale, E.B. Eph receptors and ephrins in cancer: bidirectional signalling and beyond. *Nat Rev Cancer* **10**, 165-180 (2010).
208. Pasquale, E.B. Eph receptor signalling casts a wide net on cell behaviour. *Nat Rev Mol Cell Biol* **6**, 462-475 (2005).
209. Dail, M., Richter, M., Godement, P. & Pasquale, E.B. Eph receptors inactivate R-Ras through different mechanisms to achieve cell repulsion. *Journal of Cell Science* **119**, 1244-1254 (2006).
210. Yamashita, S. *et al.* CalDAG-GEFIII Activation of Ras, R-Ras, and Rap1. *Journal of Biological Chemistry* **275**, 25488-25493 (2000).
211. Rodriguez-Viciana, P., Sabatier, C. & McCormick, F. Signaling Specificity by Ras Family GTPases Is Determined by the Full Spectrum of Effectors They Regulate. *Molecular and Cellular Biology* **24**, 4943-4954 (2004).
212. Marston, D.J., Dickinson, S. & Nobes, C.D. Rac-dependent trans-endocytosis of ephrinBs regulates Eph-ephrin contact repulsion. *Nat Cell Biol* **5**, 879-888 (2003).
213. Zimmer, M., Palmer, A., Kohler, J. & Klein, R. EphB-ephrinB bi-directional endocytosis terminates adhesion allowing contact mediated repulsion. *Nat Cell Biol* **5**, 869-878 (2003).
214. Matthews, H.K. *et al.* Directional migration of neural crest cells in vivo is regulated by Syndecan-4/Rac1 and non-canonical Wnt signaling/RhoA. *Development* **135**, 1771-1780 (2008).
215. Villar-Cerviño, V. *et al.* Contact Repulsion Controls the Dispersion and Final Distribution of Cajal-Retzius Cells. *Neuron* **77**, 457-471 (2013).
216. Davis, J.R. *et al.* Emergence of embryonic pattern through contact inhibition of locomotion. *Development* **139**, 4555-4560 (2012).
217. Lin, Y.-C. *et al.* Rapidly Reversible Manipulation of Molecular Activity with Dual Chemical Dimerizers. *Angewandte Chemie International Edition* **52**, 6450-6454 (2013).
218. Weber, M. *et al.* Interstitial Dendritic Cell Guidance by Haptotactic Chemokine Gradients. *Science* **339**, 328-332 (2013).
219. Goswami, S. *et al.* Macrophages Promote the Invasion of Breast Carcinoma Cells via a Colony-Stimulating Factor-1/Epidermal Growth Factor Paracrine Loop. *Cancer Research* **65**, 5278-5283 (2005).

Curriculum Vitae

Education

Ph.D. **Johns Hopkins University,** Baltimore, MD 2013
Department of Biomedical Engineering
Advisors: Dr. Andre Levchenko, Dr. Takanari Inoue

B.S. **Johns Hopkins University,** Baltimore, MD 2007
Department of Biomedical Engineering

Other Professional Experience

Research Assistant 2007
Advisor- Dr. Jef Boeke
Department of Molecular Biology and Genetics, JHU, Baltimore, MD

Research Assistant 2006—2007
Advisor- Dr. Andre Levchenko
Department of Biomedical Engineering, JHU, Baltimore, MD

Awards & Honors

Paul Ehrlich Young Investigator Award	2013
Provost Undergraduate Research Award	2007
Chubb United States Scholarship	2003-2007
Edward J. Bloustein Distinguished Scholar	2003

Peer Reviewed Publications

Lin, B., Holmes, W. R., Wang, C. J., Ueno, T., Harwell, A., Edelstein-Keshet, L., Inoue, T.*, Levchenko, A.*, 2012. Synthetic spatially graded Rac activation drives cell polarization and movement. *Proceedings of the National Academy of Sciences*. 09(52):E3668–E3677.

Lin, Y-C., Niewadomski, P.*, **Lin, B.***, Nakamura, H.*, Phua, SC., Jiao, J., Levchenko, A., Inoue, T., Rohatgi, R., Inoue, T. 2013. Chemically - inducible diffusion trap at cilia (C-IDTc) reveals molecular sieve-like barrier. *Nature Chemical Biology*. 9(7):437-443.

Holmes, W. R., **Lin, B.**, Levchenko, A., Edelstein-Keshet, L., 2012. Modelling Cell Polarization Driven by Synthetic Spatially Graded Rac Activation. *PLoS Computational Biology*. 8(6):e1002366.

Wang, C. J.*, Bergmann, A.*, **Lin, B.**, Kim, K., Levchenko, A. 2012. Diverse Sensitivity Thresholds in Dynamic Signaling Responses by Social Amoebae. *Science Signaling*. 5(213):ra17.

Wang, C. J.*, Li, X.*, **Lin, B.**, Shim, S., Ming, G.-l., Levchenko, A., 2008. A microfluidics-based turning assay reveals complex growth cone responses to integrated gradients of substrate-bound ECM molecules and diffusible guidance cues. *Lab on a Chip*. 8(2):227-237.

Review Articles

Lin, B., Levchenko, A., 2012. Microfluidic technologies for studying synthetic circuits. *Current Opinion in Chemical Biology*. 16(3–4):307-317.

Lin, Y-C., Phua, SC., **Lin, B.**, Inoue, T. 2013. Visualizing molecular diffusion through passive permeability barriers in cells: conventional and novel approaches. *Current Opinion in Chemical Biology*. 17(4):663-671.

Conferences and Presentations

Lin, B., Inoue, T.*, Levchenko, A.* Investigation of individual and collective responses during the directed migration of breast cancer cells using microfluidics. Advances in microfluidics and Nanofluidics 2013. (**Oral Presentation**). South Bend, Indiana. (2013).

Lin, B., Inoue, T.*, Levchenko, A.* Elucidating the roles of contact inhibition of locomotion (CIL) and chemotaxis in the dissemination of breast cancer cells. Gordon Research Conference and Seminars (GRC/GRS)- Directed Cell Migration. Galveston, TX. (2013).

Lin, B., Holmes, W. R., Wang, C. J., Ueno, T., Harwell, A., Edelstein-Keshet, L., Inoue, T.*, Levchenko, A.* Using synthetic signaling perturbations to probe directed migration. Institute of NanoBioTechnology (INBT) Symposium. (**Oral Presentation**). Baltimore, MD. (2012).

Lin, B., Holmes, W. R., Wang, C. J., Ueno, T., Harwell, A., Edelstein-Keshet, L., Inoue, T.*, Levchenko, A.* Synthetic Graded Rac activation drives Cell Polarity and Migration. Gordon Research Conference (GRC)-

Gradient Sensing and Directed Cell Migration. Les Diablerets, Switzerland. (2011).

Lin, B., Holmes, W. R., Wang, C. J., Ueno, T., Harwell, A., Edelstein-Keshet, L., Inoue, T.*, Levchenko, A.* Feedback Machinery of Rac and PI3-Kinase in Directed Cell Migration. Frontiers in Cell Migration and Mechanotransduction. Bethesda, MD. (2011).

Holmes, W. R., Edelstein-Keshet, L., **Lin, B.**, Levchenko, A. A Minimal Model for Symmetry Breaking in Eukaryotic Polarization. International Council for Industrial and Applied Mathematics (ICIAM). Vancouver, Canada. (2011).

Holmes, W. R., Edelstein-Keshet, L., **Lin, B.**, Levchenko, A. Symmetry Breaking In Cell Polarization. Biophysical Society Meeting. (2011).

Smith, C., Yuan Q., **Lin, B.**, Gupta, A., Quinones-Hinojosa, A., Levchenko, A. Enhancement of Mesenchymal Stem Cell-based Therapertics for Brain Cancer. Merck Research Laboratories- United Negro College Fund- Merck Fellow Presentation. Boston, MA. (2011).

Smith, C., Yuan Q., **Lin, B.**, Gupta, A., Quinones-Hinojosa, A., Levchenko, A. In Vitro Models of Enhanced Mesenchymal Stem Cell Homing to Brain Tumors. MSC 2011: Innovations in Cell-Based Regenerative Therapies. Cleveland, OH. (2011).